Infrared Laser Driven Quantum Dynamics

of Double Proton Transfer Reactions
and Collective Carbonyl Vibrations

Universität Rostock

Traditio et Innovatio

vorgelegt von

MAHMOUD K. ABDEL-LATIF

aus Beni-Suef, Ägypten
geb. am 15th November 1975 in Beni-Suef

11-10-2011

Dekan :   . . . .

1. Gutachter :   Prof. Dr. Oliver Kühn,

Rostock University, Institute of Physics

. . . .

2. Gutachter :   Prof. Dr. Ralf Ludwig,

Rostock University, Institute of Chemistry

. . . .

3. Gutachter :   PD. Dr. Volkhard May,

Humboldt University of Berlin, Institute of Physics

. . . .

Tag der Promotion : 11th October 2011

Tag der Submission : 26th July 2011

Author email: `mahmoud.abdel-latif@uni-rostock.de`

I would like to dedicate this thesis to my loving parents,

MOM and DAD

CONTENTS

Glossary

Asym   Asymmetric

Asyn   Asynchronous

Ax   Axial CO

B3LYP   Becke 3-Parameter (Exchange), Lee, Yang and Parr

BS   Bulirsch-Stoer

CCAP   Coherently Controlled Adiabatic Passage

C$_{tot}$ Total Concerted Contribution

CMF   Constant Mean Field

CPL   Circularly Polarized Laser

CRS   Cartesian Reaction Surface

DFT   Density Functional Theory

DOF   Degree Of Freedom

DPT   Double Proton Transfer

DVR   Discrete Variable Representation

Down   Lower Cis

EOM   Equation Of Motion

Eq   Equatorial CO

fb   Free Base Porphyrin

GTO   Gaussian Type Orbital

HF   Hartree Fock

HOMO   Highest Occupied Molecular Orbital

IRC   Intrinsic Reaction Coordinate

IR   Infra-Red

LUMO   Lowest Unoccupied Molecular Orbital

LYP   Lee-Yang-Parr

MCTDH   Multi Configuration Time Dependent Hartree

MO   Molecular Orbital

nD   n-Dimenstional

NOP   Natural Orbital Population

OCT   Optimal Control Theory

PES   Potential Energy Surface

$\mathbf{S}_{tot}$ Total Stepwise Contribution

SIL   Short Iterative Lanczos

SP1   First Order Saddle Point

SP2   Second Order Saddle Point

SPF   Single Particle Function

STO   Slater Type Orbital

STIRAP Stimulated Raman Adiabatic Passage

SV   Split-Valence

Sym   Symmetric

Syn   Synchronous

TDDFT   Time Dependent Density Functional Theory

TDH   Time Dependent Hartree

TDSE   Time Dependent Schrödinger Equation

TISE   Time Independent Schrödinger Equation

TZVP   Triple Zeta Valence Polarization

Up   Upper Cis

UV   Ultra-Violet

VMF   Variable Mean Field

Abstract

This work focuses on the infrared laser driven quantum dynamics of Double Proton Transfer (DPT) reactions in porphycenes and collective carbonyl vibrations in Dimanganese decacarbonyl ($Mn_2(CO)_{10}$).

Laser control of ultrafast double proton transfer is investigated for a two-dimensional model system describing stepwise and concerted transfer pathways. The pulse design has been done by employing optimal control theory in combination with the multiconfiguration time-dependent Hartree wave packet propagation. The obtained laser fields correspond to multiple pump-dump pulse sequences. Special emphasis is paid to the relative importance of stepwise and concerted transfer pathways for the driven wave packet and its dependence on the parameters of the model Hamiltonian as well as on the propagation time. While stepwise transfer is dominating in all cases considered, for high barrier systems concerted transfer proceeding via tunneling can make a contribution.

An asymmetrically substituted porphycene has been chosen as an example for a DPT system since its asymmetry tunes between trans and cis conformers. A quantum chemical characterization of this asymmetrically substituted porphycene is performed using density functional theory. Ground state geometries, the topology of the potential energy surface for double proton transfer, and $S_0 \rightarrow S_1$ transition energies are compared with porphycene and a symmetric derivative. Employing a simple two-dimensional model for the double proton transfer, which incorporates sequential and concerted motions, quantum dynamics simulations of the laser driven dynamics are performed which demonstrate tautomerization control. The possibility to trigger such a double proton transfer reaction by means of an infrared pump-dump laser control scheme has been explored. Transition dipole moments have been calculated for $S_0 \rightarrow S_1$ transitions for the trans conformers and it has been shown that these transition dipole moments dramatically depend on the position of hydrogen atoms in the internal cavity of porphycenes. It is known that, the excitation energy transfer along a molecular wire depends on the orientation of the transition dipole moments of neighboring chromophores. Based on the orientation of the transition dipole moments the tautomerization control may lead to an estimated change in the Förster transfer coupling of about 60%.

The excitation of the degenerate E_1 carbonyl stretching vibrations in dimanganese decacarbonyl using circularly polarized laser is shown to trigger wave packet circulation in the subspace of these two modes. On the time scale of about 5 picoseconds intramolecular anharmonic couplings do not cause appreciable disturbance, even under conditions where the two E_1 modes are excited by up to about two vibrational quanta each. The compactness of the circulating wave packet is shown to depend strongly on the excitation conditions such as pulse duration and field strength. Numerical results for the solution of the seven-dimensional vibrational Schrödinger equation are obtained for a density functional theory based potential energy surface and using the multi-configuration time-dependent Hartree method. Further, a two-dissociative PES suitable for equatorial and axial CO group is discussed. On the basis of these PES it has been shown that laser-induced, non-statistical bond-breaking by means of excitation of the carbonyl stretching vibrations of this molecule is not realistic.

Zusammenfassung

Diese Arbeit richtet ihren Schwerpunkt auf die von Infrarotlasern gesteuerte Quantendynamik von doppelten Protonentransferreaktionen (DPT) in Porphycenen und kollektiven Carbonylschwingungen in Dimangandecacarbonyl, $Mn_2(CO)_{10}$.

Die Laserkontrolle von ultraschnellem DPT wird für ein zweidimensionales Modellsystem untersucht, welches sowohl den schrittweisen als auch den konzertierten Transferpfad beschreibt. Das Pulsdesign wurde unter Verwendung der Theorie der optimalen Kontrolle in Kombination mit der multikonfiguration, zeitabhängigen Hartree (MCTDH) Wellenpaket Propagation durchgeführt. Die erhaltenen Laserfelder entsprechen multiplen Anregungs Abregungs Pulssequenzen. Besondere Beachtung gilt dem relativen Anteil des schrittweisen und konzertierten Transferpfades für das gesteuerte Wellenpaket, sowie dessen Abhängigkeit von den Parametern des Modellhamiltonoperators und der Propagationszeit. Während der schrittweise Transferpfad für alle behandelten Systeme dominiert, kann in Systemen mit hoher Barriere der konzertierte Transferpfad über Tunnelprozessen beitragen.

Ein asymmetrisch substituiertes Porphycen wurde als Beispiel für ein DPT System ausgewählt, wobei die Asymmetrie die Energien von trans und cis Konformeren bestimmen. Die quantenchemische Charakterisierung dieses asymmetrischen Porhycens wurde unter Benutzung der Dichtefunktionaltheorie durchgeführt. Grundzustandsgeometrien, die Topologie der Potentialhyperfläche für den DPT und die $S_0 \rightarrow S_1$ Übergangsenergien wurden verglichen mit Porphycen und einem symmetrischen Derivat. Unter Verwendung eines einfachen zweidimensionalen Modells für den DPT, welches sequentielle und konzertierte Bewegungen beinhaltet, wurden quantendynamische Simulationen der lasergesteuerten Dynamik durchgeführt, welche die Kontrolle der Tautomerisierung zeigen. Die Möglichkeit, solch eine DPT Reaktion mittels einer Anregungs Abregungs Lasersequenz auszulösen, wurde untersucht. Übergangsdipolmomente wurden für die $S_0 \rightarrow S_1$ Anregung der Transkonformere berechnet und es wurde gezeigt, dass diese Übergangsdipolmomente sehr stark von der Position der Wasserstoffatome im zentralen Ring der Porphycene abhängen. Es ist bekannt, dass der Anregungsenergietransfer entlang eines molekularen Drahtes von der Orientierung der Übergangsdipolmomente der benachbarten Chromophore abhängt. Auf der Grundlage der Orientierung der Übergangsdipolmomente kann die Kontrolle der Tautomerisierung zu einer abgeschätzten Änderung in der Förstertransferkopplung von etwa 60 % führen.

Für die Anregung der entarteten E_1 Carbonylstreckschwingungen in Dimangandecacarbonyl unter Zuhilfenahme eines zirkularpolarisierten Lasers konnte gezeigt werden, dass eine Zirkulation des Wellenpakets im Unterraum dieser zwei Moden ausgelöst wird. Auf der Zeitskala von etwa 5 Picosekunden werden keine nennenswerten Störungen durch intramolekulare unharmonische Kopplungen verursacht, selbst unter Bedingungen, bei denen die beiden E_1 Moden mit jeweils bis zu zwei Schwingungsquanten angeregt sind. Es konnte gezeigt werden, dass die Kompaktheit des zirkulierenden Wellenpaketes stark von den Anregungsbedingungen, wie Pulsdauer und Feldstärke, abhängt. Numerische Ergebnisse der Lösung der siebendimensionalen Schwingungs-Schrödingergleichung wurden für eine auf Dichtefunktionaltheorie basierte Potentialhyperfläche unter Benutzung der MCTDH Methode erzeugt. Desweiteren wurde eine dissoziative Potentialhyperfläche, sowohl für äquatoriale als auch für axiale Carbonylgruppen bestimmt. Auf der Grundlage dieser Potentialfläche konnte gezeigt werden, dass ein laserinduzierter, nicht statistischer Bindungsbruch durch Anregung der Carbonylstreckschwingung in diesem Molekül nicht realistisch ist.

CHAPTER 1

Introduction

Chemistry is life! Chemical reactions are of great interest in all aspects. In these chemical reactions bonds are broken and are formed. This bond formation and bond breaking can occur in ground or excited states of the molecule under investigation. Driving the reactions in the ground state is of great importance for the initiation of certain chemical reactions and for increasing reaction efficiency. In this thesis, Double Proton Transfer (DPT) reactions in porphyrin-like structures and collective carbonyl vibrations in dimanganese decacarbonyl $Mn_2(CO)_{10}$ complex triggered by ultrfast laser pulses in IR regime will be discussed. In a very broad view, in this thesis a model for DPT has been used to mimic an organic substrate like porphyrins. Porphyrins are interesting for theoretical and experimental scientists. These porphyrins have two hydrogen bonds. In other words they allow for DPT reactions. This does not mean that every system with two hydrogen bonds has DPT, but it depends on the strength of the hydrogen bond. In our porphyrin system like structures DPT indeed can be observed. In this reaction two bonds are broken and two are formed. The interesting question that comes into mind at this point is that, "is this bond breaking or formation occurring synchronously or asynchronously?" One aim of this thesis is to drive these chemical reactions using designed ultrafast laser pulse in the infrared (IR) regime and to answer this question. Also applications of this kind of driven DPT as a way to control the energy transfer through photonic molecular wire containing DPT system are discussed. In the second part concerning Dimanganese decacarbonyl of this thesis, multi-dimensional potential energy surface (PES) is created and the anharmonic IR spectrum is calculated. Furthermore, it will be shown that concerted CO bond vibration can be triggered using circularly polarized laser (CPL) such that the excitation circulates around the symmetry axis. At the end, as far this manganese complex (Mn_2CO_{10}) is used as a source of CO, two-dimensional dissociative PES for both axial and equatorial CO will be obtained and the possibility for Mn-CO dissociation will be discussed. But, without any explicit laser excitation and using dragged ground state wavepacket instead.

This chapter contains a brief introduction to porphycenes Sec. 1.1. Hydrogen bonds and their effects on the potential energy surface (PES) comes in Sec. 1.2 followed by proton transfer reactions and their mechanisms Sec. 1.3. Different ways of controlling chemical reactions using laser control are introduced in Sec. 1.4. A very brief definition for the transition dipole moment comes in Sec. 1.5. In Sec. 1.6 and 1.7 photonic molecular wires realizing electronic excitation energy transfer and ways of switching this

energy transfer are presented. In Sec. 1.8 an introduction into Dimanganese decacarbonyl, Mn_2CO_{10}, complex is given. Vibrational ladder climbing for anharmonic PES is introduced in Sec. 1.9. Finally, the goals and structure of this work will be presented in Sec. 1.10 and 1.11, respectively.
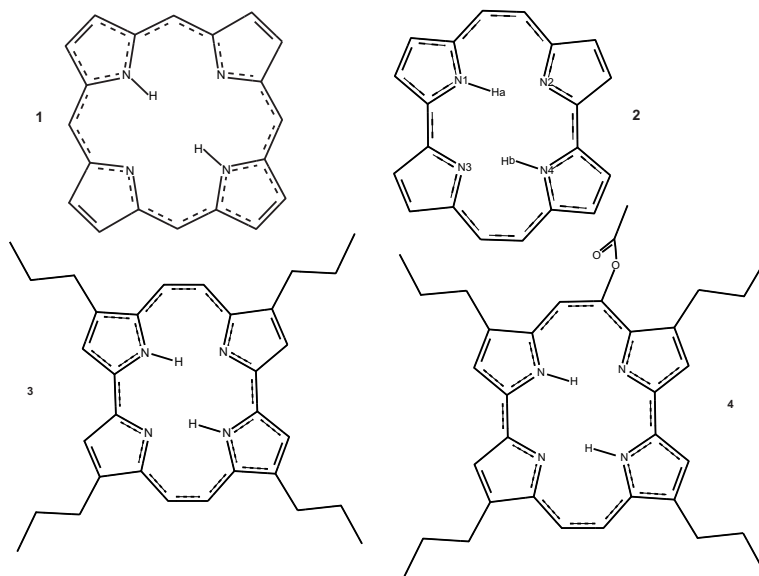
Fig. 1.1 *Reference structures of Porphyrin (parent molecule) and considered porphycenes: 1 free base porphyrin, 2 free base porphycene, 3 tetra-n-propyleporphycene and 4 tetra-n-propyleacetoxyporphycene.*

1.1   Porphycenes

Porphyrins and metalloporphyrins are molecules that have been intensively studied both in basic and in applied science for many years. They play a crucial role in biological processes, such as photosynthesis, biological redox reactions oxygen, transport and activation, so that porphyrins are described as pigments of life [1, 2, 3]. Furthermore, they are found in a wide variety of applications that exploit their photophysical properties. Recently, a lot of work has been focused on the development of metalloporphyrin assemblies and porphyrin containing mimics of photosynthetic reaction centers for light-harvesting purposes, as well as on the creation of molecular alternatives for duplicating the photoinduced processes involved in solar energy conversion [4, 5, 6], molecular memories [7, 8], photovoltaic devices [9], in medicine as phototherapeutic agents [10, 11] and of further advanced applications [12, 13]. The development in synthetic procedures lead to the creation of a new class of compounds, for instance, expanded, contracted or inverted porphyrins [14, 15].

Among these compounds, there are some constitutional isomers of porphyrin which are of particular interest here [15], namely tetrapyrrole macrocycles which differ from the parent porphyrin in the way of linking the pyrrole rings with each other through methine groups. As an example, the methine group in case of the parent molecule and the ethyne group in case of porphycenes are presented in Fig. 1. The research in this area has been stimulated since the synthesis of porphycene **2** by Vogel and co-worker [16] in 1986. Porphycene as a free base is the most stable isomer of all porphyrin isomers.

The aim of choosing molecules **3** and **4** is to shed some light on the effect of symmetric **2** and asymmetric **3** substitutions of porphycene for the ground state properties and for the $S_0 \rightarrow S_1$ excitation spectrum. For the laser-driven DPT, the potential energy surface shape is really important. For instance, the barrier height should be overcome by excitation with a few IR photons and the energy difference between the reactants and products should be found otherwise the feed back reaction via tunneling can not be prevented. Asymmetrically substituted porphycene **4** seems to meet these requirements. The stability of free base porphycene is attributed to the very strong intramolecular double NH···H hydrogen bond. The strength of these hydrogen bonds is due the shorter N–N distance which is 2.63 Å [16] as compared to 2.90 Å [17] for porphyrin. For metal complexes, the relative stabilities of porphycene and porphyrin are reversed, since the internal cavity in porphyrin is larger than in porphycene which fits the accommodation of metals. Compounds **1-3** have been shown to be planar aromatic compounds but compound **4** has been confirmed to be non-planar due to the substitution of the acetoxy group in the 9-position which prefers to be out of plane from the energetically point of view as will be shown in the results chapter 3, Sec. 3.6. All the considered molecules have different tautomeric structures. Each has four internal nitrogen atoms which are arranged as a square in case of porphyrin and a rectangle in case of porphycenes. There are two protons which can migrate from one nitrogen to another giving trans and cis isomers. In the trans structure the two hydrogen atoms are located on the opposite nitrogen atoms as shown in Fig. 1. whereas in the cis structure they are located on the adjacent nitrogen atoms which is shown later. There are two ways for migration of these two protons; synchronous (concerted) where the two protons move simultaneously through a second order transition state or asynchronous (step wise) where the two protons move one after the other through a first order transition states giving the cis isomers as intermediates (local minima).

The X-ray structure of porphycene **2** shows equal delocalization of the two protons over all four nitrogen atoms and the distance between hydrogen bonded atoms is 2.63 Å [16]. Actually this value lies between the calculated values for the trans and cis isomers of porphycene **2** suggesting the, presence of both trans and cis in the crystal. In porphycene, the two intramolecular hydrogen bonds are stronger than in porphyrin because of the shorter N–N distance and the nearly linear arrangement of N–H···H, giving an angle of $152°$ [18]. The IR active NH stretching frequency for porphyrin **1** is observed in rare gas matrices at around 3320 cm^{-1} [19]. But, in case of porphycene **2** the strong hydrogen bonds should result in the NH vibrational frequencies to be red shifted. The electronic absorption spectra of the constitutional isomers of porphyrin exhibit the characteristic spectra of the parent porphyrin compound. These spectra are characterized with a lower intensity Q transitions in the red part of the visible region followed by stronger Soret bands in the near UV [20]. For porphycene **2**, the two trans are the same (degenerate) as are the two cis. So, it is difficult to see the Q peak for each trans. In case of asymmetric porphycene **4**, the situation is different where the two trans or two cis tautomers should no longer be degenerate which has been confirmed by Waluk. Ground state calculation using density functional theory (DFT) to see the effect of symmetric and asymmetric substitution on the hydrogen bond parameters as well as the rectangle lengths for the four nitrogen cavity as well as time-dependent DFT (TDDFT) to get the electronic absorption spectra for the considered molecules have been studied in this work and the results will be shown in chapter 3, Sec. 3.8.
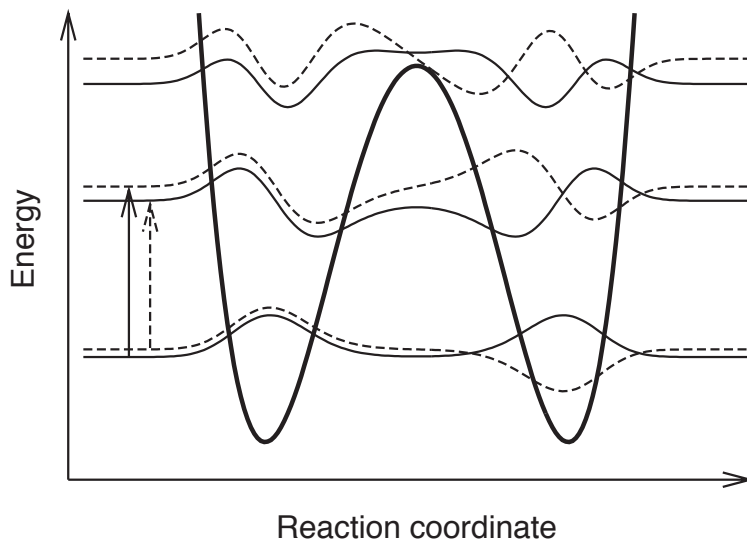
Fig. 1.2 *Schematic plot of the potential energy curve and the some vibrational wave functions of a proton transfer in a weakly hydrogen bonded system. The solid (dashed) curves are wave functions of even (odd) parity. The solid (dashed) arrow characterizes transition from even (odd) parity to odd (even) parity.*

1.2   Hydrogen Bonds and Their Effect on the PES

In 1920 there was the first publication of the hydrogen bond as a new type of weak bond [21, 22]. The name of hydrogen bonds has introduced by Pauling [23, 24] ten years later. One of the most important chemical reaction is the hydrogen atom or hydrogen ion (proton) transfer reaction. Therefore in the following, we will give a description of hydrogen bonds, their types and effects on the potential energy surface (PES) and their relevance in physics, chemistry and biology. The traditional hydrogen bond, A–H$\cdots$B, is an electrostatic attraction between a positively charged or partially charged proton attached to a donor atom A and a negatively charged or partially charged proton acceptor B, where A and B can be the same or different atoms. Further one may distinguish between intramolecular hydrogen bonds and intermolecular hydrogen bonds. But, the non-traditional hydrogen bonding is that formed between two hydrogens in a system like, A–H$\cdots$H–M, where A is more electronegative atom than hydrogen which (is partially positive) and M is less electronegative atom than hydrogen which (is partially negative). So the electrostatic attractions between these two partially charged hydrogens gives this kind of hydrogen bonding. Typically non-traditional hydrogen bonding is characterized by H—H distances of 1.7–2.2 Å and A–H$\cdots$HM bond angles between 95° and 120° [25].

As a result of the traditional hydrogen bonding interaction, the potential energy surface becomes more softer and leads to a red shift of the frequency of the A–H bond stretching vibration. The dynamics of the central proton becomes much more complicated than that of a free covalently bounded hydrogen, but H coordinate can be described by a simple potential well including the increase of the hydrogen bonding strength. There is an evidence that the shape of the potential energy surface along the proton transfer reaction depends qualitatively on the bond strength. Huggins [26] has introduced the potential energy curve of the proton transfer between two oxygen atoms and he has pointed out that, the potential energy curve changes from double minimum to a single minimum

upon decreasing the distance of the heavy atoms $O \cdots O$.

Hydrogen bonding and transfer plays a fundamental role in many fields, determining the physical, chemical and biological properties of molecules and solids [27, 28, 29, 30]. Double hydrogen bonded systems play a crucial role as a model for the understanding of the DNA base pairs. Proton transfer is of great interest for biology as well as being a fundamental reaction in chemistry [31, 28]. Moreover, multiple proton transfer in hydrogen bonded system is one of the most fundamental reactions in chemistry and biology. It repairs the DNA base pair mutations [32] and it governs the oxidation reduction reactions in many chemical and biological reactions [33].

The strength of hydrogen bond is responsible for the properties of the molecular system under consideration. Consequently, hydrogen bonds are classified according to their strength into three types, weak, medium, and strong hydrogen bonds. The weak hydrogen bond is characterized by bond energies less than 4 kcal/mol [34]. In this case the potential energy surface is of double well potential shape with two minima along the hydrogen transfer reaction coordinate with high potential energy barrier but significantly lower than the free A–H covalent bond dissociation energy. The heavy atom distance $A \cdots B$ may vary from 3.1 Å to 4.3 Å. A potential energy curve of proton transfer of this weak hydrogen bonding case and some eigenstates of this potential are shown in Fig. 1.2. The parent porphyrin molecule **1** fits this kind of hydrogen bond which is characterized by presence of two weak hydrogen bonds and high energy barrier.

In medium strong hydrogen bonds, the bond energy is varying from 4 to 14 kcal/mol and the heavy atom distance $A \cdots B$ is shortened and is varying from 2.4 Å to 3.3 Å . Such increase of the bond strength decreases the potential barrier height and as a result the anharmonicity of the potential energy curve along the hydrogen transfer reaction coordinate is increased. The description of this reaction coordinate will be discussed later in the theoretical part.

While a strong hydrogen bond is characterized by a large bond energy which might exceed 14 kcal/mol. Also the heavy atom distance is decreased to be less than 2.7 Å . The increase of the strength of the hydrogen bond in this case decreases or even removes the potential energy barrier leading to a quite flat potential energy surface with very high mobility of the bridging proton as shown in Fig. 1.3. This kind of hydrogen bonds are well known in biochemical reactions [35].

For the studied molecules, porphyrin has a weak hydrogen bonds so its PES looks like Fig. 1.2. For the most stable constitutional isomer of porphyrin, porphycenes, they have strong hydrogen bonds comparing to the parent compound. So one could say that, although all considered porphycenes have a strong hydrogen bonds they have not a flat PES like Fig. 1.3 but they have a PES looks like Fig. 1.2 but with lower barrier height comparing to porphyrin.

1.3 Double Proton Transfer and its Mechanisms

The mechanism of the tautomerization of hydrogen bonded systems, induced by a double proton transfer from one stable tautomer to another more stable one in a synchronous or sequential fashion, has been extensively discussed in literature [36, 37, 38, 39, 40] and in particular for hydrogen bonded base pairs (see Refs. [41, 42]). Moreover, there is a number of theoretical and experimental investigations that have been done to clarify the mechanism and dynamics of intramolecular double transfer responsible for the tautomerization in porphyrins [43, 44] and porphycene [37, 45].

In this work we are going to present quantum dynamics simulations for the double proton transfer reaction of the constitutional isomers of porphyrin. This DPT transfer
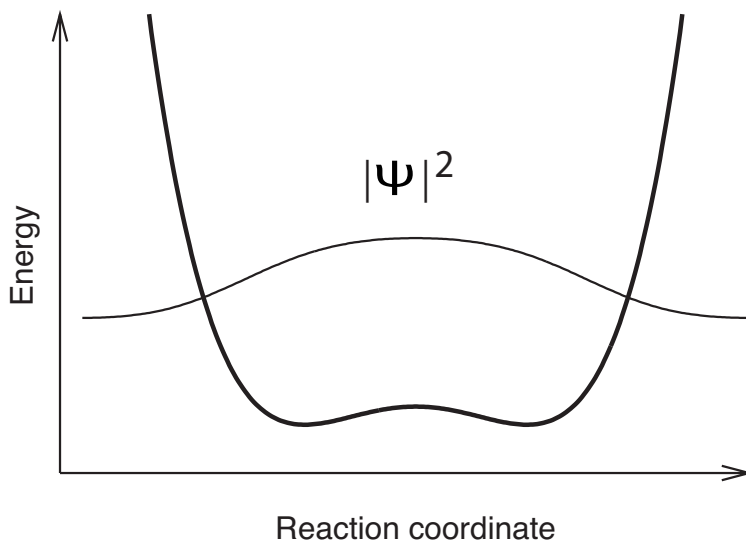
Fig. 1.3 *Schematic plot of potential energy curve and vibrational ground state wave function of a strong hydrogen bonded system.*

reaction involves the breaking of the two NH bonds and the formation of the two alternative NH bonds. Our quantum dynamics simulation of these DPT involves the electronic ground state.

Actually there are two different ways of these DPT; synchronous (concerted) mechanism where the two hydrogen atoms move simultaneously, in other words the two NH bonds break in the same time, or asynchronous (stepwise) mechanism in which one NH bond breaks first and the new NH bond forms afterwards, the other NH bond breaks and the new NH bond forms. Different scenarios of DPT are presented in Fig. 1.4. In general, the classification of the reaction mechanism as synchronous or asynchronous may depend on method used. For example, depending on the bases of the quantum chemistry calculations, the type mechanism has often been attributed to the investigation of PES i.e. all minima and all maxima of the system under consideration. Specifically, the investigation of the obtained saddle points [46, 47]. If the barrier height for the synchronous mechanism is lower than the barrier height for the sequential mechanism, then it was concluded that the concerted mechanism is more dominant than the asynchronous mechanism. Further, in other cases the determination of the mechanism has been based on the consideration of the reaction path: if it goes from the initial geometry (reactant) to the final geometry (product) through a reaction intermediate, which is characterized by a local minimum, then the reaction mechanism is called sequential, while if the reaction leads from the reactant to the product via only a global maximum or might be through tunneling in which the protons penetrate the barrier through forbidden region, then, the reaction is concerted, for more details see for instance, Refs. [48, 49] In this thesis, we are interested to investigate the mechanism of DPT and its dynamics using quantum dynamics simulations in the presence of a driving IR laser.
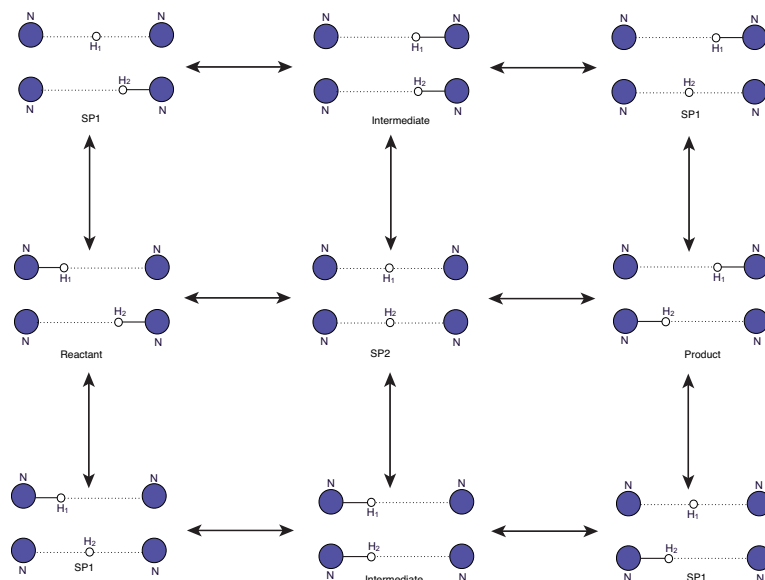
Fig. 1.4 *Mechanisms of DPT: Concerted versus step-wise mechanism in porphyrins. In the concerted one the reaction goes through the SP2 maximum while in step-wise one the reaction goes through the SP1 maxima to the intermediates and then to the product.*
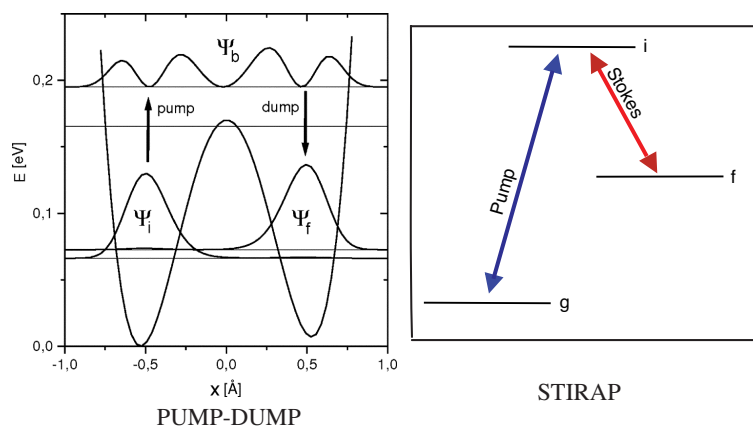
Fig. 1.5 *Left: Illustration of the pump-dump scheme for a slightly asymmetric one-dimensional double well potential. The first laser pumps the ground state wave packet from the localized state ψ_i to an above the barrier delocalized state ψ_b. From there the second pulse dumps the population into the target state ψ_f which is in the other well of the PES. Right: The STIRAP method for control.*

1.4 Laser Control

Control why, how and what comes after! In a very broad description for the why, to get a deeper understanding of system, investigate its properties like, structure, spectroscopy and to find possible reaction pathways. For the how, using modern techniques of laser shaping. Laser control of nuclear and electron dynamics has become an active field of research during the last decade in physics and chemistry [50, 51]. Guide lines can be

seen in femtochemistry experimental reviews on coherent control (see Refs. [52, 53]), and in femtosecond time-resolved photon electron spectroscopy (see Ref. [54]). Recently, laser pulse design became a powerful tool to control molecular dynamics. For example, selective population transfer to a specified quantum state of molecules could be achieved. [50, 55]. There are many laser methods which can be used to control the dynamics of a system. A straightforward and well known method for laser driven dynamics is the so-called pump-dump approach.

The pump-dump approach has been introduced by Tannor et. al. [56]. As inferred by its name, there are two pulses, pump pulse and dump pulse. The first pump-pulse excites the ground state wavepacket, which is localized in the reactant well of the potential energy surface, into a delocalized excited state above the reaction barrier. Then, comes the second dump-pulse after a certain delay time to drive the excited state wave-packet from the delocalized excited state to the localized product well in the PES. An illustration of the pump-dump scheme is shown in Fig. 1.5. Actually, the optimization of the field parameters can be done by hand, or the complete pulse can be obtained automatically by so-called optimal control theory (OCT).

This optimal control theory has been introduced by the Rabitz's group [57, 58]. The optimal control theory has the ability to design a sequence of laser pulses that drives the initial state to a desired final state. For pioneering work in optimal control theory OCT (see Ref. [59]), for more details see the review on OCT [60]. The OCT has been applied for controlling the hydrogen transfer in Refs. [61, 62]. In the OCT the pulse intensity is constrained via what so-called penalty factor. The mechanism of the proton transfer is switched from above the barrier into tunneling one upon increasing the penalty factor for strong laser pulses [61, 62]. In this case the laser field looks like a few cycles and the associated dynamics in isolated and dissipative systems were investigated in more details in Refs. [63, 64]. In this work OCT has been used to control the DPT reaction. More explicitly, a comparison between pump-dump and OCT has been given. Applying some restrictions on the OCT process may lead to various desirable properties of the process, for instance, robustness [65, 66] and π-pulse like structure.

A generalized π-pulse approach has been introduced by the Manz group [67, 68]. In this approach, a pulse sequence is made appropriately by optimizing some laser parameters in an analytical function characterizing the laser pulse structure. This approach is characterized by achieving fast population transfer to a certain state but, with low product yield. In order to overcome the product yield problem, strict conditions should be applied for the laser parameters such as pulse width and pulse intensity to achieve high product yield.

In contrast to the π-pulse approach, is the stimulated Raman adiabatic passage (STIRAP) which was presented by Bergmann et al. [69]. It is a control scheme that is designed to achieve a complete transfer population between specified quantum states, and it is more robust than its π-pulse counterpart, which is also used to invert populations [70, 71]. STIRAP approach is also well-known as an effective technique for population transfer in three level systems [72]. This laser controlling approach has been experimentally verified for atoms and small molecules [69]. The STIRAP steps approach of laser control is presented in Fig. 1.5.

For the what comes after? Intuitively comes the applications of laser control. There are many applications for the laser control, for instance, its application to trigger proton transfer as mentioned above. Pump-dump scheme has been applied for driving the proton to transfer from one minimum to another on the potential energy surface (PES) [73, 74]. Also it has been used for two a dimensional (2D) model which mimics the situation of proton transfer in malonaldehyde derivatives see Ref. [61].

Actually, laser control of DPT reactions has not attracted much attention. Nishikawa

et al. [75] considered control of stepwise DPT in an asymmetrically substituted tetraflouro-prophyrine model using STIRAP method. In this simulation, they adopted a two-step sequential model of the DPT, where one proton migrates from the most stable global minimum (one trans form) to the intermediate (one cis form), and then the other proton transfers from this cis form to the other global minimum (the second trans form) as shown in Fig. 1.4. In this two independent one-dimensional potential, they applied for density functional theory (DFT) method, intrinsic reaction coordinate (IRC) calculations. It was shown that the STIRAP pulse sequence induced the transition from the most stable trans form to the other trans form via the cis intermediate state on a time scale of some tens of picoseconds. Shapiro and coworker have considered triggering DPT in the context of DNA nucleotide base-pairs by coherent light [76]. They developed a two-dimensional PES for DPT in dinucleotide pair model system. They have applied the so-called coherently controlled adiabatic passage (CCAP) for this control and as result, direct identification and automatic repair of mutations arising from the misplacement of the two protons involved in the hydrogen bonding system of the dinucleotide has been demonstrated. Finally, Thanopulos et al. [77] have shown the implications of DPT control for single molecule charge transfer. Considering a thio-functionalized porphyrin derivative attached to four gold electrodes it was found from molecular orbital analysis that the different trans forms essentially provide orthogonal pathways for electron transfer. Laser controlled switching was discussed in a stepwise model comprising two bond coordinates for the first step and a single linear reaction coordinate for the second one. In the present work, we simulated laser-induced intramolecular DPT to control the motion of protons in a hydrogen bonded system, see Ref. [37, 78]. We used asymmetrically substituted porphycene as the DPT system. The motion of the protons in such a system are described by a simple two dimensional model which was introduced by Smedarchina and co-workers [36].

1.5 Transition Dipole Moment

Another application for the laser control is controlling the transition dipole moment orientation. In brief, transition dipole moment usually denoted $\boldsymbol{\mu}_{if}$, is the electric dipole moment associated with the transition between the two states, an initial state i and a final state f. In general the transition dipole moment is a complex quantity that includes the phase factors associated with the two states. Its direction gives the polarization of the transition, which is very important and of great interest because it determines how the system under investigation will interact with an electromagnetic wave of a certain polarization, while the square of the magnitude gives the strength of the interaction due to the distribution of charge within the system. The comparison to the classical dipole moment can be very useful, care must be taken to ensure that one does not fall into the trap of assuming they are the same. The classical dipole moment is the multiplication of the charge of two separated classical charges $+q$ and $-q$ with the displacement vector $\mathbf{r}$ pointing from the negative charge to the positive charge. While the transition dipole moment for the transition $\boldsymbol{\mu}_{if} =< f|\mathbf{E}|i >$ is given by the relevant off-diagonal element of the dipole matrix, which can be calculated from an integral taken over the product of the wavefunctions of the initial and final states of the transition, and the electric dipole moment operator $\mathbf{E}$ which is a vector operator that is the sum of the position vectors of all charged particles weighted with their charge while the transition moment $\boldsymbol{\mu}_{if}$ is a vector in the molecular framework, characterized both by its direction and its amplitude. The transition dipole moment is very important quantity where it controls how much of the transition between two states can be achieved. As has been discussed in the previous section (Sec. 1.4), laser control will be used to trigger DPT in porphycenes. It has been

found that, the transition dipole moment depends strongly on the internal Hydrogen atoms positions of porphycenes, for more details (see Ref, [79, 78]). Once the DPT has occurred, the positions of hydrogen atoms are changed and as a result, the transition dipole moment orientation should be changed and as a result the Förster energy transfer efficiency between the chromophores in a molecular frame should be affected since the coupling between neighboring chromophores depends on the orientation of the transition dipole moment as it will be introduced in Chapter 3, Sec. 3.7.4
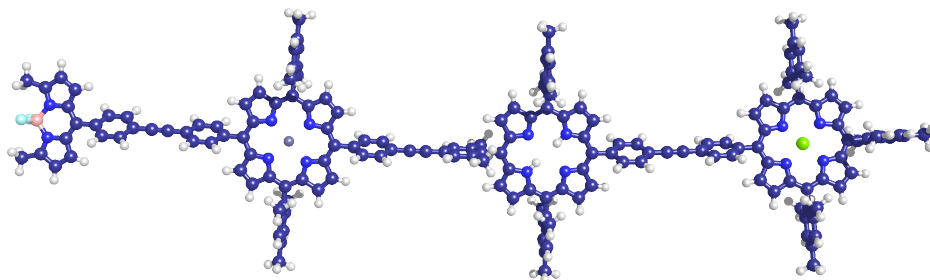
Fig. 1.6 *An example of a molecular photonic wire which consists of a boron-dipyrrin (BDPY) dye as an input unit, Zn-porphyrine as a transmission unit, a free base porphyrine (fb) as an output unit, and Mg-porphyrin. This wire has been optimized using the DFT, B3LYP/LanL2DZ method.*

1.6 Molecular Photonic Wires

A wire is a device which permits the flow of energy or charge through it. In addition to its transmission capabilities, a wire should include provisions to be connected to an input unit at one end and output unit on the other end. Wires are considered as a carriers of electrons or holes. But, a molecular photonic wire is distinguished from a molecular electronic wire by supporting excited-state energy transfer rather than electron or hole transfer. In other words, a photonic wire conducts excited-state energy rather than charge from donor to acceptor. In order to get into the excited-state energy transfer process an external effect, for instance, light should excite the input unit in the wire i.e. photon in (absorption), energy flows through the transmission units and then emission occurs through the output unit (photon out). An example is given in Fig. 1.6

Molecular photonic wires are of great interest as biomimetic models for photosynthetic light harvesting systems and as molecular devices with lots of application in material chemistry [80, 81]. Lindsey et al. as a first step in their research toward realization of molecular devices transporting via electronic excitations developed and described the design and the static spectroscopic properties of a molecular photonic wire [82]. Lindsey and coworkers synthesized and characterized a large number of other weakly coupled multi porphyrins arrays, including optoelectronic gates [83] and a variety of light harvesting architectures [84, 85]. Also they prepared a number of dyads and triads for probing

the nature of electronic communication that underlies efficient excited-state energy transfer and they demonstrated that the excited-state energy transfer in diarylethyne-linked arrays occurs predominantly by through bond processes, with only minor amount of through space contributions [86].

Hiddin and coworkers [87] studied the excited state energy transfer rates in covalently linked multiporphyrin arrays and they provided a detailed picture of the dynamics of the energy flow in multiporphyrin architectures. They found that the energy transfer has two ways. One through adjacent multiporphyrin chromophores which occurs via through bond-type mechanism and the other is through non-adjacent multiporphyrin chromophores via Förster through space mechanism. The rate of energy flow between non-adjacent multipophyrin chromophores is only 5-10-fold slower than for adjacent units. These multiporphyrin chromophores are connected together via a small unit which is called linker. There are different kind of linkers for instance, diphenylene and phenylene linkers. Of course, the rate of energy transfer depends on the linker type. Song et al. [88] studied the excited-sate energy flow in phenylene-linked multiporphyrin arrays and they found the rate constant for energy transfer from a photo excited zinc porphyrin to a free base porphyrin is approximately 10-fold faster for dyads that utilize a phenylene linker than for those that used a diphenylene linker.

Porphyrins and metalloporphyrins are a key part of molecular photonic wires studied so far. An example of a photonic molecular wire is presented in Fig. 1.6 which is composed of a boron-dipyrrin (BDPY) dye as an input unit, Zn-porphyrine as a transmission unit, a free base porphyrine (fb) as an output unit, and Mg-porphyrine. Boron-dipyrrin is an interesting chromophore composed of a dipyrromethane having both of its nitrogens coordinated to a boron atom, which is appended with two fluorines. The ring containing the boron is conjugated and the boron atom has a tetrahedral coordination geometry. These molecules are typically functionalized at positions on the phenyl ring due to the synthetic ease. Due to their intense light absorbance and emission properties they have been widely utilized as energy donors and fluorescent probes in chemo- and biosensors [89]. In this wire boron-dipyrrin is used as an energy donor to zinc porphyrin (transmitters) and then free base porphyrin or magnesium porphyrin. In the present study, the TDDFT excited state calculation has been done for DPT system (porphycenes) which could be used as a component of the molecular photonic wire showed to get an idea about the transition dipole moment orientation due to the tautomerization. Results will be reported in Sec. 3.7.4

A different design strategy has been followed by Sauer and coworkers who have used the backbone of double-stranded DNA as a scaffold for positioning highly fluorescent chromophores [90, 91] (see also Ref. [92]). In this case, Förster type dipole-dipole interaction driven transfer is the responsible mechanism for energy transfer with efficiency almost to 100 % over a range of $\sim$ 14 nm.

1.7 Energy Transfer and Ways of Switching it

An example for supramolecular systems which acts as molecular photonic wires are those composed of different metalloporphyrins. The ability of several metal ions in metallated porphyrins to bind one or two ligands axially has been extensively used to prepare a large collection of self-assembled supramolecular systems with impressive structures (see for instance [93, 94] and references therein). Zn (II) [95, 96] and Co (II) [97] porphyrins have been used for this purpose and in several cases resulted in systems that have served as interesting models for the study of photoinduced processes like energy [98, 99] or electron transfer [100, 101] that mimics the same processes occurring in natural photosynthesis. An electronic excited state is reached when an external laser field excites the electronic
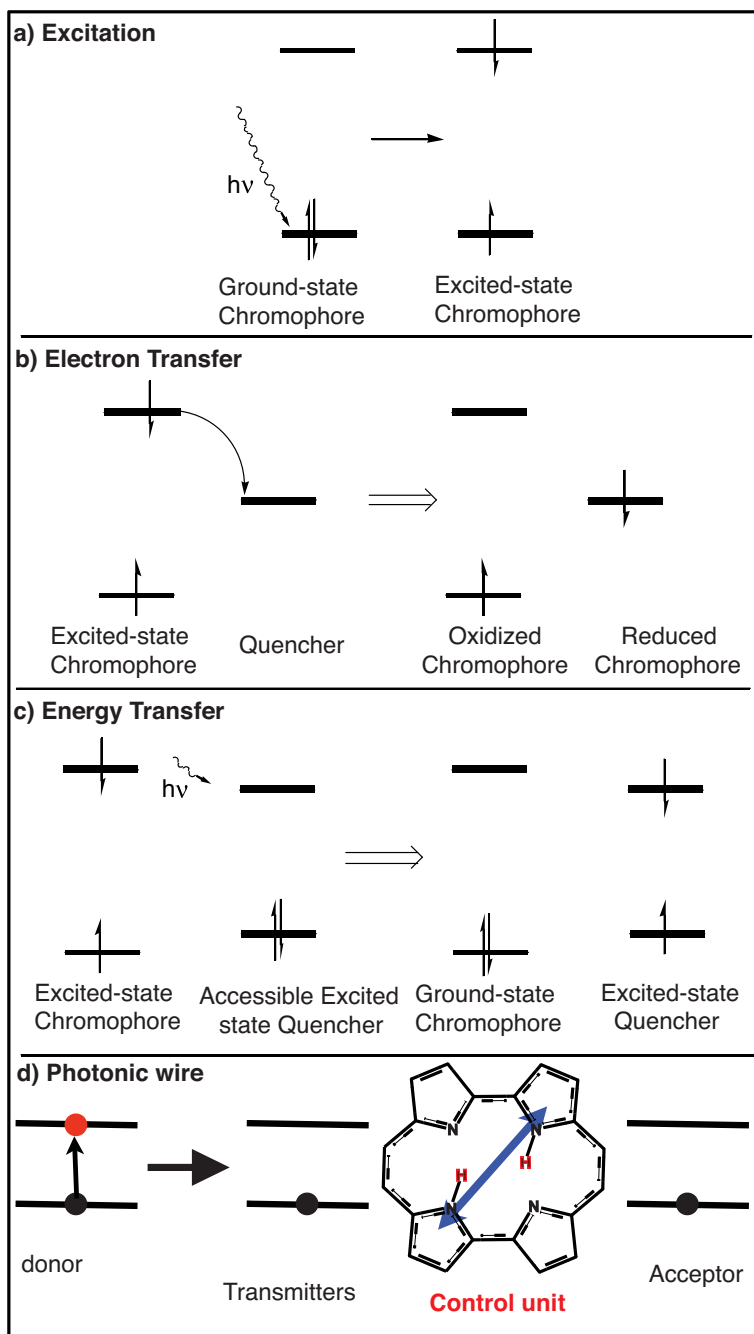
Fig. 1.7 *Schematic representation of (a) excitation process, (b) electron transfer, (c) energy transfer and model of molecular photonic wire (d).*

ground state leading to excitation of one electron to the excited state. In fact this excited electron will not stay for long time in this excited state. So, there are two ways for this excited electron to follow. The first one is the stimulated emission ending up with the ground state again and the energy which is emitted could be used to excite a second
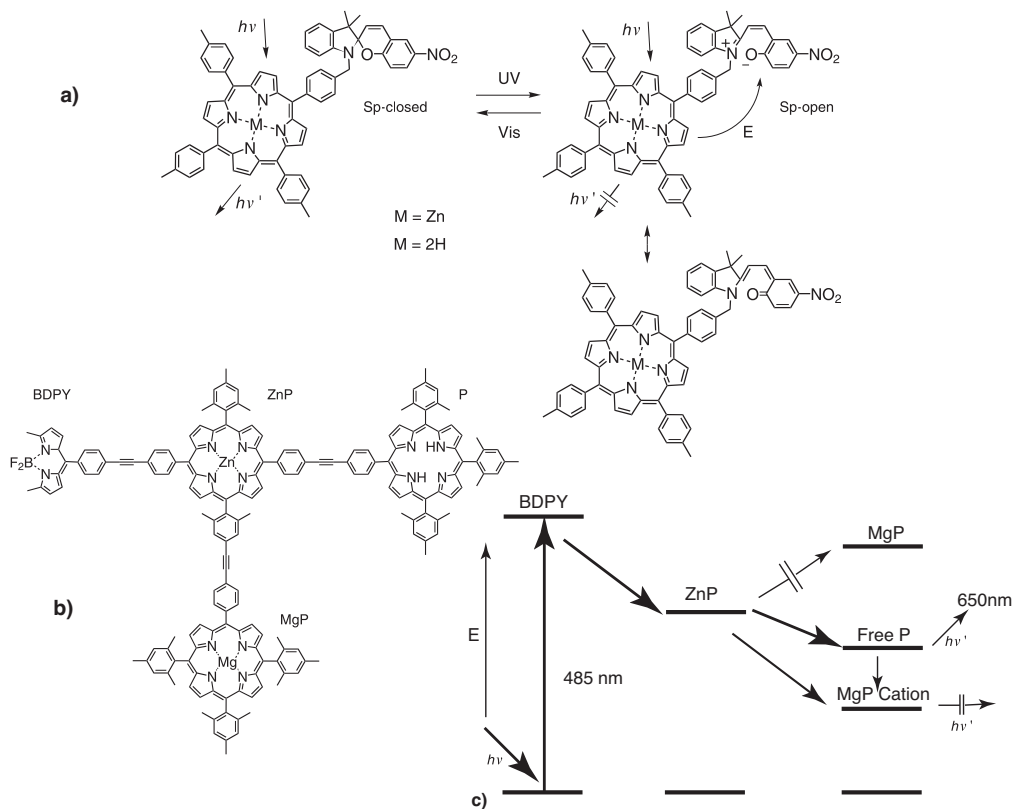
Fig. 1.8   *Schematic representation of (a) optical switching [102], (b) electrochemical oxidation [103, 104] switching processes of energy transfer and (c) energy level diagram for (b) adapted from Ref.[104]*

chromophore. The second way is the charge (electron) transfer from the excited state of this chromophore to an excited state of a neighboring chromophore. A schematic representation of such processes is shown using energy level diagrams is introduced in Fig. 1.7. In panel (a) the excitation process in which the laser excites the electronic ground state and transfers one electron from the HOMO orbital of the input chromophore (energy donor unit) to the LUMO orbital of that molecule. In Panel (b) the electron transfer process is presented where the excited electron of the donor chromophore is transfered to the vacant molecular orbital LUMO of the acceptor chromophore creating a charge separated donor-acceptor pair. Energy transfer occurs when there is some coupling between the electronic excited state of the first molecule and the second molecule. The excitation energy of the electronic excited state is transfered from the donor to the acceptor molecule. At the end the excited state of the second molecule is reached as shown in panel (c). In panel (d), a molecular photonic wire is shown which contains the double proton transfer chromophore which might be a free base porphyrin or free base porphycene.

The utilization of molecular photonic wires in optoelectronic devices requires to have at hand a means for switching the energy transfer process. There are various methods for switching, for instance, optical excitation using UV radiation [102]. The substrate used in this case is shown in Fig. 1.8 a. This compound contains a photochromic nitrospiropyran unit which is covalently linked to a zinc porphyrin or free base porphyrin. The excitation

energy can be transfered to neighboring units and the nitrospiropyran moiety relaxed to its ground state. Optical excitation of the nitrospiropyran moiety in this compound results in a zwitterionic moiety as presented in Fig. 1.8 a. Excitation energy can not be transfered subsequently to neighboring units. Instead, this excitation energy is quenched by converting this zwitterionic to a ring opening structure. Electrochemical oxidation can also be used as tool for switching energy transfer [103, 104] as introduced in Fig. 1.8 b, see also the energy level diagram in Fig. 1.8 c. This wire consists of a boron-dipyrrin (BDPY) input unit, a zinc porphyrin transmission unit, a free base porphyrin output unit and a magnesium porphyrin unit linked to the zinc porphyrin unit and acting as a redox switch key in this array. In the neutral system, photo excitation of the BDPY chromophore results in excited state energy transfer followed by emission from the free base porphyrin output unit, which has the lowest excited state energy, that fluoresces strongly as shown in the energy level diagram in Fig. 1.8 c. Electrochemical oxidation of magnesium porphyrin in this array leads to the formation of a radical cation of the magnesium porphyrin unit, which has low lying non-fluorescent excited states. So, in the oxidized form, the fluorescent excited state is either not populated or quenched. The photo excitation energy may be restored for returning back to the neutral molecule via electrochemical reduction. Another way for switching energy transfer is the acid-base effect i.e. change of the (pH) value [105, 106]. For more details see Ref. [107].

In this thesis we propose another technique for switching excited state energy transfer using an ultrafast laser field in the few picoseconds regime [37]. The idea builds on the observation that the direction of the electronic transition dipole moment, which is responsible for the coupling between the chromophores in the Förster mechanism [108] depends on the position of the two hydrogen atoms in the porphyrin like structure building blocks. Thus isomerization between the ground state tautomers, or in other words, driving double proton transfer (DPT) by means of an appropriate designed laser field in the infrared (IR) domain allows one to control the strength of the Förster transfer coupling. Returning back to panel d in Fig. 1.7, the (switching) unit is the free base porphyrin which facilitates (DPT). Triggering the (DPT) for this unit by an ultrafast IR laser pulse changes the transition dipole moment orientation of the switching unit by some degree and consequently controls the coupling between chromophores that is responsible for energy flow through the photonic molecular wire.

1.8   Dimanganese Decacarbonyl (Mn$_2$(CO)$_{10}$) Complex

Transition metals and their complexes with different ligands are important catalysts for reactions that are used industrially and synthetically [109]. In the last few decades a lot of theoretical studies on this group of molecules have been done to understand the electronic properties of the carbonyl complexes see, for instance, Refs. [110, 111, 112]. Experimental investigations of the dynamics and laser control of carbonyl complexes has also been discussed, see refs [113, 114, 115]. Homoleptic manganese decacarbonyl has been discovered in 1954 i.e. much more recently than most other stable homoleptic metal carbonyls of the first row transition metals because of the difficulty of its synthesis [116]. X-ray diffraction studies of Mn_2CO_{10} have shown a direct manganese-manganese bond without bridging carbonyls between the two metal atoms and D_{4d} point group symmetry of the molecule [117]. Dimanganese decacarbonyl plays an important role as a prototype system for organometallic compounds with metal metal bonds. This molecule, in which the two $MnCO_5$ subunits are joined solely by a metal-metal single bond, provides an ideal systems to examine the competition between metal-metal and metal-ligand bond reactivity in the excited state chemistry of the transition metal carbonyl complexes.
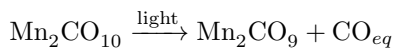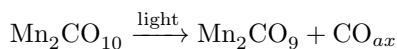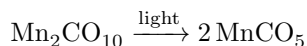
The photochemistry of dimanganese decacarbonyl, Mn_2CO_{10}, has been a subject of

considerable interest and it has been studied in a wide range of chemical environments. Photodissociation in gas phase [118, 119] and in liquid phase [120, 121, 122], see also the review in Ref. [123] occurs via two different dissociation pathways. The first pathway is through a homolytic cleavage of the Mn–Mn metal bond to yield two $MnCO_5$ subunits while the second pathway is through decarboxylation (removing) of one carbonyl group to produce Mn_2CO_9 and CO subunits as shown below. IR line spectra of Mn_2CO_{10} have been considered experimentally [124, 125] and theoretically as well [126]. In the present work we have studied the Mn_2CO_{10} system using quantum chemistry to get the geometry parameters as well the line spectra and comparing them with the previous work and the experimental results. The calculated IR vibrational frequencies using the harmonic approximation are comparable to the experimental results as will be shown in the results, Sec. 4.4. The anharmonic vibrational Hamiltonian for this system has been calculated and subsequently the IR line spectra are calculated as well.

Another application of the the laser control is controlling microscopic processes such as bond cleavage and bond formation, taking advantage of its intensity and bandwidth properties. In this laser control, bond-selective excitation using the tuned frequency of this bond occurs first. Afterwards, the intensity of the laser radiation increases to induce the bond-selective breakage. This way of control, also known as vibrationally mediated control, has been shown to be applicable to a few molecules such as HOOH [127] and C_2HD [128]. Witte et. al. have controlled molecular ground-state bond dissociation of polyatomic molecule $Cr(CO)_6$ by optimizing vibration ladder climbing [129]. Recently, coherent vibrational ladder climbing up to state $\nu = 6$ of the CO vibration in carboxy-hemoglobin has been established [130].

Besides of the advances in the field of control of nuclear dynamics, electronic quantum dynamics control has been verified. For instance, optimal control of population transfer in polyatomic molecules [131], coherent control of electric currents in superlattices and molecular wires [132] attosecond control of charge migration in small peptides [133] and magnetization switching control in quantum rings [134] has been reported.

An interesting aspect of dimanganese decacarbonyl system is its high symmetry. This leads to delocalized CO normal modes which are partly degenerated. There are three dissociative channels for Mn_2CO_{10} system can undergo upon radiation with light. These dissociative channels are illustrated as follow.

$$Mn_2CO_{10} \xrightarrow{\text{light}} 2\,MnCO_5$$

$$Mn_2CO_{10} \xrightarrow{\text{light}} Mn_2CO_9 + CO_{ax}$$

$$Mn_2CO_{10} \xrightarrow{\text{light}} Mn_2CO_9 + CO_{eq}$$

Here, we are aiming to investigate the possibility of CO bond breaking without using laser excitation directly but using the displaced ground state wavepacket instead.

1.9 Vibrational Ladder Climbing

With infrared IR laser pulses, one could excite only vibrational transitions while the molecule still remains in the electronic ground state during the entire interaction with the field. Actually, molecular dissociation via electronic ground state potential energy surface has some advantages, for example, avoiding the competition to ionization or elec-
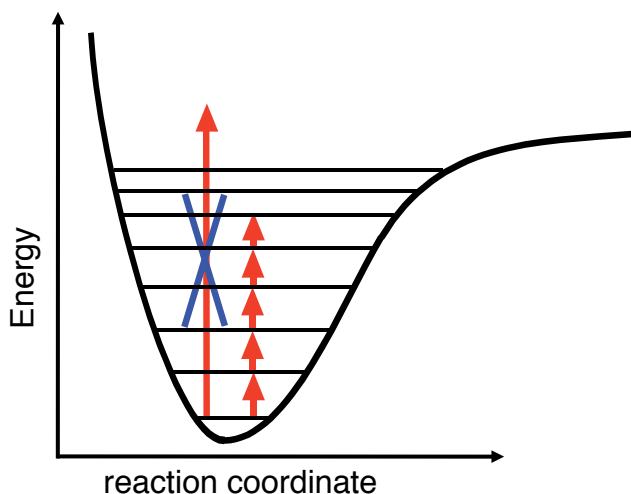
Fig. 1.9 *Anharmonic potential energy surface with energy levels. The long red arrow with blue cross on it means the direct excitation to higher vibrational states is inefficient. The short red arrows show the climbing of the vibrational ladder using a chirped IR laser pulse.*

tronic excitation of the system. In order to enhance the chemical reactivity of a system, for instance, to achieve a bond breakage of a certain bond laser excitation of the molecules into a specific highly excited vibrational state should be achieved. But, for such systems which are characterized by anharmonic dissociative potential energy surface, direct excitation and population of such a highly vibrational levels in a molecule with a laser field in the IR regime is inefficient, because of the small value of the transition dipole moment between the initial ground state and the target state. An example of such a anharmonic potential energy surface is plotted in Fig. 1.9. The more efficient way to drive this highly vibrational excitation is the step-wise excitation i.e. creation of a cascading transition from the initial state to the target state through a series of intermediate levels. this strategy is referred to as "*vibrational ladder climbing*". To achieve vibrational ladder climbing, there two ways: the first one is to use broad band short laser pulses which contain all frequencies in their spectrum, the second one is to use chirped laser pulse i.e. the carrier frequency is not constant with time since it keeps changing to compensate the vibrational energy level differences going up the anharmonic potential energy surface. Indeed, these transition frequencies decrease and become smaller while climbing the vibrational ladder due to the molecular anharmonicity. Therefore, the population efficiency of highly vibrational states can be increased dramatically by using negatively chirped pulse so that its high-frequency components, resonate with the starting transitions of the ladder, and its low frequency components resonate with the upper transitions of the ladder. Vibrational ladder climbing has been established in small molecules, such as $W(CO)_6$ [129] and NO [135], as well as a large molecule such as carboxy-hemoglobin [130, 136]. In this thesis, we are aiming to study IR-laser excitation of the collective carbonyl vibrations then to discuss the vibrational ladder climbing of the anharmonic potential energy surface of the Mn-complex.

1.10   Goals of This Work

This Section outlines the main objectives of this work:

1. The first goal of this work is the evaluation of the dynamics of Double Proton Transfer (DPT) using a simple model of DPT which was introduced by Smedarchina and coworkers [36, 39]. The parameters of this model are fitted to quantum chemistry results of the studied molecules. These dynamics involve the excitation of the wave packet using different kinds of laser pulses for instance optimal control theory (OCT) and pump dump IR laser. Then we shed some light on the mechanism of the DPT, i.e. whether it is of concerted or step-wise. And as a result of controlling the DPT by ultrafast IR laser pulse one could control the energy transfer through molecular photonic wires by changing the transition dipole moment accompanied by the tautomerization process between the global minima.

2. The second goal is the study of the dimanganese decacarbonyl $Mn_2(CO)_{10}$ system. This study involves the quantum chemical calculations for this system, obtaining the optimized structure and frequencies according to D_{4d} and D_{4h} point group symmetries. Quantum dynamic calculations are done for D_{4d} structure. Active CO normal modes are treated beyond harmonic approximation and the IR line spectrum is obtained. Furthermore, CPL in the IR regime is used to excite collective carbonyl vibrations of the degenerate E_1 modes in order to achieve the excitation of wavepacket circulation and vibrational ladder climbing. Dissociative PES as well as the possibility for the CO bond breaking will be discussed.

1.11 Structure of This Work

This work is organized as follows. Chapter 2 presents the theoretical concepts and methods that are relevant to the quantum chemistry and quantum dynamics investigations used in this thesis. A brief overview about the quantum chemistry part (Time-independent Schrödinger equation, Born-Oppenheimer approximation and solution of electronic Schrödinger Equation) is given in Sec. 2.1. Sec. 2.2 introduces the concept of the potential energy surface (PES) and some of its types. The theoretical part for quantum dynamics comes in Sec. 2.3. At the end of this Chapter, laser control techniques are introduced in section 2.4. Chapter 3 presents the model used for description of DPT in Sec. 3.2. Quantum dynamics using this model comes next describing the effect of the Hamiltonian parameters as well as the time durations on the optimal field and pathways of DPT. The computational chemistry part of molecules of interest are described in Sec. 3.6. The TDDFT calculations for the studied molecules are described and the transition dipole moment orientation is discussed. in Sec. 3.7.4. In Sec. 3.8.1 these quantum chemistry results are used to get the Hamiltonian parameters for asymmetric porphycene **4** and then the dynamics are investigated. In Chapter 4 the second part of this work is introduced which is concerning the $Mn_2(CO)_{10}$ complex. The quantum chemistry calculations part of $Mn_2(CO)_{10}$ is introduced Sec. 4.2.2. In Sec. 4.4, a 3D model of the IR active CO modes is extended to 10D PES and then the anharmonic IR-spectrum for CO vibrations is calculated. Wavepacket circulation around the principal axis of the molecule is introduced in 4.5. Different channels of CO bond breaking are presented in Sec. 4.6. Finally, the summary and outlook of this work are presented in Chapter 5.

CHAPTER 2

Theory

2.1 Overview

All of the work in this thesis has been done using quantum mechanics and and quantum dynamics. In this chapter, the theoretical concepts that have been used to obtain the results of this work are briefly reviewed. First, the quantum chemistry part is introduced. The time-independent Schrödinger equation (TISE) will be introduced in Sec. 2.2.1, after which the electronic and nuclear Schrödinger equations will be treated separately, within the Born-Oppenheimer approximations. Hartree-Fock and density functional theory as approximate methods for solving the electronic Schrödinger equation are discussed. In Sec. 2.2.3, the nuclear Schrödinger equation will be presented. Afterwards, potential energy surfaces (PES) and in particular the cartesian reaction surface (CRS) approach will be introduced. In the next section quantum dynamics background is discussed. The time-dependent Schrödinger equation (TDSE), Methods to solve it and finally laser control ways are discussed.

2.2 Quantum Chemistry

2.2.1 Time-Independent Schrödinger Equation

In order to perform quantum chemical calculation, the stationary or time-independent Schrödinger equation (TISE) should be solved.

$$H_{mol}\Psi(r,R) = E\Psi(r,R) \tag{2.1}$$

Here, r is the electronic cartesian coordinates and R is the nuclear cartesian coordinates. The solution of the TISE provides an energy spectrum E_λ and corresponding eigenfunctions, $\Psi_\lambda(r,R)$ of the molecule. The lowest energy state E_0 is called the ground state. The H_{mol} in Eq. 2.1, is the molecular Hamiltonian operator which describes the Coulomb interactions between electrons and nuclei of the system under consideration. In general, the complete molecular Hamiltonian for a molecule composed of N_{nuc} nuclei with masses M_n, momenta P_n and nuclear charges Z_n at Cartesian coordinates R_n surrounded by

N_{el} electrons with mass m_e , momenta p_j and charge e at coordinates r_j looks like:

$$H_{mol} = T_{el} + T_{nuc} + V_{el,el} + V_{nuc,nuc} + V_{el,nuc} \,. \tag{2.2}$$

It consists of kinetic energy terms for the electrons

$$T_{el} = \sum_{j=1}^{N_{el}} \frac{p_j^2}{2m_e}, \tag{2.3}$$

and the nuclei

$$T_{nuc} = \sum_{n=1}^{N_{nuc}} \frac{P_n^2}{2M_n}, \tag{2.4}$$

and of potential energy terms, including the Coulomb pair interaction between electrons

$$V_{el,el} = \sum_{i<j}^{N_{el}} \frac{e^2}{4\pi\epsilon_0|r_i - r_j|}, \tag{2.5}$$

between nuclei

$$V_{nuc,nuc} = \sum_{m<n}^{N_{nuc}} \frac{Z_m Z_n e^2}{4\pi\epsilon_0|R_m - R_n|}, \tag{2.6}$$

and between electrons and nuclei

$$V_{el,nuc} = -\sum_{n=1}^{N_{nuc}} \sum_{j=1}^{N_{el}} \frac{Z_n e^2}{4\pi\epsilon_0|r_j - R_n|}. \tag{2.7}$$

where the variable Z_n represents the atomic number of nucleus n, $|r_i - r_j|$ is the distance between electron i and j, $|R_m - R_n|$ is the distance between nucleus m and nucleus n. The Eq. 2.1 can be solved analytically only for small systems, for instance, hydrogen atom and one-electron ions. In order to solve this eigenvalue problem for more complex systems, some approximations should be applied.

2.2.2 Born-Oppenheimer Approximation

The TISE, Eq. 2.1 is not exactly solvable for many-electron/nuclei systems and approximations are required. The most successful one is the Born-Oppenheimer approximation [137]. Here the significant difference in mass between electrons ($m_e \sim 10^{-31} kg$) and nuclei ($M_n \sim 10^{-27} kg$) leads to the consideration that, the nuclei are fixed while the electrons are moving in the field of nuclei. Therefore, it is possible to separate electronic and nuclear motions. This separation simplifies the TISE because the total wave function $|\Psi\rangle$ can be written as a product of a nuclear wave function $|\Psi_{nuc}\rangle$ and an electronic wave function $|\Psi_{el}\rangle$ as follows

$$\Psi(r, R) \simeq \Psi_{el}(r, R) \, \Psi_{nuc}(R). \tag{2.8}$$

where the nuclear wave function Ψ_{nuc} depends only on the nuclear coordinates $R = \{R_n\}$, while the electronic wave function Ψ_{el} depends explicitly on the electronic coordinates $r = \{r_j\}$ as well as *parametrically* on the nuclear coordinates $R = \{R_n\}$. The electronic wave function Ψ_{el} is the solution of the electronic Schrödinger equation,

$$H_{el}|\Psi_{el}\rangle = E_{el}|\Psi_{el}\rangle. \tag{2.9}$$

where H_{el} is the electronic Hamiltonian operator and E_{el} is the electronic energy. Within the Born-Oppenheimer approximation, the kinetic energy of the nuclei T_{nuc} is neglected and the repulsion between the nuclei $V_{nuc,nuc}$ is a constant as far as the electrons are concerned. This constant term can be omitted, since any constant added to the Hamiltonian operator affects only the operator eigenvalues (energy) and has no effect on the operator eigenfunctions. The remaining terms in Eq. 2.2 form the electronic Hamiltonian, i.e. after omitting the nuclear kinetic and nuclear repulsion energy terms from the molecular Hamiltonian Eq. 2.2, which is given by,

$$H_{el} = T_{el} + V_{el,el} + V_{el,nuc}. \tag{2.10}$$

Since the electronic wave function $|\Psi_{el}\rangle$ depends explicitly on electronic r_j and parametrically on nuclear R_n coordinates, the corresponding energy E_{el} also depends parametrically on R_n. Solving this electronic Schrödinger equation for different values of R_n, one ends up with the potential energy surface (PES) for the nuclear motion.

$$V^{PES}(R_1, R_2, \cdots, R_{N_{nuc}}) = E_{el}(R_1, R_2, \cdots, R_{N_{nuc}}) + V_{nuc,nuc}(R_1, R_2, \cdots, R_{N_{nuc}}). \tag{2.11}$$

A potential energy surface is a mathematical relationship linking molecular structure with its energy. Minima on the potential energy surface can then be identified with the classical picture of equilibrium structures of molecules (reactant, product and intermediates); saddle points of first or second order are related to transition states.

2.2.3 Nuclear Schrödinger Equation

Using the Born-Oppenheimer approximation which used for solving the electronic Schrödinger equation, it is possible to obtain the nuclear Schrödinger equation

$$H_{nuc} \Psi(R_1, R_2, \cdots, R_{N_{nuc}}) = E \Psi(R_1, R_2, \cdots, R_{N_{nuc}})). \tag{2.12}$$

The nuclear Hamiltonian H_{nuc} that describes the vibrational, rotational and translational motion of the molecule depending on the electronic state el can be expressed as,

$$\begin{aligned} H_{nuc} &= T_{nuc} + E_{el}(R_1, R_2, \cdots, R_{N_{nuc}}) + V_{nuc,nuc}(R_1, R_2, \cdots, R_{N_{nuc}}) \\ &= T_{nuc} + V^{PES}(R_1, R_2, \cdots, R_{N_{nuc}}). \end{aligned} \tag{2.13}$$

and can be defined by the effective energy of the electronic terms V^{PES}, in company with the kinetic energy operator for the nuclei, T_{nuc} as defined in Eq. 2.2. Solutions of the nuclear Schrödinger equation, Eq. 2.12, describe the vibrations, rotations and translations of a molecule, whereas the nuclear energy, E , represents the total energy in the Born-Oppenheimer approximation and accounts for the electronic and vibrational energy of a molecule. Solution to the electronic and nuclear Shrödinger equations will be discussed in sections 2.3 and 2.5, respectively. Thus, solving the electronic problem will provide us with the PES which can be used to solve the nuclear Schrödinger equation and to investigate nuclear wavepacket dynamics.

2.3 Solution of the Electronic Schrödinger Equation

Solving the electronic time-independent Schrödinger equation (TISE) 2.9 for different nuclear coordinates provides single point energies which afterwards can be connected to each other giving the potential energy surface that depends on the nuclear coordinates. Solving the electronic Schrödinger equation numerically exactly is possible only for the

simplest molecules, but for larger molecules it is formidable. In order to solve it in a convenient way, approximations are needed. The Hartree-Fock approximation is one of the core approximations to solve the electronic Schrödinger equation for larger molecules.

2.3.1   Hartree-Fock Approximation

The Schrödinger equation Eq. 2.1 does not account for relativistic effects in which the spin is an important property of the electron. The electron spin may be introduced into the many-electron wave function in an ad hoc way by multiplying the wave function with a spin (up or down) function. The wave function for a single particle is called an orbital (labeled with index i). The wave function that describes the spatial distribution of an electron k is a spatial orbital $\Psi_i(r_k)$. Where r_k refers to the coordinates of electron k. To describe the electron completely, its spin is essentially to be specified. A wave function that describes both the spatial distribution of an electron and its spin is called a spin orbital $\chi_i(x_k)$. Here x refers to the spatial and spin coordinates of electron k. For a set of K orthonormal spatial orbitals, a set of 2K orthonormal spin orbitals can be constructed. The Hartree-Fock (HF) method [138, 139] has been viewed as an approximation in which the wave function is given by a single antisymmetric Slater determinant. This wave function is optimized by solving the Hartree-Fock equations iteratively in a procedure that is known as self consistent field (SCF).

Basis Sets

The spatial part ψ_i of the spin-orbitals is unknown, so it can be approximated in a way that each molecular spatial orbitals ψ_i are expressed as a linear combination of a finite set of prescribed one-electron functions known as basis functions $\phi_k(r)$ as introduced as follow. This is called the *linear combination of atomic orbitals* (LCAO) approximation,

$$\psi_i(r) = \sum_{k=1}^{M} c_{ik}\phi_k(r). \tag{2.14}$$

where c_{ik} are the coefficients of the molecular orbital expansions which provide the orbital description. There are two types of atomic basis functions. The first one is the Slater type orbitals (STO) which uses functions proportional to $e^{-\zeta r}$ where ζ is the Slater orbital exponent. They are labeled as hydrogen like atomic orbital $1s$, $2s$, and $2p_{xyz}$, etc. The other type of basis functions consists of Gaussian type orbital (GTO), also called primitive Gauss-functions. The main difference to the (STO) is that the variable r in the exponential function is squared $e^{(-\alpha r^2)}$. The basis functions $\psi_i(r)$ in Eq. 2.14 could be chosen to be STO or GTO. GTO's have the important advantage that all integrals in the computations can be evaluated explicitly without facing the very large numerical computation as STO's do. A Slater type orbitals reads:

$$S_{nml}^{\zeta}(r, \theta, \varphi) = Nr^{n-1}e^{\zeta r}Y_l^m(\theta, \varphi), \tag{2.15}$$

here N is the normalization constant. STOs are expensive to do multi-center two-electron integrals. So, Cartesian Gaussian-type-orbitals (GTO's) were used to overcome this problem.

GTOs or primitive Gauss-functions have the form:

$$G_{xyz}^{\alpha}(\mathbf{r}) = N_{xyz}^{\alpha}x^{n_x}y^{n_y}z^{n_z}e^{\alpha r^2}, \tag{2.16}$$

with normalization constant N and triple n_x , n_y , n_z set of integers; the sum $l =$

$n_x + n_y + n_z$ is used to classify the primitive Gauss-functions as s-type ($l = 0$), p-type ($l = 1$), d-type ($l = 2$), f-type ($l = 3$) orbitals, etc. The factor α in the exponent is Gaussian function exponent parallel to ζ in STO and determines the decay of the amplitude of the GTO with increasing radial distance. GTOs with large α are localized close to the nuclei, while GTOs with small α are rather diffuse. Due to the exponential dependence on r^2 , a GTO has a zero slope at the nucleus while a STO has a discontinuous derivative. Thus, a GTO does not represent the proper behavior of the wave function near the nucleus. Another failure of the GTO is that it falls off too rapidly far from the nucleus compared with an STO, and the tail of the wave function is consequently represented poorly. In order to achieve a more accurate description, linear combinations of primitive Gauss-functions $G^{\alpha}_{xyz}(r)$, so called contraction $\phi(r)$ are used:

$$\phi(r) = \sum_p d_p G^{\alpha}_{xyz}(r). \tag{2.17}$$

Here, d_p are coefficients and p is the length of the contraction.

For minimal basis set, one contracted basis functions ϕ is used to describe every atomic orbital. In fact, the minimal basis set is relatively inexpensive but quite inaccurate. The first step in improving upon the minimal basis set involves using two, three or four functions for each of the minimal basis functions like $double - zeta$, $triple - zeta$ and $quadruple - zeta$, respectively, and so forth. But, if one goes in this direction rather than adding functions of higher angular quantum number, the basis set would not be balanced.

Since the inner shell is not involved strongly in the chemical reactions they are kept contracted and the chemical bonding occurs through the valence orbitals, it is reasonable to split these valence orbitals only. A SV basis sets uses two basis functions for each valence atomic shell but only one basis function for each inner-shell atomic orbital. 6-31G is an example of a split-valence basis set in which the inner-shells are described by six GTOs, whereas the outer-shells are split into an expansion of three primitive GTOs and another primitive GTO.

The split-valence (SV) basis set at some point concerns a relatively poor energy for some elements. So, one could increases the efficiency of the basis set by fully optimization of the contracted GTOs especially the valence atomic orbitals i.e. de-contraction of the valence atomic orbitals and the re-optimization. An examples for these type of basis set are single zeta (SZ), double zeta (DZ) and triple zeta (TZ). TZVP [140, 141] basis set has been used for $Mn_2(CO)_{10}$ part since it gives reasonable results for the complexes of the transition metal elements.

Another way of improving the basis is that, by adding functions of high angular momentum *polarization functions* so that the atomic orbitals can become distorted, or polarized in the chemical bond formation. For example, d-type functions (3d) are added to the first and the second row elements and p-type (2p) functions are added to H-atom. These polarization functions are represented by double stars ($**$) or (d,p). An example is 6-31G(d,p) or 6-31** family of basis sets.

Also one can improve the basis set by adding one or two highly diffuse functions in order to have a proper description of the electron density away from the nuclei. These diffused functions are represented by ($+$ or $++$). An example for this type of basis set is 6-31G+(d,p) which has been used in this thesis in the DPT part.

Electron correlation

The energy which comes out from an HF calculation is higher than the exact value since the wave function is described by a single determinant which lacks the correlation

between electrons of opposite spin. The difference between the exact and the HF energy is defined as the correlation energy [142],

$$E_{(corr)} = E_{(exact)} - E_{(HF)} \tag{2.18}$$

As a result of HF neglecting of the correlation energy between electrons of opposite spin, the description of the electronic structure as well as the energy of the molecular system are not so efficient. There are different ways that consider the electron correlation energy. An efficient way of these ways is density functional theory (DFT).

2.3.2   Density Functional Theory

A completely different approach from the Hartree-Fock methods in which "*The HF wave functions lack electronic correlation*", is the Density Functional Theory (DFT). DFT is based on the Hohenberg-Kohn theorems [143]. The first Hohenberg-Kohn theorem (HK-I) states that the complete molecular potential V is a functional of the charge density $\rho(r)$ and since, in turn, the molecular potential is described completely by the Hamilton operator H, the full many particle ground state of the molecule Ψ is also a functional of $\rho(r)$ [144]:

$$\rho(r) \leftrightarrow V \leftrightarrow \Psi. \tag{2.19}$$

Therefore, it is possible to calculate the total electronic energy of the system E_{el} by minimizing the charge density functional,

$$E_{el}[\rho_{el}] = \langle \Psi_{el}[\rho_{el}] | H | \Psi_{el}[\rho_{el}] \rangle = min, \tag{2.20}$$

which depends on the electron density which reads:

$$\rho_{el}(r) = \sum_{i}^{N_{el}} |\psi_i(r)|^2, \tag{2.21}$$

where ψ_i is the spatial part of the single particle functions for the electron i. The second Hohenberg-Kohn theorem (HK-II) proves that the exact ground state density minimizes the total electronic energy of the molecular system. Since this is not the case the energy obtained from a trial charge density ρ represents an upper limit to the exact ground electronic state energy,

$$E[\rho] \geqslant E_{exact}^0, \tag{2.22}$$

which could be calculated if the exact electron density was known. This is nothing else than the variational principle. So the electronic energy is given as,

$$
\begin{aligned}
E[\rho(\mathbf{r})] &= T_s[\rho] + J[\rho] + E_{XC}[\rho] + E_{Ne}[\rho] \\
&= T_s[\rho] + \frac{1}{2} \int \int \frac{\rho(\mathbf{r}_1)\rho(\mathbf{r}_2)}{r_{12}} d\mathbf{r}_1 d\mathbf{r}_2 + E_{xc}[\rho] + \int V_{Ne} d\mathbf{r} \rho(\mathbf{r}) \\
&= -\frac{1}{2} \sum_{i}^{N} \langle \varphi_i | \nabla^2 | \varphi_i \rangle + \frac{1}{2} \sum_{i}^{N} \sum_{j}^{N} \int \int |\varphi_i(\mathbf{r}_1)|^2 \frac{1}{r_{12}} |\varphi_j(\mathbf{r}_2)|^2 d\mathbf{r}_1 d\mathbf{r}_2 \\
&\quad + E_{XC}[\rho] - \sum_{i}^{N} \int \sum_{A}^{M} \frac{Z_A}{r_{1A}} |\varphi_i(\mathbf{r}_1)|^2 d\mathbf{r}_1
\end{aligned}
\tag{2.23}
$$

Which is composed of several functionals terms: $T[\rho]$, which describes the kinetic energy of electrons; φ_i, are Kohn-Sham orbitals; $E_{Ne}[\rho]$, which describes the attraction between

the nuclei and the electrons; $J[\rho]$, which denotes the Coulomb repulsion between the electrons; and $E_{XC}[\rho]$, which represents the exchange correlation energy term. The latter is the only term that has no explicit form, i.e. is unknown. By applying the variational principle and choosing a certain condition for the orbital $\{\varphi_i\}$, which fulfill the minimization of energy under $\langle \varphi_i | \varphi_j \rangle = \delta_{ij}$ constrains, so, the Kohn-Sham equations can be derived,

$$\left(-\frac{1}{2}\nabla^2 + \left[\int \frac{\rho(\mathbf{r_2})}{r_{12}} + V_{XC}(\mathbf{r_1}) - \sum_A^M \frac{Z_A}{r_{1A}} \right] \right) \varphi_i$$
$$= \left(-\frac{1}{2}|\nabla^2| + V_{eff}(\mathbf{r_1}) \right) \varphi_i = \epsilon_i \varphi_i , \qquad (2.24)$$

which are again solved iteratively. These equations are differed from HF-equations in the form of the effective potential $V_{XC}(\mathbf{r_1})$ which is the potential due to the non-classical exchange-correlation energy and is expressed as:

$$V_{XC} = \frac{\delta E_{XC}[\rho]}{\delta \rho(r)}. \qquad (2.25)$$

The non-classical electron correlation energies E_{XC} involves all kind of electronic interactions which cannot be described exactly. If the exact correlation energy E_{XC} were known, then the solution of the Kohn-Sham equations would be exact for the total energy of the system. And, because it is not known, the art of a DFT calculation is to find a functional that describes this correlation energy well.

The Becke3LYP (B3LYP) hybrid functional is commonly used and it is a mixture of Hartree-Fock exchange with DFT exchange-correlation functional. In particular the DFT exchange-correlation functional consists of the Becke's 1988 exchange functional (B88 or B) [145] and the Lee-Yang-Parr (LYP) correlation functional [146]. All functionals are combined by three parameters indicated by the number 3 in B3LYP. The parameters are derived by fitting the results of DFT calculations for test systems to experimental data, for instance, thermodynamic and spectroscopic properties. The B3LYP exchange-correlation energy expression is:

$$E_{XC}^{B3LYP} = (1-a)E_X^{LSD} + a\,E_{XC}^{\lambda=0} + b\,E_X^{B88} + c\,E_C^{LYP} + (1-c)\,E_C^{LSD} \qquad (2.26)$$

Where, LSD is local spin-density approximation which is an unrestricted case of local density approximation LDA extension. The exchange-correlation terms are parameterized by a , b and c , with fixed values of 0.20, 0.72 and 0.81 respectively. The B3LYP level of theory has been used for the DPT part.

Another level of theory is used in this work for the $Mn_2(CO)_{10}$ part which is BP86. Where in BP86, Becke's 1988 exchange functional (B) is combined with Perdew's 1986 gradient corrected correlation functional method (P86) [147, 148]. The Becke's exchange-energy density is given as,

$$E_X = E_X^{LDA} - \beta \sum_\sigma \int \rho_\sigma^{4/3} \frac{x_\sigma^2}{(1 + 6\beta x_\sigma sinh^{-1}x_\sigma)} d^3r \qquad (2.27)$$

Where E_X^{LDA} is the Hartree-Fock exchange energy that approximated by so-called local density approximation, σ denotes electron spin either up or down, β is a constant, ρ_σ is the spin density and x_σ is dimensionless ratio which is given by $\frac{|\nabla \rho_\sigma|}{\rho_\sigma^{4/3}}$.

DFT has some advantages, It offers very good scaling of computational cost with

system size comparing to configuration interaction (CI) and Møller-Plesset perturbation theory. Obviously the DFT methods overcome one of the main disadvantages of ab initio methods such as Hartree-Fock: the complete neglect of electron correlations of different spin. However, this effect is taking into account approximately only since $E_{XC}[\rho]$ is not known.

2.3.3   Time-Dependent Density Functional Theory

The time dependent DFT(TD-DFT) method can be applied to excited state calculations. TD-DFT method is based on the fact that frequency dependent linear response of a finite system with respect to a time-dependent perturbation has discrete poles at the exact correlated excitation energies of the unperturbed system [149]. The mean polarizability $\alpha(\omega)$ is frequency dependent and describes the response of the dipole moment to a time-dependent electric field with frequency ω. Its relation to the electronic excitation energies $\omega_i = E_i^{el} - E_0^{el}$ and corresponding oscillator strength f_i is given by:

$$\alpha(\omega) = \sum_i \frac{f_i}{\omega_i^2 - \omega^2}. \tag{2.28}$$

and the sum runs over all excited states i of the system. Eq. 2.28 shows easily that the dynamic mean polarizability $\alpha(\omega)$ diverges for $\omega_i = \omega$, i.e., has poles at the electronic excitation energies ω_i. In the Kohn-Sham scheme, the exact linear response can be expressed as the linear density response of a non-interacting systems. Since the excitation energies in TD-DFT are derived in terms of the electronic ground state orbitals, sometimes they may not describe correctly the excited states of the molecule. The TD-DFT method has been applied in this work for the calculation of excitation energies for the case study of porphycenes.

2.4   Potential Energy Surface

The concept of a PES has been introduced in Sec. 2.2.2. The PES is a result of the separation of the nuclear and electronic motion as introduced by the Born-Oppenheimer approximation and defined in Eq. 2.11. The PES is the key quantity needed to investigate chemical reaction dynamics or more generally the nuclear motions of the system. $V^{PES}(R)$ in Eq. 2.11 is a function in $3N_{nuc}$ nuclear coordinates R. Since the system is isolated from the environment, the total translation energy as well as the rotation energy can be neglected. Consequently, there are $3N_{nuc}-6$ and $3N_{nuc}-5$ coordinates necessary to describe the energetics for non-linear and linear molecules, respectively.

Once $V^{PES}(R)$ has been obtained, one can analyze its properties in forms of first and second derivatives. In general $V^{PES}(R)$ is a function of all $3N_{nuc}$ nuclear coordinates R (recall the notation $R = (R_1, \cdots, R_{3N_{nuc}})$). The negative gradient of the PES is expressed as,

$$\mathbf{f} = -\nabla V^{PES}(R) = \left\{ \partial V^{PES}(R)/\partial R_1, \cdots, \partial V^{PES}(R)/\partial R_{3N_{nuc}} \right\}. \tag{2.29}$$

and it is the force acting on the atoms. Another quantity of great interest is the $3N \times 3N$ force constant matrix or Hessian matrix $\mathbf{K}$ which is expressed as,

$$\mathbf{K}_{mn} = \frac{\partial^2 V^{PES}(R)}{\partial R_m \partial R_n} \qquad (m, n = 1, \cdots, 3N_{nuc}). \tag{2.30}$$

The points in the PES for which the gradient of the potential is zero, $\nabla V^{PES}(R) = 0$

are called stationary points, which could be minima or maxima. This can be identified by looking at the eigenvalues of the Hessian matrix. In the Hessian matrix, there are six eigenvalues equal to zero. The remaining $3N - 6$ correspond to the vibrational degrees of freedom. If all eigenvalues of the Hessian matrix are positive so we are at a minimum of the potential energy surface. Otherwise, we are at a maximum (stationary saddle point of order n, where n is the number of negative frequencies). Going beyond the harmonic approximation for large systems is not possible keeping all degrees of freedom since this is computationally very demanding. So specific approximations should be invoked. One of these approximations is cartesian reaction surface (CRS) [150].

Harmonic Approximation

The cartesian Hamiltonian for a system of N nuclei, when expressed in a full set of f nuclear coordinates $(3N_{nuc})$ where $(f = R_1, \cdots, R_{3N_{nuc}})$, and momenta $P_{R,f}$, is expressed as:

$$H = T + V = \sum_{f=1}^{N_f} \frac{P_{R,f}^2}{2M_f} + V(R). \tag{2.31}$$

Suppose that, we have reached a stationary point $R_f^{(0)}$ that corresponds to a global minimum on the potential energy surface. Within the harmonic approximation, we restrict ourself to small amplitude displacements, $\triangle R_f = R_f - R_f^{(0)} (f = 1, \cdots, 3N)$ of the nuclear coordinates for a given electronic state. Thus the $3N$-dimensional PES $V^{PES}(R)$ can be approximated by a second order Taylor expansion with respect to the reference equilibrium geometry $\{R_f^{(0)}\}$ as follows:

$$V^{PES}(R_f) \approx V^{PES}(R_f^{(0)}) - \sum_{f=1}^{N_f} f_n \triangle R_n + \sum_{m,f=1}^{N_f} \frac{1}{2} \mathbf{K}_{mf} \triangle R_m \triangle R_f \tag{2.32}$$

Since we are at the stationary point, the second term (the gradient of the PES) vanishes. Substituting Eq. 2.32 into Eq. 2.13, and according to Eq. 2.8, the Hamiltonian for the nuclear DOF in the adiabatic approximation can be written as,

$$H = V^{PES}(R_f^{(0)}) + \sum_{f=1}^{N_f} \frac{P_f^2}{2M_f} + \sum_{m,f=1}^{N_f} \frac{1}{2} \mathbf{K}_{mf} \triangle R_m \triangle R_f \tag{2.33}$$

In order to switch to the normal modes coordinates, one should introduce mass-weighted cartesian coordinates ξ_f and their conjugated momenta $p_{\xi,f}$ as well as the Taylor expansion coefficients in Eq. 2.32:

$$\xi_f = \sqrt{M_f} \triangle R_f, \qquad p_{\xi,f} = \frac{p_{R,f}}{\sqrt{M_f}} \tag{2.34}$$

$$\tilde{f}_f = \frac{f_f}{\sqrt{M_f}}, \qquad \tilde{\mathbf{K}}_{mf} = \frac{K_{mf}}{\sqrt{M_f M_m}} \tag{2.35}$$

Substituting the Eq. 2.34 and Eq. 2.35 in 2.33, one obtains the following expression for the nuclear Hamiltonian,

$$H = V^{PES}(R_f^{(0)}) + \frac{1}{2} \left[\sum_{f=1}^{N_f} p_{\xi,f}^2 + \sum_{m,f=1}^{N_f} \tilde{\mathbf{K}}_{mf} \xi_m \xi_f \right], \tag{2.36}$$

The first term in Eq. 2.36 can be omitted since it is just a constant that shifts the energy levels of the Hamiltonian so we have,

$$H = \frac{1}{2} \left[\sum_{f=1}^{N_f} p_{\xi,f}^2 + \sum_{m,f=1}^{N_f} \tilde{\mathbf{K}}_{mf} \xi_m \xi_f \right] , \qquad (2.37)$$

From Eq. 2.37, it is that, the individual degrees of freedom are still coupled in this representation through the bilinear term $\tilde{\mathbf{K}}_{mf}$. Since the harmonic approximation is applied for small amplitude displacement, one can eliminate the bilinear coupling term and switch to normal mode coordinates q_ξ. The normal mode Hamiltonian follows as,

$$H^{(fm)} = \frac{1}{2} \sum_{\xi=1}^{3N-6} \left(p_\xi^2 + \omega_\xi^2 q_\xi^2 \right) . \qquad (2.38)$$

where ω_ξ are the normal mode frequencies which are the nonzero eigenvalues of the Hessian matrix Eq. 2.35. It can be seen from Eq. 2.38 that the nuclear motion can be understood as a superposition of independent harmonic vibrations around the equilibrium positions $\{R_n^{(0)}\}$. Diagonalization of the Hessian matrix leads to six eigenvalues being zero along with $3N - 6$ normal mode frequencies. In fact the normal mode vibrations do not lead to any translation or rotation of the molecule. Having a vibrational (normal modes) Hamiltonian at hand one could use it to obtain the anharmonic frequencies for the system under consideration. The anharmonic frequencies are calculated as follows.

Since one is interested in the anharmonicity of the PES in the vicinity of a minimum, the PES can be expressed in terms of normal mode coordinates which will be denoted by V^{PES}. Of course, not all normal modes are treated anharmonically. Therefore, the normal modes have been divided into two sets. Active normal modes s_i which are treated beyond the harmonic approximation are separated from the remaining harmonic bath modes Z_i. In fact, not all the bath modes Z_i are coupled strongly with the active modes s_i. The criteria for choosing the bath modes are the force $\mathbf{f}(s)$ exerted by the active modes on the bath modes. After some rearrangement of Eq. 2.36, the total hamiltonian is given by,

$$H = \frac{1}{2} \sum_{i=1}^{N_{active}} P_{s_i}^2 + \mathbf{V}(\{s_i\}) + \frac{1}{2} \sum_{j=1}^{N_{bath}} P_{Z_j}^2 - \sum_{j}^{N_{bath}} f_j(\{s_i\}) Z_j + \frac{1}{2} \sum_{j}^{N_{bath}} \omega_{Z_j}^2 Z_j^2, \quad (2.39)$$

Once the total Hamiltonian is set, one can use the dipole-dipole autocorrelation function for the wavepacket propagation to obtain the anharmonic frequencies. In the second part of this thesis which concerning $Mn_2(CO)_{10}$, the anharmonic frequencies for CO modes of that complex have been calculated, Sec. 4.4.

2.4.1   Cartesian Reaction Surface

The properties of the nuclear motion in the vicinity of a minimum (equilibrium configuration) have been discussed in the previous section. But this not the case if a part of the molecule is moved a part from the system like what is happening in chemical reactions e.g. isomerization reactions or bond dissociation reactions. Now it becomes important to describe the properties of the PES away from the stationary points. In practice, however, the case that all DOF move appreciably during a reaction is rather unlikely. To this end, one should think of another way of approximation that can take into account all these points. This kind of approximation is the cartesian reaction surface (CRS) [150, 108].

In this approximation the DOF are separated into *active* $s = (s_1, \cdots, s_{N_{rc}})$ and *bath* or *substrate* $3N_{nuc} - N_{rc}$ coordinates. These active coordinates perform a large amplitude motion. And, they are separated from the remaining $3N_{nuc} - N_{rc}$ substrate coordinates Z. The key assumption is that, the bath coordinates stay close to their minimum and exert a small amplitude motion through the reaction.

Since the substrate atoms execute only a small amplitude motion around their equilibrium positions $V^{PES}(R) = V(\mathbf{s}, \mathbf{Z})$ can be expanded in a Taylor series up to second order in terms of the deviations $\triangle \mathbf{Z}(\mathbf{s}) = (\mathbf{Z} - \mathbf{Z^{(0)}})$ as follows:

$$V^{PES}(R) \approx V(\mathbf{s}, \mathbf{Z^{(0)}}) + \left(\frac{\partial V(\mathbf{s}, \mathbf{Z})}{\partial \mathbf{Z}} \right)_{Z=Z^{(0)}(s)} \triangle \mathbf{Z}(\mathbf{s})$$

$$+ \frac{1}{2} \triangle \mathbf{Z}(\mathbf{s}) \left(\frac{\partial^2 V(\mathbf{s}, \mathbf{Z})}{\partial \mathbf{Z} \partial \mathbf{Z}} \right)_{Z=Z^{(0)}(s)} \triangle \mathbf{Z}(\mathbf{s}) \tag{2.40}$$

where Z^0 is the reference configuration at which one should calculate the first derivative (force) and the second derivative (Hessian) of the potential energy surface and $V(\mathbf{s}, \mathbf{Z})$ is the multi-dimensional potential energy surface (PES). The spectator DOF are frozen at some reference geometry which is in our study the equilibrium configuration Z^0. The second term in Eq. 2.40 is the force exerted on the bath DOF Z due to the displacement of the active DOF away from its equilibrium position:

$$\mathbf{f}(s) = - \left(\frac{\partial V(\mathbf{s}, \mathbf{Z})}{\partial \mathbf{Z}} \right)_{Z=Z^{(0)}}, \tag{2.41}$$

and, the third term in Eq. 2.40 describes the change in the Hessian matrix

$$\mathbf{K}(s) = \frac{1}{2} \left(\frac{\partial^2 V(\mathbf{s}, \mathbf{Z})}{\partial \mathbf{Z} \partial \mathbf{Z}} \right)_{Z=Z^{(0)}}. \tag{2.42}$$

The substrate atoms are considered to perform small amplitude harmonic motion and normal modes can be introduced by applying the transformations Eq. 2.34 and Eq. 2.35 with respect to the fixed reference configuration $\mathbf{Z^0}$. Consequently, the CRS Hamiltonian can be expressed as,

$$H^{(CRS)} = \frac{1}{2} \sum_i^{N_{ac}} P_{si}^2 + \mathbf{V}(s, Z^{(0)}(s)) + \frac{1}{2} \sum_i^{N_{bath}} P_{qi}^2 - \sum_i^{N_{bath}} F_i(s) q_i + \frac{1}{2} \sum_{i,j=1}^{N_{bath}} q_i K_{ij}(s) q_i. \tag{2.43}$$

which can be written in a simpler form as follow,

$$H^{(CRS)} = \mathbf{T}_s + V(\mathbf{s}, \mathbf{Z^{(0)}}(\mathbf{s})) + \mathbf{T}_q - \mathbf{F}(\mathbf{s})\mathbf{q} + \frac{1}{2}\mathbf{q}\mathbf{K}(\mathbf{s})\mathbf{q}. \tag{2.44}$$

Where, $\mathbf{T}_s$ and $\mathbf{T}_q$ is the diagonal kinetic energy operator for the reaction coordinates (active modes) and bath modes, respectively. Further $\mathbf{f}$ and $\mathbf{K}$ are the mass-weighted force exerted by the active mode displacement on the bath modes and the mass-weighted Hessian matrix which includes the coupling between different substrate modes, respectively. Finally, the $V(\mathbf{s}, \mathbf{Z^{(0)}})$ is the anharmonic PES. Within harmonic approximation, Eq. 2.43 and Eq. 2.44 returned back to Eq. 2.39.

Of course, not all the bath modes will couple strongly with the reaction coordinates. and the question needs to be addressed, which substrate modes are most strongly coupled to the reaction coordinates. Here, the reorganization energy of the substrate modes is a convenient measure. It combines both information about the forces and the Hes-

sian matrix entering in Eq. 2.43. The reorganization energy is the energy required to shift the oscillators to their equilibrium position for a given value of the reaction coordinates. Defining the displacement of the substrate modes with respect to their equilibrium position as,

$$\mathbf{q}^{(0)}(\mathbf{s}) = -[\mathbf{K}(s)]^{-1}\mathbf{F}(s). \tag{2.45}$$

The reorganization energy is defined as,

$$E_\lambda(\mathbf{s}) = \frac{1}{2}\mathbf{q^{(0)}}(\mathbf{s})\mathbf{K}\,\mathbf{q^{(0)}}(\mathbf{s}). \tag{2.46}$$

In this work the reorganization energy has been calculated using the assumption that the frequencies do not change [108], so the reorganization energy becomes

$$E_\lambda^i = \frac{1}{2}\left[\frac{F_i(\mathbf{s})}{\omega_i}\right]^2. \tag{2.47}$$

The anharmonic PES $V(\mathbf{s}, \mathbf{Z^{(0)}})$ can be obtained by displacement of the large amplitude coordinates away from their minimum structure. Let there are three active modes. The anharmonic PES can be expressed as follows

$$V(\mathbf{s_1}, \mathbf{s_2}, \mathbf{s_3}) = V^{(1)} + V^{(2)} + V^{(3)} \tag{2.48}$$

Where $V^{(1)}$ represents a one mode potential for the uncoupled modes,

$$V^{(1)} = \sum_i V^{(1)}(s_i), \tag{2.49}$$

$V^{(2)}$ represents the two mode potential for the coupled two modes,

$$V^{(2)} = \sum_{i<j} V^{(2)}(s_i, s_j), \tag{2.50}$$

and $V^{(3)}$ represents the three mode potential for the coupled three modes,

$$V^{(3)} = V^{(3)}(s_i, s_j, s_k), \tag{2.51}$$

and so forth if there are more active degrees of freedom.

2.5 Quantum Dynamics

2.5.1 The Time-Dependent Nuclear Schrödinger Equation

The solution of the time-independent nuclear Schrödinger equation yields the vibrational eigenstates and eigen energies of the molecular system. To describe the time-dependent properties of the model system (its interaction with a time-dependent laser field) it is necessary to solve the time-dependent nuclear Schrödinger equation (TDSE). The resulting wave packet dynamics are obtained by solving the TDSE numerically as it will be discussed in the next sections. The nuclear Schrödinger equation reads,

$$i\hbar\frac{\partial}{\partial t}|\Psi_{nuc}(t)\rangle = H(t)|\Psi_{nuc}(t)\rangle \tag{2.52}$$

the H(t) Hamiltonian is time dependent and has the form;

$$H(t) = H_{nuc} + H_{\text{field}}. \tag{2.53}$$

The time-dependent Hamiltonian consists of the nuclear Hamiltonian which is given by Eq. 2.13 and a time-dependent interaction Hamiltonian term $H_{\text{field}}(t)$ arising from the interaction of the molecular dipole moment $\boldsymbol{\mu}$ with an external electromagnetic field $\mathbf{E}(t)$ and is given by,

$$H_{field}(t) = -\boldsymbol{\mu}\,\mathbf{E}(t) \tag{2.54}$$

The kinetic energy operator T_{nuc} in its simplest form reads:

$$T_{nuc} = -\frac{1}{2m_1}\frac{\partial^2}{\partial R_1^2} - \frac{1}{2m_2}\frac{\partial^2}{\partial R_2^2} - \cdots - \frac{1}{2m_n}\frac{\partial^2}{\partial R_n^2}. \tag{2.55}$$

where R_i are coordinates and the m_i are the corresponding masses. The coordinates R_i can be Cartesian, normal or internal coordinates. Later on of the chapter, the index of "*nuc*" will be removed for simplicity. There are several numerical methods to solve the TDSE Eq. 2.52. The method that is used to solve TDSE in this thesis is Multi Configuration Time Dependent Hartree (MCTDH).

2.5.2 Multi Configuration Time Dependent Hartree

Once the quantum chemical calculations are done and the PES is obtained, the TDSE Eq. 2.52 can be solved. Many numerical techniques were developed for solving the TDSE numerically [151]. Several specific integrators have been developed to solve TDSE for example, split-operator [152, 153], Chebyshev [154], and Lanczos scheme [155].

The standard methods developed to solve TDSE, Eq. 2.52 were based on a time propagation scheme where the wave function of the system is expanded in a time-independent primitive basis set, as follows:

$$\Psi(R_1, \cdots, R_f, t) = \sum_{j_1=1}^{N_1} \cdots \sum_{j_f=1}^{N_f} C_{j_1, \cdots, j_f}(t) \prod_{k=1}^{f} \chi_{j_k}^{(k)}(R_k) \tag{2.56}$$

Here f specifies the number of degrees of freedom, $(R_1, \cdots, R_f)$ are the nuclear coordinates, $C_{j_1, \cdots, j_f}(t)$ denote the time-dependent expansion coefficients, and $\chi_{j_k}^{(k)}$ are the orthogonal time-independent primitive functions for degree of freedom k. For evaluation of the action of H onto Ψ, these basis functions $\chi_{j_k}^{(k)}$ are often chosen to be DVR/FBR (grid) functions of collocation method, for more details see Ref. [156]. Each product of primitive functions, actually a Hartree product, is defined as a configuration.

The equations of motion for the coefficients $C_{j_1, \cdots, j_f}(t)$ can be derived from the Dirac-Frenkel variational principle [157, 158]:

$$\left\langle \delta\Psi \left| \mathbf{H} - i\hbar\frac{\partial}{\partial t} \right| \Psi \right\rangle = 0, \tag{2.57}$$

The advantage of applying a variational principle to obtain the equations of motion is that the temporal derivative of the wave packet at each time, evaluated by the Hamiltonian, will be the one that will approach variationally the solution of the time-dependent Schrödinger equation. Inserting Eq. 2.56 in the previous equation leads to:

$$i\hbar\dot{C}_J = \sum_L \langle \chi_J | \mathbf{H} | \chi_L \rangle C_L, \tag{2.58}$$

where the multiindex $J = j_1 \cdots j_f$, has been established and the same for L and $\langle \chi_j | \mathbf{H} | \chi_L \rangle$ is the matrix representation of the Hamiltonian given in the product basis set $\{\chi_{j_k}^{(k)}\}$. Eq. 2.58 forms a system of coupled linear first-order ordinary differential equations which can be solved by integrators like, split-operator [152, 153], Chebyshev [154], and Lanczos methods [155]. The use of these methods in wave packet propagation are feasible if the dimensionality of the system is small. Assuming the same number $N_k = N$ of grid points for all k, the computational effort of this numerically exact calculation grows exponentially with the number of degrees of freedom f and becomes proportional to fN^{f+1}. In principle, this scaling behavior restricts the applications of this standard method to systems with less than five or six degrees of freedom.

The approximated method used in this thesis to solve Eq. 2.52 is the Multi Configuration Time Dependent Hartree approach (MCTDH) [156].

In the MCTDH scheme, the wave function which is used to describe the molecular dynamics of a system with f degrees of freedom is defined as a linear combination of time-dependent configurations that adapt to the wave packet according to the Dirac-Frenkel variational principle. The MCTDH wave function ansatz is:

$$\Psi(R_1, \cdots, R_f, t) = \sum_{j_1=1}^{n_1} \cdots \sum_{j_f=1}^{n_f} A_{j_1, \cdots, j_f}(t) \prod_{k=1}^{f} \phi_{j_k}^{(k)}(R_k, t) \tag{2.59}$$

$$= \sum_{J} A_J \Phi_J \tag{2.60}$$

where $(R_1, \cdots, R_f)$ are the nuclear coordinates, $A_{j_1, \cdots, j_f}$ denote the MCTDH expansion coefficients, and $\phi_{j_k}^{(k)}$ are the n_k expansion functions for each degree of freedom k, known as single particle functions (SPFs). Eq 2.60 is used for simplification of notations by establishing the composite index J and configuration Φ_J.

$$A_J = A_{j_1} \cdots A_{j_f} \quad \text{and} \quad \Phi_J = \prod_{k=1}^{f} \phi_{j_k}^{(k)}. \tag{2.61}$$

Each single particle function is expanded into a linear combination of time-independent basis (grid) functions $\chi_{i_k}^{(k)}(R_k)$ as follows.

$$\phi_{j_k}^{(k)}(R_k, t) = \sum_{i_k=1}^{M_k} c_{j_k, i_k}(t) \chi_{i_k}^{(k)}(R_k). \tag{2.62}$$

Here M_k is the number of grid points and the time-independent basis functions $\chi_{i_k}^{(k)}(R_k)$ per each degree of freedom ranges from $1 \rightarrow M_k$. Setting $n_1 = \cdots = n_f = 1$ in Eq. 2.56 one arrives at the TDH wave function and for $n_1 = \cdots = n_f = M_k$ one reaches the exact expansion of the wave function. This ansatz for the MCTDH wave function looks similar to the ansatz for the standard method. The only difference here is that, the SPFs are time dependent.

The efficiency of the numerical calculations depend in a great part on the choice of the basis functions. The discrete variable representation (DVR) is a straightforward method for representing the wavefunctions and operators. In DVR, the wave function is expanded in a set of basis functions that have the feature of diagonalizing the potential and in turn, the kinetic energy operator may be integrated analytically and consequently the matrix element is evaluated in an efficient way.

DVR functions have been used to expand the SPFs, which are then called *primitive*

basis functions as presented in Eq. 2.62. The transformed Hamiltonian, kinetic energy and potential energy in DVR forms reads,

$$\mathbf{T}^{DVR} = \mathbf{U}^{\dagger}\mathbf{T}\mathbf{U}, \tag{2.63}$$

$$\mathbf{V}^{DVR} = \mathbf{U}^{\dagger}\mathbf{V}\mathbf{U} \tag{2.64}$$

Where $\mathbf{U}$ is unitary transformation matrix. There are number of DVRs can be used for different type of coordinates. For instance, the harmonic oscillator DVR is used for vibrational motion. The harmonic oscillator DVR functions read,

$$\chi_j(R) = (2^j j!)^{-1/2} (m\omega)^{1/4} H_j(\sqrt{m\omega}(R - R_{eq})) \exp\left(-\frac{1}{2} m\omega(R - R_{eq})^2\right) \tag{2.65}$$

Here, H_j denotes the *jth* Hermite polynomial. The harmonic oscillator DVR primitive basis function is chosen for the wave function description in this thesis.

Applying the Dirac-Frenkel variational principle Eq. 2.57 onto Eq. 2.59 gives the following equations of motions (EOM) of the MCTDH scheme,

$$i\hbar\dot{A}_J = \sum_L \langle \Phi_J | H | \Phi_L \rangle A_L, \tag{2.66}$$

$$i\hbar\dot{\boldsymbol{\phi}}^{(k)} = \left(1 - P^{(k)}\right) \left(\boldsymbol{\rho}^{(k)}\right)^{-1} \langle \mathbf{H} \rangle^{(k)} \boldsymbol{\phi}^{(k)}. \tag{2.67}$$

Here $H_{JL} = \langle \Phi_J | H | \Phi_L \rangle$ is Hamiltonian operator represented in the basis of Hartree products. $P^{(k)}$ is the single particle projection operator onto the space spanned by SPFs. And, the operator $(1 - \rho^{(k)})$ assures that the time derivative of the SPFs is orthogonal to the space spanned by the functions.

Defining a single-hole function, $\Psi_l^{(k)}$, which is the wave function associated with *jth* SPF of the *kth* particle. As a consequence of this, the total wave function reads

$$\Psi = \sum_l \phi_l^{(k)} \Psi_l^{(k)} \tag{2.68}$$

Based on the notation of the single-hole function, the mean-field operator matrix $\langle \hat{\mathbf{H}} \rangle^{(k)}$ in Eq. 2.67 can be written as

$$\langle \mathbf{H} \rangle_{jl}^{(k)} = \langle \Psi_j^{(k)} | H | \Psi_l^{(k)} \rangle \tag{2.69}$$

and the density matrix $\boldsymbol{\rho}^{(k)}$ in Eq. 2.67 can be written as

$$\rho_{jl}^{(k)} = \langle \Psi_j^{(k)} | \Psi_l^{(k)} \rangle \tag{2.70}$$

For more details for EOMs derivation see Ref. [156].

In MCTDH there are two sets of equation of motions Eq. 2.66 and Eq. 2.67 which correspond to the $A_{j_1, \cdots, j_f}$ coefficients and the $\phi_{j_k}^{(k)}(R_k, t)$ functions and are called the A and $\boldsymbol{\phi}$ vectors ,respectively, instead of one set of EOMs in the standard methods, Eq. 2.58.

The efficiency and accuracy of the MCTDH method strongly depends on the algorithm used for solving the equations of motion Eq. 2.66 and Eq. 2.67 which are a system of coupled non-linear ordinary differential equations of first order. The *variable mean-field* (VMF) scheme is used to solve these non-linear ordinary differential equations. In the VMF scheme an Adams-Bashforth-Moulton (ABM) predictor-corrector integrator performs most efficiently in integrating of the MCTDH EOMs, Eq. 2.66 and Eq. 2.67.

In this thesis the VMF scheme has been used for time-dependent Hamiltonians. But, the disadvantages of this integrator scheme is that time demanding since it needs small integration steps.

The MCTDH package provides a robust integrator scheme which specifically developed for the numerically efficient solutions for Eq. 2.66 and Eq. 2.67. This integrator is the so-called *Constant mean-field* (CMF) [159]. In the CMF integration scheme the fact is that often the Hamiltonian matrix elements $H_{JL} = \langle \Phi_J |H| \Phi_L \rangle$, as well as the products of the inverse density and mean field matrices, $(\boldsymbol{\rho}^{(k)})^{-1}\langle \mathbf{H} \rangle^{(k)}$, change much slower in time than the MCTDH coefficients and single-particle functions. So one could you use wider meshed time discretization for the propagation and as a result, over come the time demanding problem of the VMF. With the CMF integrator scheme, the differential equation for the A-vector, Eq. 2.66, turns into a set of linear equations with constant coefficients, which can be solved most efficiently by using the short iterative Lanczos (SIL) method or Lanczos-Arnoldi integrators as implemented in [160]. Similarly, the differential equation for the single-particle functions, Eq. 2.67, splits up into subsets of uncoupled, but still non-linear equations (due to the projection operator $P^{(k)}$, which can be solved by using the implemented Bulirsch-Stoer (BS) extrapolation method. CMF scheme has been used in this work for the propagations of the time-independent Hamiltonian.

The accuracy of an MCTDH calculation depends on both the size of the primitive and the single-particle bases. The MCTDH package provides a number of analysis programs to check the convergence. For checking the primitive basis size, one could evaluate the population of the primitive basis functions over the boundaries of the grid points. If this sum over grid points is close to zero, these grid points can be removed without affecting the calculations quality.

With respect to the single-particle function basis size, we return back to the density matrix $\boldsymbol{\rho}^{(k)}$ in Eq. 2.67. This density matrix is the transposed of the matrix representation of the density operator $\rho^{(k)}$ in the set of the SPFs. The diagonalization of this operator $\rho^{(k)}$ yields the natural populations and natural orbitals [161] which are eigen values and eigen vectors, respectively, of $\rho^{(k)}$ operator. As a result of the thumb rule, one could say that, when the natural orbital population (NOP) of the highest (least populated) is below 1 % (i.e. a population below 0.01), the calculation is of reasonable quality. In this work, NOPs are used as an indication for the convergence of the calculations. Here, the largest NOP for the highest number of SPFs for all degrees of freedom will be given.

2.5.3 Stationary Eigenstate Calculations

The vibrational stationary eigenfunctions have to be obtained explicitly in order to study the population dynamics of the eigenstates. These eigenstates can be evaluated by solving the stationary, vibrational Schrödinger equation Eq. 2.12. These vibrational eigen states can also be generated by the relaxation method [162, 163]. In that method, the basic idea is to propagate the vibrational wavepacket in the imaginary time domain $t = -i\tau$ to decrease the energy of an initial guess wave packet to approach the ground state energy. In other words, the time in the time-dependent Schrödinger equation Eq. 2.52 is replaced by an imaginary one $t = -i\tau$. Under this condition, the solution of Eq. 2.52 is given by:

$$\Psi(\tau) = \sum_n c_n e^{-E_n \tau / \hbar} \Psi_n(0). \tag{2.71}$$

Actually, the formal equation shows that, each eigenfunction relaxes to zero at a rate that is proportional to its corresponding eigenvalue. This means that the slower relaxing ground state persists for the longest time. The same idea can be used to get excited

states. The first excited state is obtained by projecting out the ground state $\Psi_0(\tau = 0)$ from the Hilbert space and this means that, the first excited state becomes the new ground state in the new space. If $\mathbf{P}_0 = |\Psi_0\rangle\langle\Psi_0|$ is the projector operator for the ground state, $(1 - \mathbf{P}_0)\Psi_0(\tau = 0)$ is the new ground state for the new space with the operator $\mathbf{H}_1 = (1 - \mathbf{P}_0)\mathbf{H}(1 - \mathbf{P}_0)$. Continuing this procedure in order to obtain the $n - th$ excited states, one should get all $n - 1$ lower energy states first and then project them out.

In MCTDH package the ground state is obtained by relaxation while the excited states are obtained by so called improved relaxation [163, 164]. The improved relaxation method works as follow. First one has to use an initial guess which should be close to the vibrational state of interest (in other words, the initial guess should have a valuable overlap with the desired excited state). Then the Hamiltonian is diagonalized in the basis of the configurations of the initial state to obtain the expansion coefficients for the desired eigenstate expressed in the initial SPF bases. Afterwards, the SPFs are optimized by relaxation over a short time interval and the Hamiltonian matrix is rebuilt in the new Hartree products and diagonalized. Finally, the whole procedure is repeated till the convergence is reached.

2.5.4   Autocorrelation Function

Another quantity of frequent interest is autocorrelation function. The autocorrelation function $C(t)$ is often considered to monitor the evolution of the time-dependent wave function. Autocorrelation function tells, how much the evolving wavepacket still overlaps with the stationary state e.g. the initial state at time zero. In this work, the IR absorption coefficient is evaluated by the Fourier transform of the dipole-dipole correlation function neglecting constant prefactors [108].

$$\alpha(\omega) = \omega \sum_{a=x,y,z} \int_0^\infty \mathrm{d}t\, e^{i\omega - \gamma t}\, C_{\mu_a - \mu_a}(t)\,, \tag{2.72}$$

where γ is a parameter introduced to cut-off the integrand, $\boldsymbol{\mu}_a = (\mu_x, \mu_y, \mu_z)$ and $C_{\mu_a - \mu_a}(t)$ is the dipole-dipole autocorrelation function which is given as,

$$C_{\mu_a - \mu_a} = \langle\Psi(0)|\boldsymbol{\mu}_a(t)\boldsymbol{\mu}_a|\Psi(0)\rangle. \tag{2.73}$$

here $\Psi(0)$ is the ground state.

2.6   Laser Control of Quantum Dynamics

The operator for the interaction Hamiltonian H_{field} of the molecule with the external laser field in Eq. 2.53 is given by the semi-classical dipole approximation [165]. The magnetic dipole as well as the qudrapole are neglected in case of laboratory fixed coordinates because their values are two orders of magnitude smaller than the electric dipole moment. The time-dependent electromagnetic field $\mathbf{E}(t)$ is used to control intramolecular motion and in general is given by:

$$\mathbf{E}(\mathbf{r}, t) = \boldsymbol{\epsilon}\, E_0\, s(t)\, \frac{e^{i(\mathbf{k}\mathbf{r} - \omega t)} + e^{-i(\mathbf{k}\mathbf{r} - \omega t)}}{2}, \tag{2.74}$$

where E_0 is the amplitude of the field with the carrier frequency ω, $\boldsymbol{\epsilon}$ is the polarization vector, $\mathbf{k}$ is the wave vector and $s(t)$ is the shape function which describes the envelope

of the laser pulse. The term $e^{i\mathbf{kr}}$ can be expanded in the Taylor series as follows:

$$e^{i\mathbf{kr}} \approx 1 + i\mathbf{kr} + \cdots . \tag{2.75}$$

The Taylor series can be truncated after the first term since the length of the studied molecules in this thesis are much more shorter than the wavelength of used laser (IR-domain). Therefore, an expression for a position-independent field is used:

$$\mathbf{E}(t) = \boldsymbol{\epsilon}\, E_0\, s(t)\, (\omega t). \tag{2.76}$$

The $s(t)$ shape functions used throughout this thesis are sin^2 or Gaussian function which are given by:

$$s(t) = \exp\left(-(t - t_0)^2/2\tau^2\right) \tag{2.77}$$

$$s(t) = \sin^2\left(\frac{\pi t}{t_p}\right), \qquad\qquad 0 \leq t \leq t_p, \tag{2.78}$$

where t_0 is the center of the Gaussian, τ is related to the width of the Gaussian and t_p is pulse duration with respect to the $\sin^2$ function.

2.6.1   Linearly Polarized Laser Pulses

Analytical laser pulses are well defined laser fields with analytical shape functions. An example for analytical laser pulse control is the pump-dump scheme [56]. In this scheme the pump pulse is used to excite the population from one energetically low lying state (initial state) to a higher state (intermediate or transition state). Next comes the dump pulse which stimulates population back to an energetically lower state (final state). Analytical laser pulses are usually of the form of Eq. 2.77 and Eq. 2.78. A sequence of laser pulses with different envelope shape functions can be expressed as:

$$\mathbf{E}(t) = \sum_i E_{0,i} \cdot \cos(\omega_i t) \exp(-(t - t_{0,i})^2/2\tau^2), \tag{2.79}$$

$$\mathbf{E}(t) = \sum_i E_{0,i} \cdot \cos(\omega_i t) \sin^2\left(\frac{\pi t}{t_{p,i}}\right), \qquad 0 \leq t \leq t_p, \tag{2.80}$$

Where $E_{0,i}$ are the amplitudes of laser fields, ω_i are the carrier frequencies, $t_{0,i}$ are the center of the Gaussian laser pulses, and $t_{p,i}$ are the pulse durations. When $i = 1, 2$ in the previous equations Eq. 2.79 and Eq. 2.80, it is the same like pump-dump scheme where the first pulse excites the ground state to the transition state and then after some delay time comes the dump pulse which deexcites the transition state to the final state.

For the initial guess of the laser pulse, one should take into account that choosing the appropriate (low intensity) value which should be lower than Keldysh limit $(< 10^{13}\, W/cm^2)$ in order to avoid the undesired ionization of the molecular system under consideration. And, for the transition frequency ω_i one should use the resonance frequency between the involved states. But, the optimal laser carrier frequency is usually slightly changed from the resonance frequency. This is because of the interaction of the electric field with system yields slight shifts of the vibrational energy levels (Stark effect). Therefore, the optimum carrier frequency is obtained by starting with the resonating transition frequency ω_i and slightly shifting (detuning) it until optimal results are achieved. In principle one could have other parameters as well.

2.6.2 Circularly Polarized Laser

The state of polarization of a given plane wave is known to be circular if at a given point in space, the tip of the electric field vector describes a circle during time propagation. Such a wave can be expressed as a superposition of two orthogonal and linearly polarized waves (for instance, along the x and y directions) with equal amplitudes but having a phase difference of $\pi/2$, as given below:

$$\mathbf{E}_x(t) = E_0 s(t)(\mathbf{e}_x \cos(\omega t + \varphi)), \tag{2.81}$$

$$\mathbf{E}_y(t) = E_0 s(t)(\mathbf{e}_y \sin(\omega t + \varphi)), \tag{2.82}$$

$$\mathbf{E}_\pm(t) = \frac{E_0}{\sqrt{2}} s(t)(\mathbf{e}_x \cos(\omega t + \varphi) \pm \mathbf{e}_y \sin(\omega t + \varphi)) \tag{2.83}$$

Here, E_0 is field amplitude, $s(t)$ is the envelope function defined in the previous section, Sec. 2.6, ω is the carrier frequency, φ is the phase shift and $\mathbf{e}_x$, $\mathbf{e}_y$ are the unit vectors in x- and y-axes respectively. The laser field that is defined as in Eq. 2.83 is called circularly polarized light (CPL) [166]. The $(+)$ in Eq. 2.83 means the laser is right circularly polarized if the electric field vector rotates in xy plane clockwise. On the other hand the $(-)$ in Eq. 2.83 means the laser is left circularly polarized if the electric field vector rotates in xy plane counterclockwise. The rotation is taken clockwise and counterclockwise with respect to an observer who is looking into the source, i.e., against the direction of propagation which should be z-axis.

CPL can be used for excitation of degenerate electronic as well as degenerate vibrational states. CPL has been used by Barth et. al. [167] for producing a unidirectional electronic ring current for Mg-porphyrin and [168] for spinning a pseudorotating molecular top of three-atomic molecule (CdH_2). In this work, CPL is used to excite degenerate CO vibrational modes for larger molecular system e.g. $Mn_2(CO)_{10}$ in order to have a wavepacket circulation around the principal axis of the molecule.

2.6.3 Optimal Control Theory

Instead of optimizing the laser field required to achieve the control by hand (manually), the optimization process can be obtained by optimal control theory (OCT) [169, 170, 60]. Note that experimentally the so-called feedback control is most successful [171]. What is needed to do OCT are two states; the initial state $|\Psi_i(0)\rangle = |\Psi_i\rangle$ at time $t = 0$ and the final (target) state $|\Psi_f(T)\rangle = |\Psi_f\rangle$ at time $t = T$. Within OCT, one usually defines a control functional J that measures the optimality of the electric field used to transfer the initial state to the target state. The control functional J can be defined as [172, 173]:

$$J(\mathbf{E}, T) = \langle \Psi(T)|O|\Psi(T)\rangle - \kappa \int_0^T dt \frac{E^2(t)}{\sin^2(\pi t/T)} \tag{2.84}$$

where O is the target operator whose expectation value is to be maximized at the final time T. The O could be, for instance, a projection operator $O = |\Phi\rangle\langle\Phi|$ onto the target state $|\Phi\rangle$. The second term penalizes strong fields to ensure that the field does not cause ionization the molecular system, where κ is the so-called penalty factor. The envelope function $\sin^2(\pi t/T)$ serves as a shape function which keeps a smooth pulse envelope [173]. The optimal control laser field is obtained by finding the extremum of the functional given in Eq. 2.84, $\delta J(\mathbf{E}, T)/\delta \mathbf{E}(t) = 0$. This variation gives the optimal control field that can be expressed as:

$$\mathbf{E}(t) = -\frac{\sin^2(\pi t/T)}{\kappa_0} \operatorname{Im}\langle \Theta(t)|\boldsymbol{\mu}|\Psi(t)\rangle, \tag{2.85}$$

where $|\Theta(t)\rangle$ is an auxiliary function which evolves or propagates according to the TDSE Eq. 2.52 and $\boldsymbol{\mu}$ is the dipole moment operator. The Eq. 2.85 can be solved iteratively [172, 173]. For clarity, a subscript is used to describe the iteration number on the wave functions as well as the control field. In the zeroth step, one starts with the initial guess field E_0 and propagates the wave function $|\Psi_0(t)\rangle; t \equiv t_0 \to T_f$ forward by solving TDSE Eq. 2.52 to get at the final time T the wave function $|\Psi(T)\rangle$. Then the target operator O is applied on this wave function to get a new function which is $|\Theta(T)\rangle$. Afterwards, one propagates this new wave function $|\Theta_0(T)\rangle; t \equiv T_f \to t_0$ backward by solving TDSE Eq. 2.52 where the initial time is T_f since the time runs in the revers order to get a new field E_1 which will be used in the first step. In the first step, the calculated field E_1 now can be used to propagate the wave function $|\Psi_1\rangle(t); t \equiv t_0 \to t_f$ forward by solving TDSE Eq. 2.52 to get at the final time T the wave function $|\Psi_1(T)\rangle$. Then one applies the target operator O on this wave function to get a new function which is $|\Theta_1(T)\rangle$. Subsequently the next backward propagation is used to calculate a new field E_2 which should be better than E_1 and so forth till the convergence.

The initial guess for the laser field E_0 is defined and it is supposed to give a good starting point for the iterative process in a way that the laser pulse transfers at least a small part of the initial wave function to the position of the target wave function. In other words, the overlap at the final time between Φ and $\Psi(T)$ should not be equal to zero $\langle\Phi|\Psi(T)\rangle \neq 0$, otherwise the control field will keep zero throughout the iterative process.

As shown from above the procedure, the control field depends only on two functions, definitely the initial wave function $\Psi(t_0)$ and the final wave function Φ propagated forward and backward in time respectively. And, the calculation of these wave functions depends on the control field. OCT has been implemented in the frame of MCTDH package [160]. But, direct implementation of the iterative scheme to verify the field optimization is not possible. So, the field has been evaluated in an external program that communicates with the main program through so-called pipes. This involves an extrapolation scheme to be applied for the field. For more details see Ref [174].

The advantage of the OCT is that, all what is needed are the initial and target states, but no assumption on the reaction mechanism. The disadvantage of the OCT is that, if it is applied to large systems of many degrees of freedom it becomes extremely time demanding.

The optimal fields from OCT are usually rather complicated. Insight into the temporal and frequency structure is provided by the XFROG trace [175]. The XFROG trace is given as,

$$I_{\text{XFROG}}(\omega, t) = \left| \int d\tau E(\tau) G(\tau - t) e^{-i\omega\tau} \right|^2 \tag{2.86}$$

where $G(\tau - t)$ is a step-like gate function with Gaussian tails [176] that selects a small part of the laser pulse around time t which is then Fourier-transformed. The $G(t)$ is given as,

$$G(t) = \begin{cases} 1 & \text{for } |t| \leq W/2 \\ \exp\left(-\frac{(|t| - \frac{W}{2})^2}{2\sigma^2}\right) & \text{for } |t| > W/2 \end{cases} \tag{2.87}$$

here W is the width of the rectangular part, σ is the width of the Gaussian shoulders.

CHAPTER 3

IR Laser Control for DPT in Porphycenes

3.1 Overview

In this chapter the results concerning triggering double proton transfer as well as its mechanisms will be discussed and investigated. Before doing that, the model used for double proton transfer is introduced and the corresponding Hamiltonian is constructed. Afterwards, the effect of the time duration, and the Hamiltonian parameters such as barrier height and symmetry on the the DPT mechanisms and the laser pulse shape is investigated. Finally, the specific example of an asymmetric porphycene derivative is discussed.

3.2 Double Proton Transfer Model

The basic model for double proton transfer is a hydrogen bonded molecule or a complex in which the two hydrogen atoms are in equivalent positions. These two hydrogen atoms can transfer between these equivalent positions. Each hydrogen atom is positioned inside a hydrogen bonding frame like M-H···M, where M is a molecule or a complex that includes a heavy atom for instance, O, N, S and C that can carry the mobile hydrogen. The two M-H···M are arranged in such a way that the four M atoms occupy the four corners of a rectangle with sides a and b as introduced in Fig. 3.1. For M=N parameter a is the heavy atoms distance containing the hydrogen bonding while parameter b is the distance between the two hydrogen bonds. If b is so large that there is no interaction between the two hydrogen bonds, the simplest form of the double proton transfer potential is given by a sum of two double minimum potentials, i.e. sum of a two quartic potentials.

$$U_{\mathrm{sym}}(x_1, x_2) = \frac{U_0}{x_0^4} \left[(x_1^2 - x_0^2)^2 + (x_2^2 - x_0^2)^2 \right] . \qquad (3.1)$$

The DPT Hamiltonian will first be given in terms of single proton transfer coordinates x_1 and x_2 which are assumed to describe the linear translocation of the particles between donor and acceptor sites. If the coupling between the two hydrogen bonds cannot be
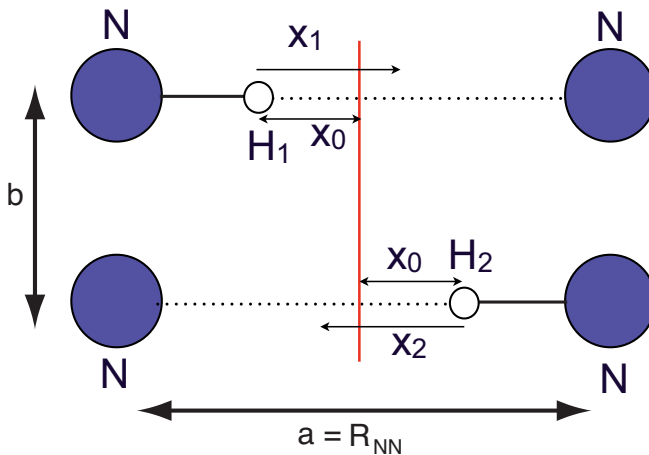
Fig. 3.1 *Schematic representation of the basic model of double proton transfer along parallel equivalent hydrogen bonds in hydrogen bonding systems.*

neglected, the simplest form including the coupling term is obtained by coupling these two quartic potentials via a bilinear interaction

$$U_{\text{sym}}(x_1, x_2) = \frac{U_0}{x_0^4} \left[(x_1^2 - x_0^2)^2 + (x_2^2 - x_0^2)^2 \right] - \frac{gU_0}{x_0^2} x_1 x_2 \,. \tag{3.2}$$

This type of potential has been used extensively by Smedarchina and coworkers [36, 39]. It has two equivalent global minima (called "trans" in the following) and two equivalent local minimum (called "cis") which correspond to the transfer of a single proton. In eq. (3.1), U_0 is the barrier for uncorrelated single proton transfer, x_0 is half the transfer distance and is defined for symmetric DPT system as $2x_0 = a - 2r \cos\theta$, where a is N-N distance, r is the $N - H$ bond length and θ is the $\angle$ H-N-N which express the non-linearity of the hydrogen bond. In Eq. 3.2, g is the dimensionless bilinear coupling strength. Since we are aiming at an analysis in terms of concerted and stepwise transfer, this potential is more conveniently expressed in terms of the symmetric and asymmetric transfer coordinates $x_s = (x_1 + x_2)/2$ and $x_a = (x_1 - x_2)/2$, respectively. This transformation gives for eq. (3.2)

$$\begin{aligned} U_{\text{sym}}(x_s, x_a) &= 2U_0 + \frac{U_0}{x_0^2} \left[(g - 4)x_a^2 - (g + 4)x_s^2 \right] \\ &+ \frac{2U_0}{x_0^4} (x_s^4 + x_a^4 + 6x_s^2 x_a^2) \,. \end{aligned} \tag{3.3}$$

For the purpose of laser control of DPT it is useful to consider the case of asymmetric molecules in order to allow for a clear identification of initial and final states. Two types of asymmetry can be introduced into the model Hamiltonian, that is, with respect to the trans and cis states:

$$U_{\text{asym}}(x_s, x_a) = \frac{\alpha_{\text{trans}} U_0}{x_0} x_s + \frac{\alpha_{\text{cis}} U_0}{x_0} x_a \,, \tag{3.4}$$

where α_{trans} and α_{cis} are dimensionless parameters characterizing the detuning between the trans and cis states, respectively.
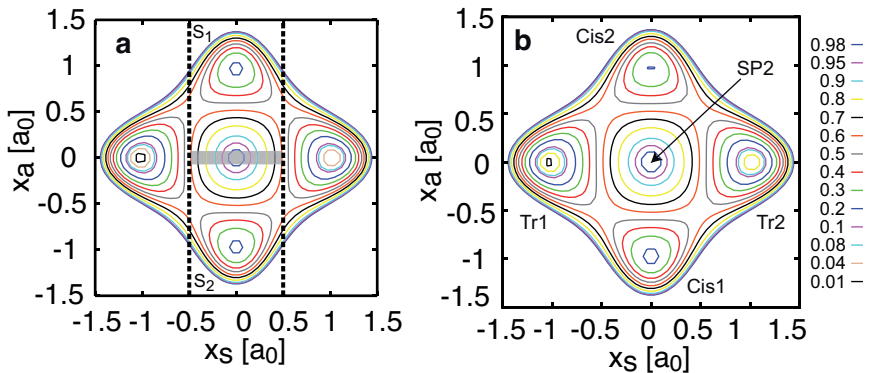
Fig. 3.2 *Panel (a): two-dimensional PES for the high barrier case ($U_0 = 2000\ cm^{-1}$, $x_0 = 1a_0$, $g = 0.2$, $\alpha_{\mathrm{trans}} = 0.005$, and $\alpha_{\mathrm{cis}} = 0.0$). The energy is given in units of the barrier height for concerted transfer ($4428\ cm^{-1}$). The energetic difference between the two trans minima is 41 cm^{-1}. The two dashed lines mark the region which is passed during stepwise DPT. This doesn't include the shaded area whose width in x_a direction corresponds to the width of the vibrational ground state and which is assigned to concerted DPT. Upper and lower stepwise DPT is marked by S_1 and S_2, respectively. In the low barrier case (not shown) $U_0 = 800\ cm^{-1}$, giving a barrier height of $1773\ cm^{-1}$. The barriers for stepwise DPT are $2430\ cm^{-1}$ and $975\ cm^{-1}$ and the energies of the cis minima are $821\ cm^{-1}$ and $330\ cm^{-1}$ for the high and low barrier case, respectively. Panel (b): two-dimensional PES for the low barrier asymmetric cis case ($U_0 = 800$ cm^{-1}, $x_0 = 1a_0$, $g = 0.2$, $\alpha_{\mathrm{trans}} = 0.005$, and $\alpha_{\mathrm{cis}} = 0.01$). The energy is given in units of the barrier height for concerted transfer ($1773\ cm^{-1}$). The energetic difference between the two cis minima is $31\ cm^{-1}$.*

The total Hamiltonian is given by

$$H = -\frac{\hbar^2}{2m}\left(\frac{\partial^2}{\partial x_s^2} + \frac{\partial^2}{\partial x_a^2}\right) + U_{\mathrm{sym}}(x_s, x_a) + U_{\mathrm{asym}}(x_s, x_a)\,. \tag{3.5}$$

Since it is assumed that the moving particles are H-atoms, the mass for the collective coordinates is $m = 2m_{\mathrm{H}}$.

For the interaction with the laser field we assume that the permanent dipole moment depends only linearly on the coordinates, i.e.,

$$H_{\mathrm{field}}(t) = -(\mu_a x_a + \mu_s x_s)\mathbf{E}(t) \tag{3.6}$$

where $\mu_{a/s}$ is the derivative of the dipole moment with respect to $x_{a/s}$ and $\mathbf{E}(t)$ is the laser field. For the case of symmetric systems like porphycene the dipole moment changes only along the asymmetric coordinate (for simplicity we have chosen $\mu_a = 1.0$ e) in the simulation below. This will be used as the reference case. In order to investigate the principal effect of a dipole gradient along x_s due to asymmetric substitution on the substrate molecule we will also consider a variation along x_s. The parameters of the Hamiltonian have been chosen such as to highlight in particular cases of high "porphyrin" and low "porphycene" barriers "4126" cm^{-1} [177] and "2256" cm^{-1} [45] for the concerted DPT, respectively. The stationary Schrödiner equation $H|\phi_i\rangle = E_i|\phi_i\rangle$ has been solved to obtain the eigen states of the system.
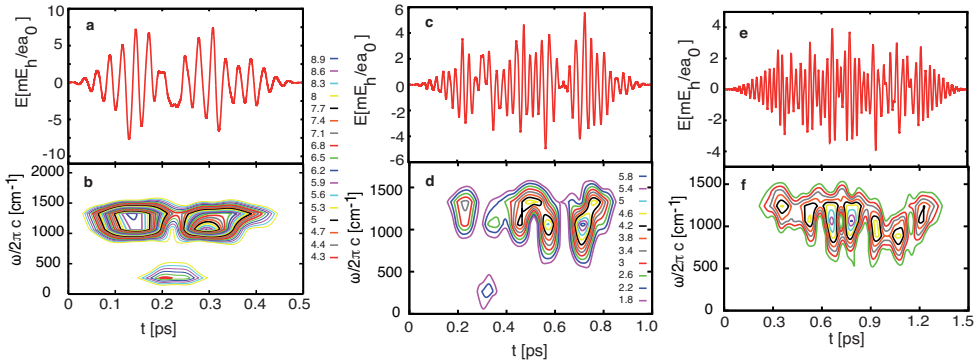
Fig. 3.3 *Laser pulses obtained from OCT for high barrier symmetric cis case using $T = 500$ fs, (a) (guess field $E_0 = 7$ mE_h/ea_0) after 291 iterations, $T = 1.0$ ps (c) (guess field $E_0 = 0.95$ mE_h/ea_0) after 244 iterations and $T = 1.5$ ps (e) (guess field $E_0 = 2$ mE_h/ea_0) after 165 iterations ($\kappa = 1.5$ a.u., $\omega = 1194$ cm^{-1}). Panels b, d and f show the respective XFROG traces for the three time durations and for a gate function of width 1000 a.u. and Gaussian tails of width 1000 a.u. (contours in units of a.u.).*
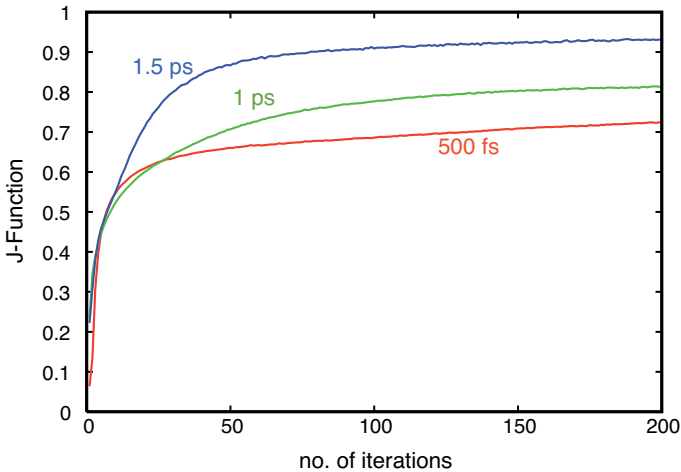

Fig. 3.4 *Control function Eq.2.84 as a function of the number of iterations for high barrier symmetric cis case for the three time durations.*

3.3 Quantum Dynamics

The two-dimensional time-dependent Schrödinger equation

$$i\hbar\frac{\partial}{\partial t}\Psi(x_a, x_s; t) = (H + H_{\text{field}}(t))\Psi(x_a, x_s; t) \tag{3.7}$$

has been solved using the MCTDH approach as implemented in the Heidelberg program package [178]. To this end the two-dimensional wave function $\Psi(x_a, x_s; t)$ is represented on a grid in terms of a harmonic oscillator discrete variable representation (64 points within [-2.5:2.5] a_0). The actual propagation is performed using the variable mean field scheme in combination with a 6-th order Adams-Bashforth-Moulton integrator. Twenty single particle functions per coordinate have been used. Using this setup the largest natural orbital populations have been typically on the order of 10^{-6}. Selected eigenstates of the time-independent Hamiltonian, ϕ_i, are obtained by improved relaxation method [164].

The shape of the laser field is determined using optimal control theory (OCT), that is, the functional in Eq. 2.84 is maximized at some final time T [172, 173]. The iterative optimization of the field has been performed by using the implementation within the MCTDH program package by Brown and coworkers as detailed in Ref. [176]. The pulses will be characterized in terms of their XFROG trace Eq. 2.86

It will be assumed that initially the system is in the vibrational ground state which is localized in the left part of the potential due to the asymmetry term α_{trans}. The target operator will be taken as the projector onto that state which is localized in the right well of the potential, i.e. $\hat{O} = |\phi_1\rangle\langle\phi_1|$ (see Fig. 3.6). In order to elucidate the mechanism of DPT, i.e. stepwise vs. concerted, we have defined step-like operators dividing the different regions of transfer between the two trans-forms as shown in Fig. 3.2. Here, transfer is counted as concerted if the wave packet passes a narrow range in the vicinity of the second order saddle point of the PES. The width of that range is, of course, arbitrary and we have used the width of the ground state distribution. Furthermore, note that this definition of "stepwise" does not imply the existence of a stable intermediate in the sense of traditional kinetic considerations.

The results reported below have been obtained for different numbers of OCT iterations starting with a $\sin^2$-shaped guess field. The convergence of the control functional has been monotonic as shown in Fig. 3.4 . The iteration number has been chosen such that the change in the control yield between two iterations was below 10^{-4}. The guess field frequency that has been chosen for the high barrier case is slightly red-shifted as compared with the strong IR active first excited state along the x_a coordinate. For the low barrier case the resonance to the x_a coordinate has been chosen. The spectrum for the high and the low barrier cases is obtained via Fourier transforming the autocorrelation function of the dipole moment [108] which is assumed to be linearly x_a coordinate dependent. The spectrum is presented in Fig. 3.5. Lowering the guess frequency, e.g. by $20\,\text{cm}^{-1}$, resulted in zero yield, an increase by the same amount gave a similar convergence behavior of the control yield.

3.4 High Barrier Case

The reference case will be the high barrier scenario with equivalent cis minima shown in Fig. 3.2 in the right panel (for parameters see figure caption). Note that with these cases, we do not address any specific system, although the energetics of the PES can be considered to be typical for DPT molecules. Here, in particular porphyrin and por-
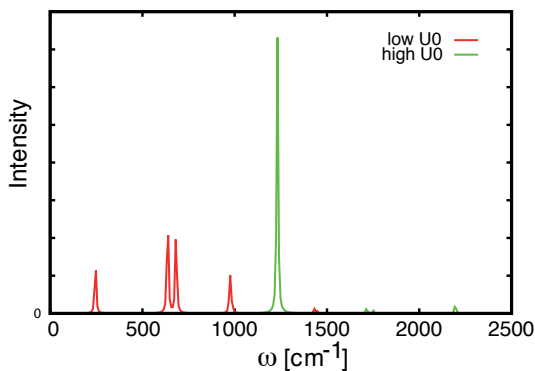
Fig. 3.5 *Linear infrared absorption spectra of 2D DPT model system for both case high and low barrier cases. The spectrum has been obtained from a 3000 fs dipole moment autocorrelation function employing a numerical damping time of 1500 fs for the Fourier transform.*
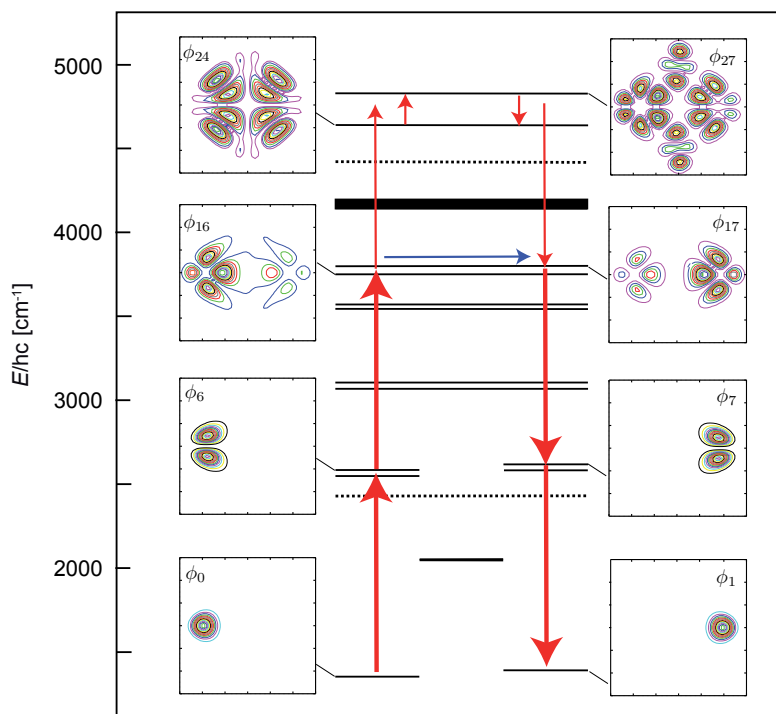

Fig. 3.6 *Level scheme for the high barrier case and probability densities of selected eigenstates which get appreciably populated during the laser driven transfer. The lengths of the horizontal solid bars indicate the range of delocalization of the state with respect to the symmetric coordinate x_s (e.g. ϕ_0/ϕ_1 are localized in the left/right trans minimum, ϕ_2/ϕ_3 ($\sim$2000 cm^{-1}) around $x_s = 0$, i.e. in the cis minimum, etc.). The dashed lines correspond to the energy of the barriers for concerted and stepwise transfer. The density plots cover the range $[-1.5 : 1.5]a_0$ along the vertical x_a and the horizontal x_s axes. The vertical arrows indicate the major pathway for laser driven transfer, the horizontal one shows the pathway for concerted transfer. (Note that around 4200 cm^{-1} there are several close lying states.)*

phycene derivatives offer a tunability of the energetics over a wide range (see, e.g., [20]), a specific application will be discussed in section 3.6.

3.4.1 Pulse Duration

The OCT optimization problem depends on the final time T at which the optimization goal shall be reached. The obvious question is to what extent will the OCT field and the associated wave packet dynamics depend on the pulse duration. Fig. 3.3 compares OCT pulses for $T = 500$ fs panel (a), $T = 1000$, fs panel (c) and $T = 1500$ fs panel (e). Inspecting the XFROG traces, we notice that upon increasing T one obtains a pulse train like structure with an increasing number of overlapping subpulses.

The dynamics can be analyzed in terms of populations of eigenstates of the field-free Hamiltonian. A level scheme as well as densities for selected states are given in Fig. 3.6. In total there are 24 states below the barrier for concerted DPT. Also shown are the localized initial, ϕ_0, and target, ϕ_1, states which differ by 38 cm^{-1} for the chosen α_{trans}. The population dynamics for $T = 500$ fs , 1000 fs and 1500 fs is presented in Fig. 3.7. Upper panels show the initial state, target state and some selected states which are populated during the propagation time. Panels (b), (d) and (f) show the population of the two states, ϕ_{24} and ϕ_{27} for the three time durations, respectively.

The population dynamics for $T = 500$ fs shows that the initial state is almost completely depopulated during the first $\sim$180 fs whereas the target state becomes populated after $\sim$300 fs reaching a final population of 0.74. Since the dipole moment changes along the x_a direction only, we would expect that the laser pulse excites a wave packet along this direction. Indeed the initial excitation is to state ϕ_6 which has a node along x_a. But already the next state which is populated, i.e. ϕ_{16}, is of mixed character containing excitations along both directions. This mixing is, of course, a consequence of the anharmonicity of the potential. Both states are excited by the first pulse within about 200 fs. The mismatch between the $\phi_0 \rightarrow \phi_6$ and $\phi_6 \rightarrow \phi_{16}$ transitions amounts to a 65 cm^{-1} redshift which is covered by the pulse spectrum. The latter also shows a slight down-chirp. Due to the delocalized nature of states ϕ_{16} and ϕ_{17} the first pulse actually excites a superposition of these two states, what can be seen from the rise of the population of state ϕ_{17} around 100 fs in Fig. 3.7 (a). The second pulse which is centered around 300 fs acts as a dump pulse transferring the populations according to the scheme $\phi_{17} \rightarrow \phi_7 \rightarrow \phi_1$. In between the two main pulses there is a minor feature at $\sim$220 fs spectrally located around 200 cm^{-1}. It is related to the population of states which are energetically above the barrier for concerted transfer (see, Fig. 3.6). In fact the two main pulses excite and de-excite state ϕ_{24} according to $\phi_{16} \rightarrow \phi_{24}$ and $\phi_{24} \rightarrow \phi_{17}$, respectively. The subpulse centered around 200 cm^{-1} switches populations according to $\phi_{24} \rightarrow \phi_{27} \rightarrow \phi_{24}$. This effect is most likely not relevant for the DPT control.

The population dynamics for the $T = 1000$ fs case is shown in Fig. 3.7 (c). Compared with the $T = 500$ fs case, only the effect of the first pulse is similar, that is, the excitation scheme $\phi_0 \rightarrow \phi_6 \rightarrow \phi_{16}/\phi_{17}$ applies. Some features of the dynamics triggered by the other subpulses are: (i) the population of the initial state becomes constant from 350 fs on and starts to depopulate again at 430 fs and it almost reaches zero population around 800 fs. (ii) The target state starts to be populated around 420 fs, becomes slightly depopulated around 600 fs, keeps constant population and shows an enhanced population around 700 fs via the depopulation of ϕ_7 and ϕ_{17} states. (iii) There are some oscillation of the wave packet between ϕ_6 and ϕ_{16} between 430-600 fs and these oscillations are due to the high frequencies pulses. (iv) The subpulse centered around 320 cm^{-1} populates states above the concerted barrier and switches populations according to $\phi_{24} \rightarrow \phi_{27} \rightarrow \phi_{24}$ but, the contributions of these states become less than in the case of $T = 500$ fs. At the very end,
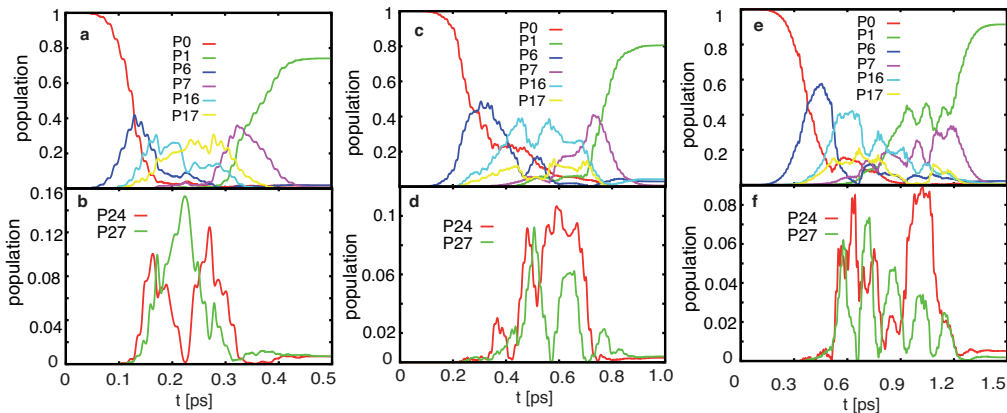
Fig. 3.7 *In panels (a), (c) and (e) are the population dynamics for some states (ϕ_0, ϕ_6, ϕ_7, ϕ_{16}, ϕ_{17}, ϕ_1) of higher contributions for $T = 500$ fs , $T = 1000$ fs and $T = 1500$ fs respectively for the laser fields in Fig. 3.3. In panels (b), (d) and (f) are the populations dynamics for ϕ_{24} and ϕ_{27} for the three time durations.*
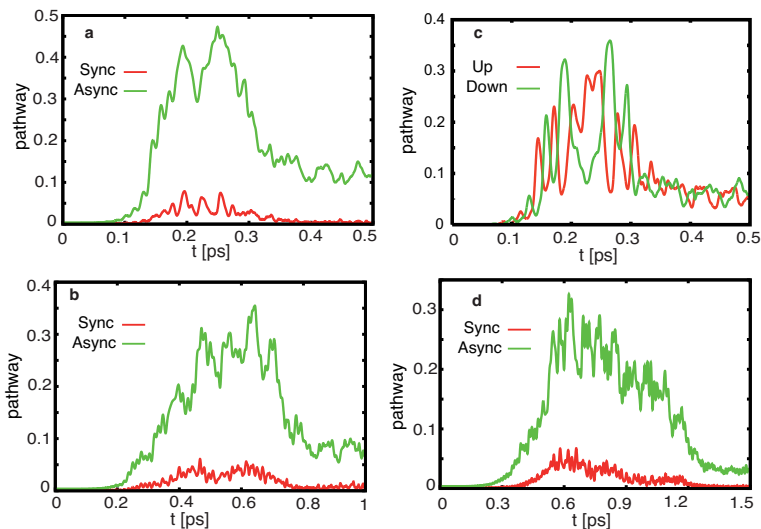

Fig. 3.8 *Concerted and step-wise pathway contributions for $T = 500$ fs (a) panel, $T = 1000$ fs (b) panel and $T = 1500$ fs (d) panel which measured by the probability of being in the C and S regions of the PES. The (c) panel is the measured population for two cis region with $\alpha_{\mathrm{cis}} = 0.00$.*

the population of the target state at 1000 fs is 0.82, thus exceeding the one for the 500 fs case.

The population dynamics for the $T = 1500$ fs case is shown in Fig. 3.7 (e) and (f). As compared with the $T = 500$ fs case it is more complex. Only the effect of the first pulse is comparable, that is, the excitation scheme $\phi_0 \rightarrow \phi_6 \rightarrow \phi_{16}/\phi_{17}$ applies. Some features of the dynamics triggered by the other subpulses are: (i) The initial state is repopulated around 600 fs and subsequently depopulated until about 900 fs. (ii) A population/depopulation is also observed for the target state around 1000 fs. (iii) Above barrier states are populated directly by transitions from below barrier states. Comparing the contributions of those states with these of the previous two propagation times shows that it becomes smaller upon increasing the pulse duration. So it can be concluded that the low frequency contributions can be avoided when using longer pulses. Finally, the population of the target state at 1500 fs is 0.92, thus exceeding the one for the 500 fs case.

Since the reference case contains a dipole moment in x_a direction only, one expects that the laser driven wave packet is bound to move toward the product well in a stepwise fashion, i.e. passing through the regions S_1 and S_2 in Fig. 3.2 (a). Indeed this is the major pathway as shown for different pulse durations in Fig. 3.8 (a), (b) and (d). We further notice that the rise of the target state population is closely related to the decay of the probability of being in the regions S_1 and S_2. For example, for $T = 1500$ fs Fig. 3.8 (d) the latter has decayed by ~ 1200 fs which coincides with a steep rise of P_1. In other words, it takes about 1200 fs for the major part of the laser-driven wave packet to reach the product well via a stepwise mechanism. Similar arguments hold for the $T = 1000$ fs and $T = 500$ fs cases where this transition takes place around 800 fs and 300 fs respectively.

Comparing the results for the three propagation lengths one notices a difference as far as the dynamics in the range of concerted DPT is concerned. Inspecting the densities of the different populated states it is clear that the contribution to the concerted pathway is mostly due to the pair ϕ_{16} and ϕ_{17} which both have x_a and x_s character. A superposition of these states is excited already by the first pulse and the subsequent dynamics will be that of a two-level system. The energy mismatch between these two states of 51 cm^{-1} yields a time scale of $\sim$650 fs for a round trip between the two minima, i.e. the transfer from the reactant to the product well takes about 325 fs. Given the approximate nature of this estimate, e.g. due to preparation process, one finds this time scale for the motion through the concerted region in the $T = 500$ fs case. But, for the $T = 1000$ fs case the time that the wave packet spends in the C region is about 600 fs, Fig. 3.8 (b). While for the $T = 1500$ fs case the time that the wave packet spends in the C region is about 900 fs as shown in Fig. 3.8 (d). From Fig. 3.8 one notices that there are one, two and three maxima of the C region population for $T = 500$ fs, $T = 1000$ fs and $T = 1500$ fs, respectively and these coincide with maxima of the populations of especially ϕ_{16} state in three time durations as introduced in Fig. 3.7 (a), (c) and (e) panels. Since ϕ_{16} and ϕ_{17} are energetically below the barrier, one can conclude that the contribution to concerted DPT is mostly due to tunneling. Also one concludes that upon increasing propagation time, the contribution of the x_s character states ϕ_{16} and ϕ_{17} increases, and so the importance of the concerted mechanisms.

3.4.2 Asymmetry Cis Parameter

Actually, realistic DPT systems don't necessarily have the same intermediate state energetics, In other words, the cis intermediates have a different energy, that is why in the following, the effect of adding an asymmetry to the two cis configurations for the
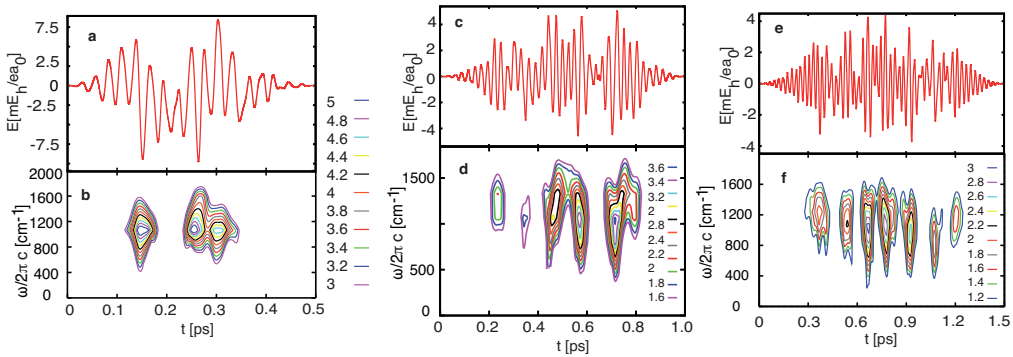
Fig. 3.9 *Panels (a), (c) and (e) are laser pulses obtained from OCT using $T = 500$ fs (guess field $E_0 = 7$ mE_h/ea_0) after 195 iterations, $T = 1.5$ ps, (guess field $E_0 = 0.95$ mE_h/ea_0) after 289 iterations and $T = 1.0$ ps, (guess field $E_0 = 2$ mE_h/ea_0) after 195 iterations, respectively, for higher barrier case with different cis energetics ($\kappa = 1.5$ a.u., $\omega = 1194$ cm^{-1}). Panels (b), (d) and (f) show the respective XFROG traces for the three time durations, respectively, for a gate function of width 1000 a.u. and Gaussian tails of width 1000 a.u. (contours in units of a.u.).*

high barrier reference case will be explored as well as its effects on the study the optimal field, the involved populated states, and the mechanisms of the DPT. We have chosen $\alpha_{cis} = 0.01$ which translates into an energetic difference of 77 cm^{-1} between the two cis minima. The PES is shown in Fig. 3.2 (b), for the parameters see Figure caption.

The OCT laser fields for different time durations are introduced in Fig. 3.9, for $T = 500$ fs, (a) $T = 1000$ fs (c) and $T = 1500$ fs (e). Comparing the XFROG traces for such fields with the symmetric reference case fields, it is seen that, the fields are looking different for all time durations. Specifically, for shorter time durations, for instance $T = 500$ fs, the number of pulses are different, there are three pulses instead of two. And, the low frequency contributions disappeared here in both cases $T = 1000$ fs and $T = 500$ fs and this will be reflected in the population of certain state as described below.
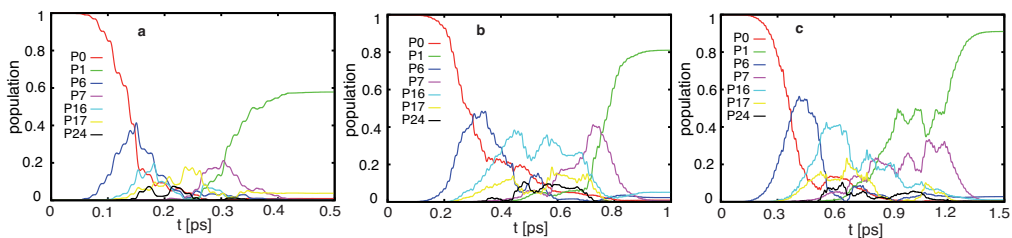

Fig. 3.10 *Population dynamics for some states (ϕ_0, ϕ_1, ϕ_6, ϕ_7, ϕ_{16} and ϕ_{17}) $T = 500$ fs (a), $T = 1000$ fs (b) and $T = 1500$ fs (c). For higher barrier case with different cis energetics.*

The population dynamics for all time durations are shown in Fig. 3.10, for $T = 500$ fs (a), $T = 1000$ fs (b) and $T = 1500$ fs (c). Comparing these populations with the symmetric reference case it is clear that the state ϕ_{27} is not populated any more because of the absence of the low frequency sub-pulse which was responsible for the excitation of the wave packet from ϕ_{24} to it. With respect to $T = 1500$ fs and $T = 1000$ fs, there is no big difference in the shape of the populations between asymmetric cis case and the reference symmetric case. However it is noted that, the final population of the target

state is now 0.91 and 0.81, respectively. For $T = 500$ fs, there are some differences: (i) the initial state is almost depopulated at ~ 267 fs i.e. later than the reference case, (ii) the target state becomes populated after ~ 400 fs reaching the final population of 0.58, (iii) the ϕ_6, ϕ_{16} states get populated and depopulated simultaneously, but in the reference case they are populated step wise, (iv) states ϕ_7 and ϕ_{17} are depopulate step wise but in the symmetric case they are depopulated simultaneously. And, the conclusion for that is, in the case of symmetric cis case, the contributions of the concerted pathway is bigger than the case of asymmetric cis case with different cis energetics since the concerted pathway is mediated through the ϕ_{17} state. This means the wavepacket goes directly from state ϕ_{17} to the target state and this contribution of the concerted pathway is attributed to tunneling.

Fig. 3.11 shows in the (a), (c) and (e) panels, the different pathways, synchronous and asynchronous and in the (b), (d) and (f) panels the populations of the two regions of the two cis minima. In the symmetric reference case, the populations of the different cis regions S_1 and S_2 reflects the oscillation of the excited wave packet in the more stable trans well as seen in Fig. 3.8 (c) for $T = 500$ fs. That means, if the major part of the wave packet moves via S_1 there is a minimum in the population of S_2 and vice versa. Overall there is no net preference for a pathway. Since the S_2 region is energetically more favorable in the asymmetric cis case, OCT prefers this way as seen from Fig. 3.11 panel (b) ($T = 500$ fs) and panel (f) ($T = 1500$ fs).

3.4.3   Non-Vanishing x_s Dipole

Now, we address the case where there is a nonvanishing dipole moment along both directions, exemplarily we have chosen $\mu_a/\mu_s = 4$. Here, direct excitation of the x_s coordinate becomes possible and as a result, the field shape, states involved in the propagations and the pathways could be affected and we are going to show that in the following.

The OCT fields are shown in Fig. 3.12, for $T = 500$ fs (a), $T = 1000$ fs (c) $T = 1500$ fs (e) and their corresponding XFROG are shown in panels (b), (d) and (f), respectively. Comparing these XFROGs with the reference case, it can be seen that, the low frequency contributions disappeared in the cases of $T = 500$ fs and $T = 1000$ fs and as a result, this affects the population of the above barrier state specifically ϕ_{27}. The OCT field for $T = 1500$ fs is looking simpler than in the previous two cases, the symmetric cis reference case and the asymmetric cis case. The populations of the involved states are presented in Fig. 3.13.

For $T = 1500$ fs in (panels (e) and (f)), the ground state has the same behavior, depopulation, population and depopulation again. For this case it starts to populate again around 400 fs, but around 500 fs for the reference symmetric cis case. And, the ground state here is almost completely depopulated around 750 fs, but around 900 fs for the reference symmetric cis case. This means the ground state depopulation here is faster than the symmetric cis reference case since the wavepacket now is excited in both x_a and x_s directions instead of x_a for the reference symmetric cis case. With respect to the the target state, its population in this case has a different behavior compared with the reference symmetric cis case. It shows an earlier start of population before 600 fs, depopulates again to be near zero population before 800 fs and becomes steeply populated starting at 930 fs.

In case of $T = 1000$ fs (panels (c) and (d)), the behavior of the ground state is the same like in the reference symmetric cis case for this time duration. In addition, it is almost completely depopulated earlier than the reference symmetric cis case for the same reason (x_a and x_s excitation). With respect to the target state $T = 1000$ fs, it is a bit different from the symmetric cis reference case. It starts to populate before 400 fs a bit
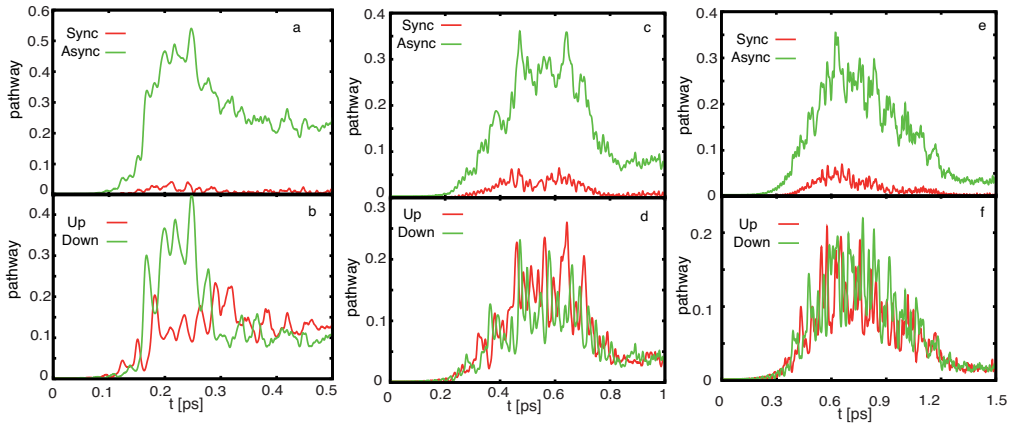
Fig. 3.11 *In panels (a), (d) and (e) are the concerted pathway against step-wise pathway contributions for $T = 500$ fs (f), $T = 1000$ fs (c) and $T = 1500$ fs (e) which measured by the probability of being in the C and S regions of the PES. In panels (b), (d) and (f) are the populations of the two cis regions with $\alpha_{\mathrm{cis}} = 0.01$ for the three time durations. For higher barrier case with different cis energetics.*
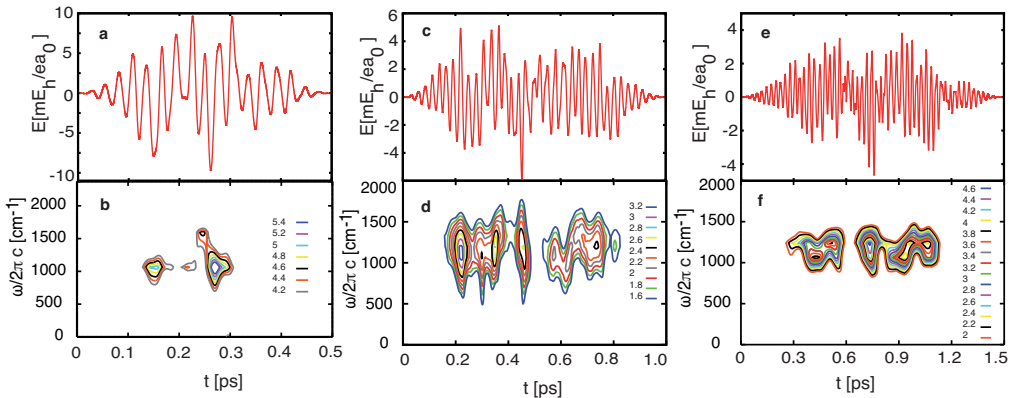

Fig. 3.12 *Laser pulses obtained from OCT for the case of nonvanishing dipole moment along both directions x_a x_s for $T = 500$ fs (a) (guess field $E_0 = 7$ mE_{h}/ea_0) after 385 iterations, $T = 1.0$ ps (c) (guess field $E_0 = 0.95$ mE_{h}/ea_0) after 449 iterations and $T = 1.5$ ps (e) (guess field $E_0 = 2$ mE_{h}/ea_0) after 158 iterations ($\kappa = 1.5$ a.u., $\omega = 1194$ cm^{-1}). Panels (b), (d) and (f) show the respective XFROG traces for all time durations, respectively, for a gate function of width 1000 a.u. and Gaussian tails of width 1000 a.u. (contours in units of a.u.).*
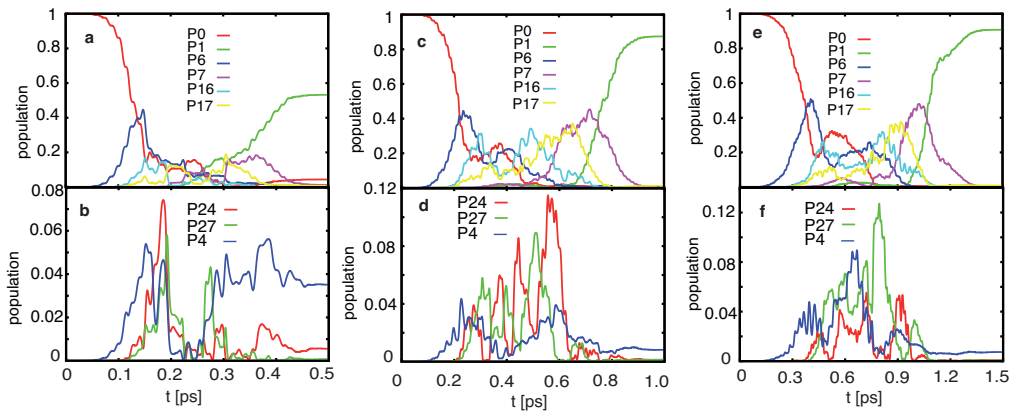
Fig. 3.13 *In panels (a), (c) and (e) are the population dynamics for some states (ϕ_0, ϕ_1, ϕ_6, ϕ_7, ϕ_{16} and ϕ_{17}) of higher contributions for $T = 500$ fs, $T = 1000$ fs and $T = 1500$ fs, respectively. In panels (b), (d) and (f) are the populations dynamics for ϕ_4, ϕ_{24} and ϕ_{27} for the three time durations, respectively. These for the case of nonvanishing dipole moment in both directions x_a and x_s.*
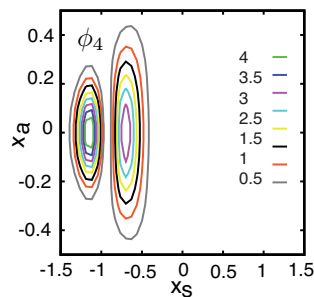
Fig. 3.14 *Probability density of the vibrational eigenstate ϕ_4 which is populated using nonvanishing dipole moment in both directions x_a and x_s.*

Fig. 3.15 *Concerted pathway against step-wise pathway contributions for $T = 500$ fs (a), $T = 1000$ fs (b) and $T = 1500$ fs (c) which measured by th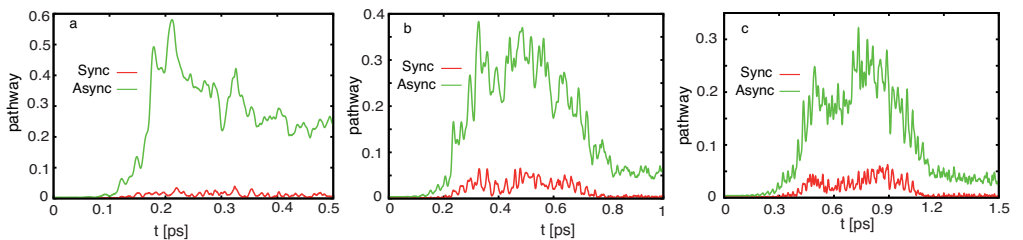e probability of being in the C and S regions of the PES using nonvanishing dipole moment in both directions x_a and x_s with $\alpha_{cis} = 0.00$.*

earlier than the reference case, depopulates again and is steeply populated at 650 fs which is earlier than that of the corresponding time duration for the reference case in which it is steeply populated at 750 fs. This has confirmed that, the target state is reached faster since the ground state wavepacket now is excited in two directions.

For $T = 500$ fs (panels (a) and (b)), the ground state behavior shows steep depopulation, population after 200 fs, depopulation again at about 260 fs and finally it ends up with some population. With respect to the above barrier states ϕ_{24} and ϕ_{27}, a decreasing of the population of theses states occurs with decreasing time propagation length and this has been confirmed by the absence of low frequency sub-pulses as presented in the Fig. 3.12 in (b) panel. Because of the excitation of the wavepacket in both directions x_a and x_s in the same time, ϕ_4, which is shown in Fig. 3.14 to be of x_s character, has been populated as shown in Fig. 3.13 in (b), (d) and (f) for all time durations.

Concerning the excitation of the wave packet in the x_s direction, one would expect the importance of the concerted pathway to increase. Indeed this is the case (see Fig. 3.15) and for the optimized field the integrated populations for both pathways during the time interval up to 1500 fs are obtained to give a ratio of $C_{tot}/S_{tot} = 0.144$. This value exceeds the 0.130 obtained from the corresponding duration time of the reference case. However, the extra gain in concerted DPT is small. In fact the OCT pulse populates a state of x_s excitation character (ϕ_4) which is ~ 36 cm^{-1} below ϕ_6. The population, however, doesn't exceed 10% and is subsequently also promoted to ϕ_{16}. Thus the smallness of the gain in concerted DPT is due to the fact that ϕ_{16}, which plays the dominant role for the concerted DPT, can be reached from the x_a and x_s fundamental excitation of states ϕ_6 and ϕ_4, respectively. That is, there is no substantial net effect due to the (competing) wavepacket excitation of along the symmetric coordinate.

3.5   Low Barrier Case

Now, the effect of lowering the barrier height U_0 on the OCT field, the involved states in DPT, and the pathways of the transfer will be explored. Afterwards, the effect of the α_{cis} parameters for the low barrier case will be discussed. The OCT fields and their XFROG for the three time durations are presented in Fig. 3.16, for $T = 1500$ fs (a), $T = 1000$, fs (c) and $T = 500$ fs (e). A level scheme diagram as well as the involved eigenstates are shown in Fig. 3.17.

Actually lowering the reaction barriers has a substantial influence on the OCT field and the wave packet dynamics. First, we notice that, in contrast to the high barrier case for all time durations, the OCT pulse consists of only three subpulses or two subpulses for $T = 1500$ fs and $T = 1000$ or 500 fs, respectively. These pulses drive the wave packet essentially via the stepwise pathways as seen in Fig. 3.18, lower panels. This is somehow counter-intuitive since one would expect that upon lowering the barrier for concerted DPT, tunneling becomes even more effective. However, for the present parameters there is essentially only one state below the barrier having locally an excited x_a character, namely ϕ_5; see Fig. 3.17. This state is not appreciably mixed with other states, say of x_s excitation character. Instead it is delocalized encompassing both trans as well as the cis regions.

The population dynamics in Fig. 3.18 (a), (c) and (e) for $T = 500$ fs, $T = 1000$ fs, and $T = 1500$ fs, respectively, shows that the dominant pathway is indeed $\phi_0 \to \phi_5 \to \phi_1$ triggered in a pump-dump like fashion. The spectrally broad pulses also excite state ϕ_7 which in turn causes an excitation of an above barrier state, ϕ_{12}. The latter state clearly will lead to a contribution of the concerted pathway, but this time not by virtue of tunneling since it is above the SP2 barrier. However, its effect is rather minor as can be traced from the population of the concerted region in Fig. 3.18. For $T = 1500$ fs,

the ground state is almost depopulated at about 1100 fs and the target state is almost populated at about 1350 fs. The ground state for the $T = 1000$ fs propagation time does not completely depopulate. The target state shows a steep population rise till 600 fs, a plateau till about 750 fs and again a population to 0.90 at the end. Within the $T = 500$ fs duration time ground state and target state are having the same behavior like for $T = 1500$ fs except that the ground state at the end still has some population and the target state reaches 0.82 only.
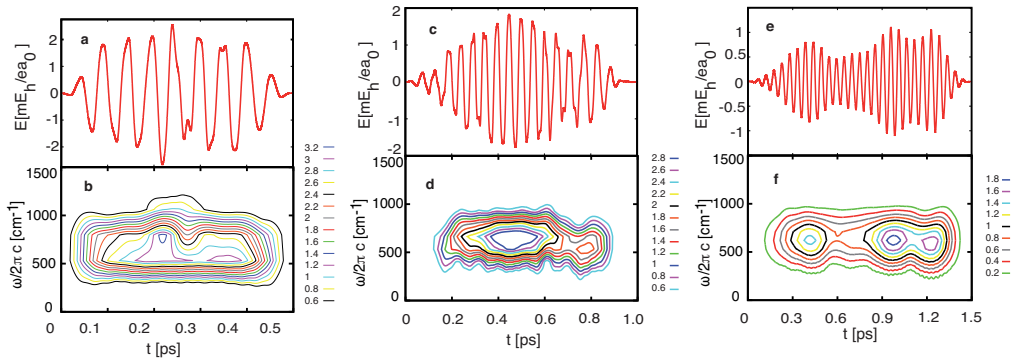

Fig. 3.16 *Laser pulses obtained from OCT for symmetric cis lower barrier case for $T = 500$ fs (a) (guess field $E_0 = 7$ mE_h/ea_0) after 265 iterations, $T = 1.0$ ps (c), (guess field $E_0 = 0.95$ mE_h/ea_0) after 115 iterations and $T = 1.5$ ps (e), (guess field $E_0 = 2$ mE_h/ea_0) after 60 iterations ($\kappa = 1.5$ a.u., $\omega = 637$ cm^{-1}). Panels (b), (d) and (f) show the respective XFROG traces for the three time durations, respectively, for a gate function of width 1000 a.u. and Gaussian tails of width 1000 a.u. (contours in units of a.u.).*

For all time durations the dominant pathway is the asynchronous mechanism. As mentioned before, ϕ_7 is the state which is responsible for the synchronous mechanism. Since the population of ϕ_{12} is increased going from $T = 1500$ fs to $T = 500$ fs as shown in Fig. 3.18 (b) and (f), respectively, one could expect that the contribution of the concerted mechanism should be increased and actually this is the case. The ratio of C_{tot}/S_{tot} is increased from 0.063 to 0.081 for $T = 1500$ fs and $T = 500$ fs, respectively. The probability of the stepwise and concerted mechanism are presented in Fig. 3.18 (b), (d) and (f) for $T = 500$ fs, $T = 1000$ fs and $T = 1500$ fs, respectively. As shown in Fig. 3.18 lower panels, there are one maximum and two maxima for the concerted probability for $T = 500$ fs, $T = 1000$ fs and $T = 1500$ fs, in (b), (d) and (f) panels, respectively. This is in agreement with the population of ϕ_{12} as shown in Fig. 3.18 (a), (c) and (e), respectively. Finally, we note that due to the sparser energy level structure the OCT iteration converges faster since a few number of iterations are needed for all time durations compared with the high barrier case. Further, it is seen from Fig. 3.18, that a 99%, 90% and 82% population of the target state is achieved for $T = 1500$ fs, $T = 1000$ fs and $T = 500$ fs, respectively, which are higher than in the reference symmetric cis high barrier case.

3.5.1 Asymmetry Cis Parameter

Here, we are going to see the effect of adding an asymmetry to the two cis configuration for the lower barrier case. As before $\alpha_{cis} = 0.01$ with the same energy difference of 77 cm^{-1} between the two cis minima. Two time durations, 1500 fs and 1000 fs will be discussed. In these two cases, again the OCT fields look much simpler than in the case
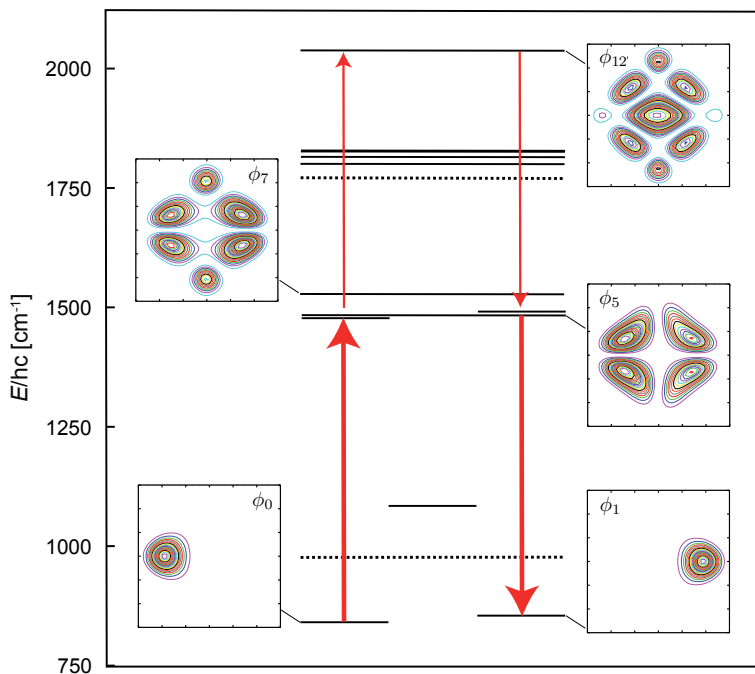
Fig. 3.17 *Level scheme for the low symmetric cis barrier case and probability densities of selected eigenstates which get appreciably populated during the laser driven transfer. The lengths of the horizontal solid bars indicate the range of delocalization of the state with respect to the symmetric coordinate x_s (e.g. ϕ_0/ϕ_1 are localized in the left/right trans minimum, ϕ_2/ϕ_3 (~1100 cm^{-1}) around $x_s = 0$, i.e. in the cis minimum, etc.). The dashed lines correspond to the energy of the barriers for concerted and stepwise transfer. The density plots cover the range $[-1.5 : 1.5]a_0$ along the vertical x_a and the horizontal x_s axes. The vertical arrows indicate the major pathway for laser driven transfer.*

Fig. 3.18 *In panels (a), (c) and (e) the population dynamics for some states are shown, (ϕ_0, ϕ_1, ϕ_5, ϕ_7 and ϕ_{12}) for $T = 500$ fs, $T = 1000$ fs and $T = 1500$ fs, respectively. In panels (b), (d) and (f) are the concerted pathway versus step-wise pathway contributions plotted for $T = 500$ fs (b), $T = 1000$ fs (d) and $T = 1500$ fs (f) which measured by the probability of being in the C and S regions of the PES (low barrier case with $\alpha_{cis} = 0.00$)*
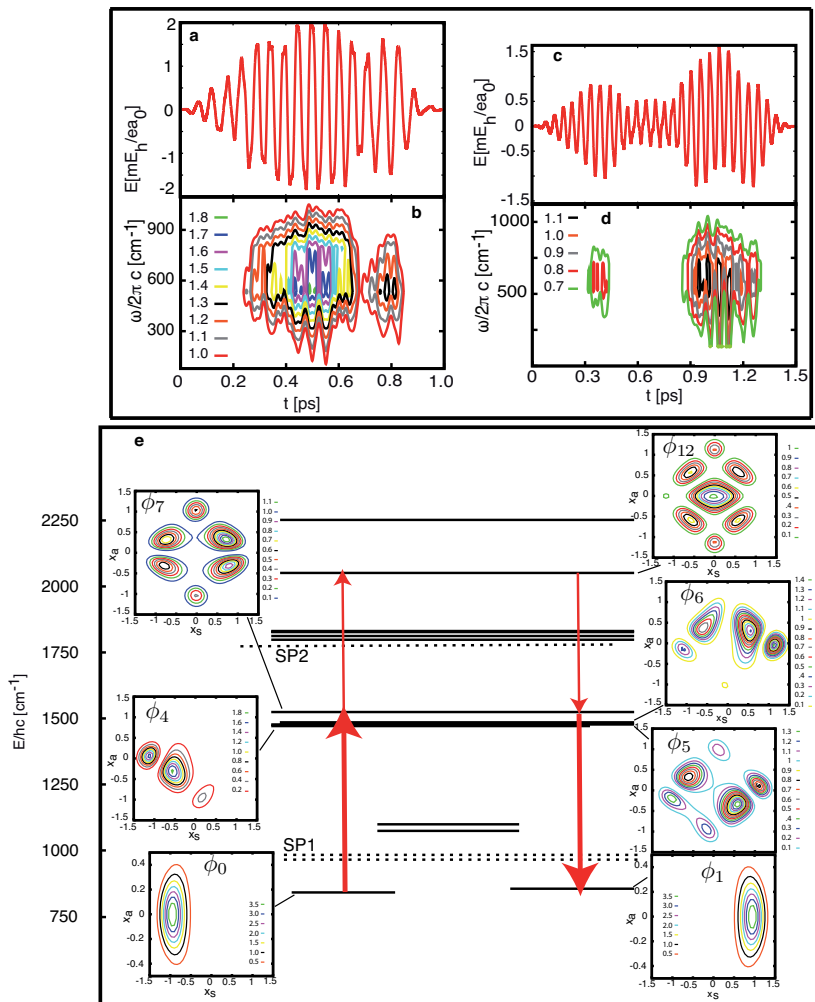
Fig. 3.19 *Laser pulses obtained from OCT and their XFROG for asymmetric cis lower barrier case with $\alpha_{cis} = 0.01$ for $T = 1.0$ ps, (guess field $E_0 = 0.95$ mE_h/ea_0) after 256 iterations (a) and (b) and $T = 1.5$ ps, (guess field $E_0 = 2$ mE_h/ea_0) after 123 iterations (c) and (d) ($\kappa = 1.5$ a.u., $\omega = 637$ cm^{-1}). Panel (e) shows the level scheme for the low barrier asymmetric cis barrier case with $\alpha_{cis} = 0.01$ and probability densities of selected eigenstates which get appreciably populated during the laser driven transfer. The lengths of the horizontal solid bars indicate the range of delocalization of the state with respect to the symmetric coordinate x_s (e.g. ϕ_0/ϕ_1 are localized in the left/right trans minimum, ϕ_2/ϕ_3 ($\sim$1100 cm^{-1}) around $x_s = 0$, i.e. in the cis minimum, etc.). The dashed lines correspond to the energy of the barriers for concerted and stepwise transfer. The vertical arrows indicate the major pathway for laser driven transfer.*

of the high barrier cases. In addition, the XFROG of the fields shows only two subpulses for each time duration as seen in Fig. 3.19 (b) and (d). From the XFROG of $T = 1000$ fs, the first pulse is long with respect to the second pulse which is quite short so, the first pulse depopulates the ground state and at the same time populates the target state and the second pulse completes the target state population as shown in Fig. 3.20 (a). In case of $T = 1500$ fs, the situation is reversed where the first pulse is quite short with respect to the second pulse so, complete depopulation of the ground state is achieved by the second pulse as shown in Fig. 3.20 (d). In other words, the ground state in 1500 fs is depopulated in two steps and the same holds the target state be populated for $T = 1000$ fs.

Fig. 3.20 *Panels (a) and (d) show the population dynamics for some states (ϕ_0, ϕ_1, ϕ_4, ϕ_5, ϕ_6, ϕ_7, ϕ_{12} and ϕ_{15}) which have higher contributions in the population dynamics for $T = 1500$ fs and $T = 1000$ fs respectively. In panels (b) and (e), the comparison between concerted and step-wise pathway for $T = 1500$ fs and $T = 1000$ fs, respectively, is shown as measured by the probab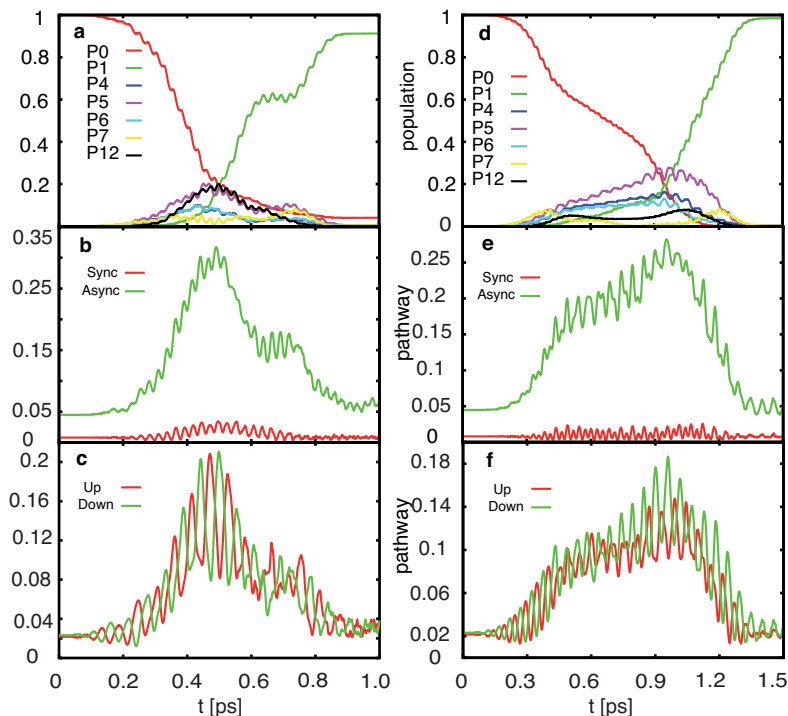ility of being in the C and S regions of the PES. Panels (c) and (f) contain the comparison of the population of the tow cis regions for both time durations $T = 1000$ fs (down right panel) and $T = 1500$ fs (down left panel) where $\alpha_{\text{cis}} = 0.01$.*

The energy level diagram with the involved states in the DPT system is seen in Fig. 3.19 (e). Comparing the asymmetric cis lower barrier case with the symmetric lower barrier case in Fig. 3.17, it is noticed that the low energy states have been affected more in the symmetric one and become more localized in the more stable cis intermediate, see for instance ϕ_4 and ϕ_5 in Fig. 3.19 (e). Also tuning the energy between the two intermediates let these states to have some x_s character and as a result the contribution of the concerted mechanism could increase, but in this case via the tunneling pathway since these states are below the SP2 barrier.

The population dynamics in Fig. 3.20 (a) and (d) show that the dominant pathway

is $\phi_0 \rightarrow (\phi_4, \phi_5, \phi_6$ and $\phi_7) \rightarrow \phi_1$ triggered in a pump-dump like fashion. Moreover, the pulses are broad enough to excite ϕ_7 to the above barrier state ϕ_{12}, which is responsible for the concerted mechanism. Looking at the population dynamics for $T = 1500$ fs in Fig. 3.20 (d), we see that: (i) The ground state starts to depopulate at 150 fs by the first pulse, and at the same time (ii) the $(\phi_4, \phi_5, \phi_6$ and $\phi_7)$ states start to be populated. The target state ϕ_1 starts to be populated later at about 400 fs. (iii) The second pulse completes the depopulation of the initial state which almost reaches zero population at 1100 fs, the intermediate states are depopulated by the second pulse and almost become depopulated about at 1300 fs, and the target states become totally populated at the same time to end with 0.99. For the time $T = 1000$ fs, the initial state is steeply depopulated by the first pulse and at the very end it does not reach to zero population. The target state ϕ_1 and the state ϕ_5 in both cases (the symmetric and the asymmetric lower barrier cases) are similar. In addition, the final population for the target state reaches 0.91 at about 860 fs comparable to the symmetric lower barrier case in which it ends up with 0.9 at about 890 fs .

The probability of different mechanisms, stepwise versus concerted is illustrated in Fig. 3.20 (b) and (e) for $T = 1000$ fs and $T = 1500$ fs, respectively. Farther the probabilities of being in different cis regions are shown panels (c) and (f). In general, the dominant pathway is the asynchronous mechanism via the two cis intermediates. From the energetic point of view the reaction goes through (prefers) the more stable cis intermediate and this is shown in Fig. 3.20 (c) and (f), where the lower region (stable cis intermediate) shows a higher probability than the less stable one for the two time durations. This is attributed to the population of the states ϕ_4 and ϕ_5 which are localized on the more stable cis side as seen from Fig. 3.19 (e). As mentioned before, also the ϕ_4 and ϕ_5 states attain some x_s character, so that the contribution of the concerted mechanism should be increased. This is indeed the case and the ratio of $C_{tot}/S_{tot} = 0.071$ and of $C_{tot}/S_{tot} = 0.095$ for $T = 1500$ fs and $T = 1000$ fs, respectively, has to be compared with 0.063 and 0.088, for the lower barrier symmetric case. Since these states are below the SP2 barrier, the contribution to the concerted mechanism is via tunneling. Also the contribution of the concerted mechanism which goes above the barrier through ϕ_{12} is pronounced in the case of $T = 1000$ fs since this state is populated to a high extent as seen from Fig. 3.20 (e).

3.6   Asymmetric Porphycene: a Case Study

In the following an application of the previous considerations to a molecular system will be presented. Further we show exemplarily to what extent laser-triggered DPT can influence the Förster transfer coupling. Specifically, we will focus on porphycene like structures, which have rather strong hydrogen bonds (HBs) whose properties are widely adjustable by structural design [20]. For the laser-driven DPT the shape of the potential energy landscape is rather important as seen in the previous section. Besides energy barriers which need to be surmounted by excitation with a few IR photons, reactants and products should be energetically different to prevent an efficient back reaction via tunneling. Asymmetrically substituted porphycenes seem to meet these requirements. Below we will consider 9-acetoxy-2,7,12,17-tetra-n-propylporphycene (**4**) (see Fig. 1.1) whose spectroscopy had been studied by Waluk and coworkers [179]. Thus, besides the specific goal of demonstrating a laser-driven switch for molecular photonic wires, our quantum chemical studies of the ground state properties and the $S_0 \rightarrow S_1$ excitation spectrum will shed some light on the effect of symmetric (**3**) and asymmetric (**4**) substitution of the most stable constitutional isomers of porphyrin (porphycene) compound (**2**) and hence will provide the theoretical basis for the assignment of the absorption spectrum.

3.7   Quantum Chemistry

3.7.1   Computational Details

Geometry optimization for the electronic ground state has been performed using density functional theory (DFT) employing the B3LYP hybrid functional together with a 6-31+G(d,p) basis set (see Sec. 3.7.2). Stationary points have been validated by means of frequency calculations. Excitation energies are obtained from time-dependent DFT (TDDFT) calculations at the optimized ground state geometries (vertical excitation) and using the same functional and basis set. All quantum chemical calculations for the ground state and TDDFT are performed with the Gaussian 03 suite of programs [180], while the excited state geometries have been obtained using Gamess US. [181].
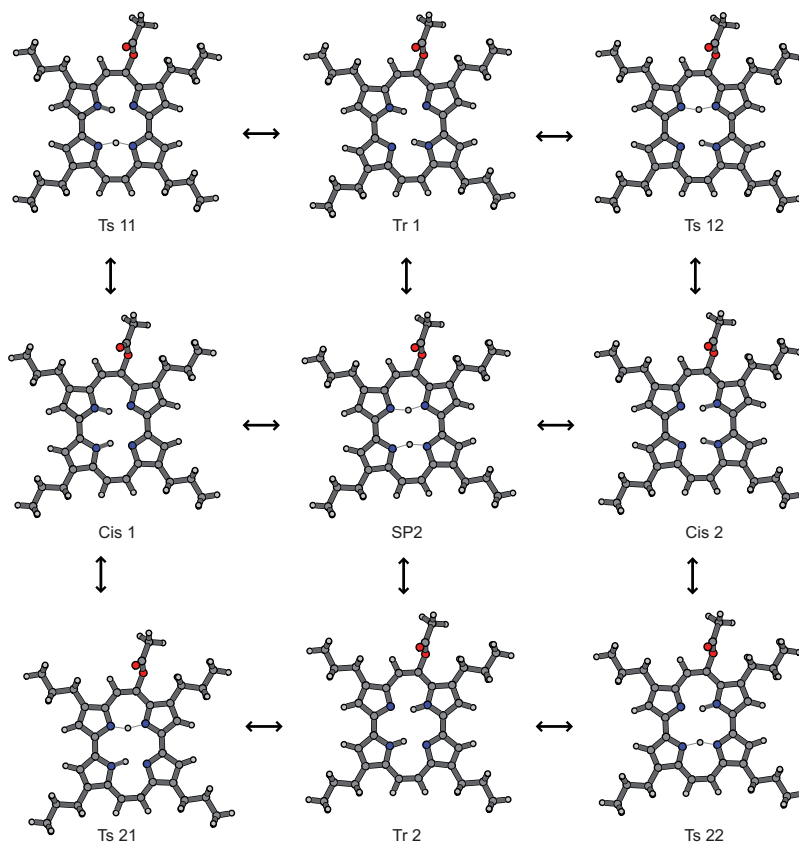
Fig. 3.21   *Optimized geometries (B3LYP/6-31+G(d,p)) of stationary points on the PES of molecule 4 see Fig. 1.1 which are relevant for DPT.*

3.7.2   Optimized Geometries

Ground state optimized structures of **3** (Fig. 1.1) show that this molecule like **2** (Fig. 1.1) is planar in accord with Ref. [20]. Asymmetric substitution, however, causes **4** to become nonplanar with respect to the acetoxy group. Overall **4** has two global trans minima, Tr1 and Tr2, two local cis minima, Cis1 and Cis2, four local maxima which correspond to first order saddle points, Ts11, Ts12, Ts21 and Ts22, and one global maximum being a second

Table 3.1 *Energies and absolute value of dipole moments of stationary points for the tautomerism of the molecules shown in Fig. 1.1 and the values in parentheses are for the electronic excited state of **4** at the B3LYP/6-31+G(d,p) level of theory (values for **2** from Ref. [45]).*

molecule	structure	ΔE (cm^{-1})	dipole (Debye)
4	Tr1	0 (0)	1.633
	Tr2	38 (239)	1.481
	Cis1	726 (603)	2.042
	Cis2	838 (869)	2.218
	SP2	2169 (2530)	1.635
	Ts11	1329	1.539
	Ts12	1505	1.865
	Ts21	1479	1.690
	Ts22	1461	1.834
3	Tr	0	0.002
	Cis	817	1.452
	SP2	2263	0.000
	SP1	1514	0.770
2	Tr	0	
	Cis	804	
	SP2	2256	
	SP1	1637	

order saddle point, SP2. All these structures are shown in Fig. 3.21 and the energetics is compiled in Table 3.1. In terms of the double proton transfer, SP2 is passed in the concerted mechanism, while pathways like Tr1-Ts11-Cis1-Ts21-Tr2 are followed during sequential transfer. Finally, we note from the dipole moments given in the Table 3.1 that **4** is considerably more polar than **3** due to the acetoxy group in the 9 position.

For the ground state, the energetic difference between trans and cis, which is 804 cm^{-1} for **2**, is largely unaffected by the symmetric substitution in **3**. The same holds true for the second order transition state SP2, i.e. the barrier height for concerted DPT is about 2260 cm^{-1}. The barrier for stepwise proton transfer which is 1637 cm^{-1} for **2** decreases slightly to 1514 cm^{-1} in **3**. Upon asymmetric substitution with an acetoxy group in the 9 position in **4** most notably in comparison with **3** is the asymmetry of the two trans tautomers which amounts to 38 cm^{-1}. This rather small value is in good accord with the experimental finding of indistinguishable tautomers [179]. Further, the SP2 transition state is lowered by about 4% and the first order saddle points and cis minima are changed in a way such as to make a stepwise DPT via Cis1 energetically more preferable.

For the first excited electronic state, optimized geometries for all minima and SP2 maximum have been determined using quantum chemistry calculations. The energetic values are given in parenthesis in the Table 3.1. The energetic difference between the two trans minima is 239 cm^{-1} for the S$_1$ PES comparing to 38 cm^{-1} between the two trans minima for the S$_0$ PES. And, the picture that emerges is that from a nearly symmetric double well potential in S$_0$ to an asymmetric one in S$_1$. Hence, the equilibrium between Tr1 and Tr2 in the first excited state is shifted toward the Tr1, in other words, the hydrogens are completely localized in the Tr1 and this is in agreement with Ref. [179]. Excited state calculation shows a higher SP2 barrier of 2530 cm^{-1} comparing to 2169 cm^{-1} for the electronic ground state, hence the DPT reaction becomes less probable in the excited state than the ground state and this is in line with the HB distance in the excited state which is larger than in the ground state.

The results on the HB geometries for the ground state of **4** are compiled in Table 3.2

Table 3.2 *Geometric parameters characterizing the HBs in 4 for the ground state, values are for the excited S_1 state for 4 (and for Tr in 2 and 3) at the B3LYP/6-31+G'(d,p) stationary points (bond lengths in Ångstrom, angles in degrees, data for 2 are taken from Ref. [182]).*

structure	N_1-H_a	N_2-H_a	N_1-N_2	$\angle N_1$-H_a-N_2	N_3-H_b	N_4-H_b	N_3-N_4	$\angle N_3$-H_b-N_4
Tr1	1.05 (1.04)	1.70 (1.74)	2.67 (2.69)	150.9 (150.0)	1.68 (1.7)	1.05 (1.05)	2.65 (2.67)	152.9 (152.1)
Tr2	1.67 (1.7)	1.05 (1.05)	2.66 (2.68)	154.9 (154.5)	1.05 (1.05)	1.68 (1.7)	2.65 (2.67)	153.0 (152.5)
Cis1	1.06 (1.05)	1.64 (1.68)	2.62 (2.65)	152.6 (151.6)	1.07 (1.06)	1.61 (1.64)	2.61 (2.63)	155.1 (154.8)
Cis2	1.60 (1.63)	1.07 (1.6)	2.62 (2.64)	156.5 (156.2)	1.61 (1.64)	1.07 (1.06)	2.61 (2.63)	154.0 (153.5)
SP2	1.29 (1.23)	1.25 (1.32)	2.51 (2.51)	159.4 (158.0)	1.27 (1.24)	1.27 (1.29)	2.50 (2.5)	159.1 (160.3)
Ts11	1.06	1.61	2.60	153.1	1.30	1.25	2.51	159.2
Ts12	1.30	1.26	2.52	159.6	1.57	1.07	2.58	154.8
Ts21	1.26	1.31	2.52	159.2	1.07	1.57	2.58	155.3
Ts22	1.57	1.07	2.59	156.8	1.30	1.25	2.52	158.9
2	1.05	1.69	2.67	152.6				
1	1.05	1.68	2.66	152.8				

which also contain values for the trans tautomers of **2** and **3**. Comparing the most stable trans forms of the three molecules the differences in HB parameters are rather small. Most notably again is the asymmetry, i.e. in Tr1 of **4** the HB that is far from the acetoxy substitution site (N_1-H_b-N_2) is slightly shorter and substantially more linear as compared with the N_3-H_a-N_4 HB that is close to the acetoxy substituent. The geometric signature of the energetically more preferable path for stepwise DPT can be found in the stronger contraction of the N_3-H_b-N_4 HB in Ts11 as compared with the N_1-H_a-N_2 HB in Ts12. The transition states for the second transfer step, Ts21 and Ts22, on the other hand, have almost the same HB parameters.
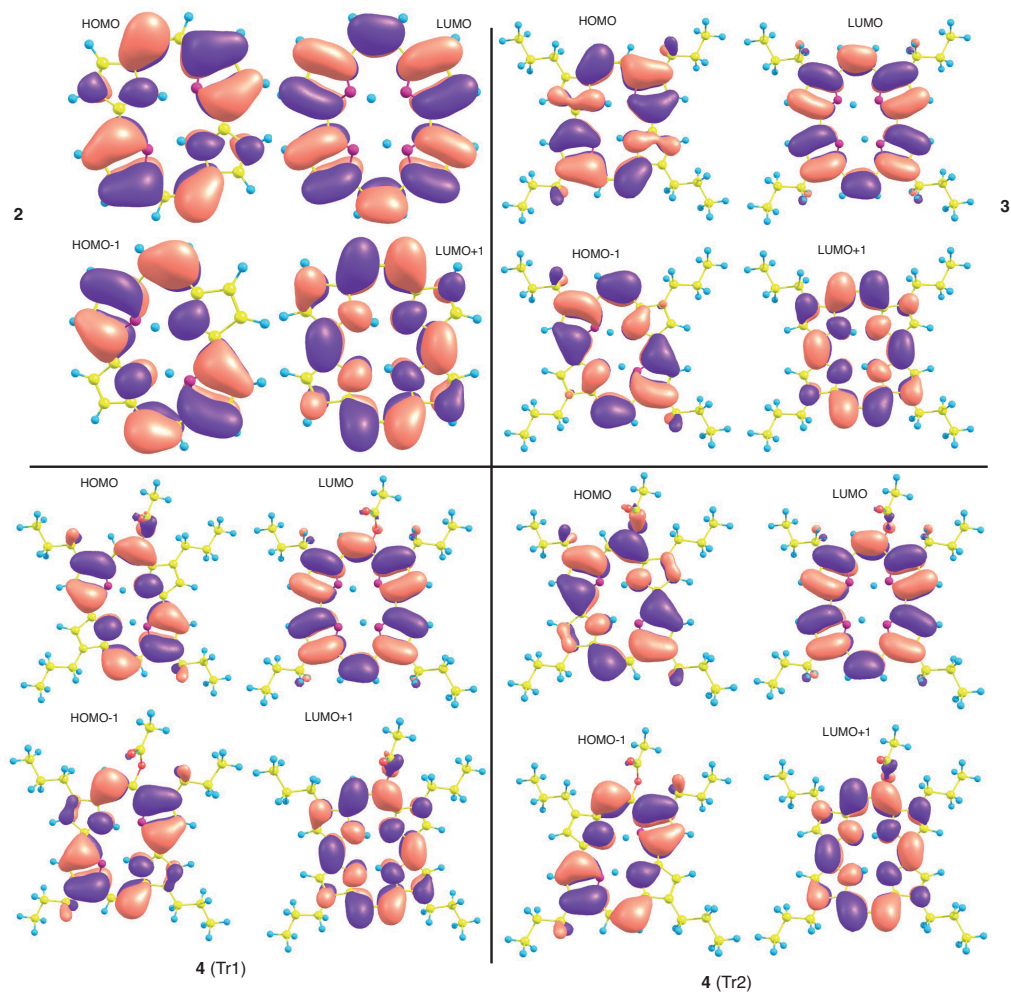
Fig. 3.22 *Molecular orbitals relevant for the $S_0 \rightarrow S_1$ transition (cf. Table 3.4) for molecules **2**, **3**, and the two tautomers of **4**. The orbital numbers are 80-83 (**2**), 128-131 (**3**), and 143-146 (**4**).*

The results on the HB geometries for the excited state geometries of **4** are compiled in the Table 3.2 (values in parenthesis). The HB parameters show a small increase in lengths and nonlinearity and as a result, the hydrogen bonding becomes weaker in the excited state. Most probably, the molecule expands upon excitation, and the inner cavity becomes larger since the bonding in the molecule is weaker in the excited state. With

Table 3.3 *Energies (a.u.) of frontier molecular orbitals obtained by B3LYP/6-31+G(d,p) method for the studied molecules and HOMO−LUMO energy gap.*

Orbitals	2	3	Tr1	Tr2
LUMO+1	-0.06760	-0.06140	-0.06427	-0.06416
LUMO	-0.11533	-0.10193	-0.10502	-0.10479
HOMO	-0.20458	-0.19259	-0.19546	-0.19421
HOMO−1	-0.20675	-0.19422	-0.19678	-0.19792
Energy gap	0.08925	0.09066	0.09044	0.08942

Table 3.4 *Vertical excitation energies (in cm^{-1}) and oscillator strengths (in parenthesis) obtained at the TD-DFT B3LYP/6-31+G(d,p) level of theory. The calculated values for the different structures are compared with the experimental assignment from Refs. [179] (3,4) and [183] (2). Note that the experimental values correspond to the respective 0-0 transition.*

struct.	calc.	exp.	leading excitation	Excitation Amplitude
4(Tr1)	17392 (0.15)	15708	144→145	0.58
4(Tr2)	17670 (0.13)	15993	143→145	0.58
3	17536 (0.14)	15983	128→130	0.48
2	17904 (0.12)	16000	80→82	0.56

respect to the HB that is next to the acetoxy group, the HB lengths in Tr1 and Tr2 in the excited state are 1.74 and 1.70 Å. So, one could say that, the SP1 for the weaker HB in (Tr1) is higher than the stronger HB in (Tr2). As a result, the hydrogen atom is more localized in Tr1 than in Tr2. But with respect to the HBs parameters that are far from the acetoxy group, they do not change much in both Tr1 and Tr2 for the ground and the excited states.

3.7.3 Molecular Orbitals and Excited States

Investigating the highest occupied molecular orbital (HOMO) and the one before (HOMO−1) indicates they are π type orbitals and the lowest unoccupied molecular orbital (LUMO) and the second unoccupied molecular orbital (LUMO+1) indicates they are π^* type orbitals for all studied molecules. Different molecular orbital energies and HOMO−LUMO energy gaps of the studied molecules are presented Table 3.3. In this work free base porphycene (**2**) Fig. 1.1 is considered as the reference molecule. The substitutions by n-propyl groups to obtain tetra-n-propylporphycene (**3**) Fig. 1.1, n-propyle groups and acetoxy group to obtain acetoxy-tetra-n-propylporphycene (**4**) Fig. 1.1 disturb the energies of the HOMOs and LUMOs and as a result the HOMO-LUMO gap changes. For example the HOMO-LUMO gap for Tr1 becomes smaller than the HOMO-LUMO gap for **3** so, the $S_0 \rightarrow S_1$ energy decreases.

In the following we will discuss the $S_0 \rightarrow S_1$ transition, which contributes to the Q absorption band. Results of TDDFT calculations are compared with experimental data in Table 3.4 for the different compounds. First, we notice that TDDFT gives excitation energies which exceed the experimental ones by about 1500 - 2100 cm^{-1}. Most of this difference must be attributed to the method itself (see, e.g., systematic study in Ref. [184]). Further deviations might be due to the fact that the experimental values correspond to the 0-0 transitions whereas the calculations are performed for a vertical excitation. Comparing the experimental spectra of porphycenes in gas and condensed phases the environmental effects (e.g., a nitrogen matrix in Ref. [179]) is negligible [20].
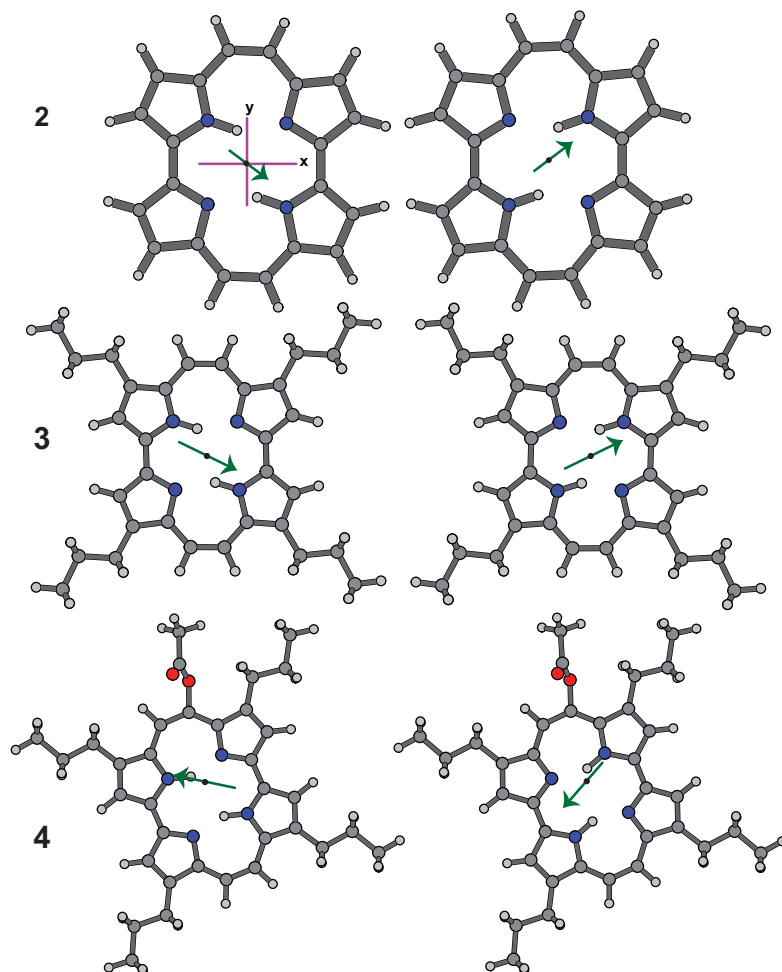
Fig. 3.23 *Transition dipole moment vectors for structures **2** (left) (1.252,-0.950), **3** (left) (-1.489,0.672), **4** (Tr1) (-1.652,0.356), and **4** (Tr2) (-1.042, 1.174) (in Debye).*

Let us focus on the tautomerization of **4**. As discussed in Section 3.7.2 the energetic asymmetry in the electronic ground state is rather small. The measured splitting in the $S_0 \rightarrow S_1$ transition, however, gave evidence for a considerable asymmetry in the excited states of 285 cm^{-1} [179]. The assignment of the most stable tautomer in the S_1 excited state has been based on a semiempirical ZINDO/S calculation. Considering Table 3.4 we notice that the agreement of the splitting in the $S_0 \rightarrow S_1$ transitions (278 cm^{-1}) is rather good thus giving strong support for the experimental conclusions in Ref. [179].

The $S_0 \rightarrow S_1$ transitions are of $\pi \rightarrow \pi^*$ type with participation of the π (HOMO, HOMO-1) and π^* (LUMO, LUMO+1) molecular orbitals (MOs). These orbitals are shown for the different molecules in Fig. 3.22 and the excitation amplitudes are compiled in Table 3.4. The main contributions to the $S_0 \rightarrow S_1$ transition in **2** and **3** is of HOMO-1 $\rightarrow$ LUMO type (see also Ref. [185]). The same holds true for the less stable tautomer Tr2 of **4**. Interestingly, in tautomer Tr1 of **4** this transition is of HOMO $\rightarrow$ LUMO type. Comparison of the MOs of Tr1 and Tr2 shows that the order of HOMO and HOMO-1 is *reversed* upon tautomerization.

A closer look at the orbitals reveals the effect of symmetric and asymmetric substitu-
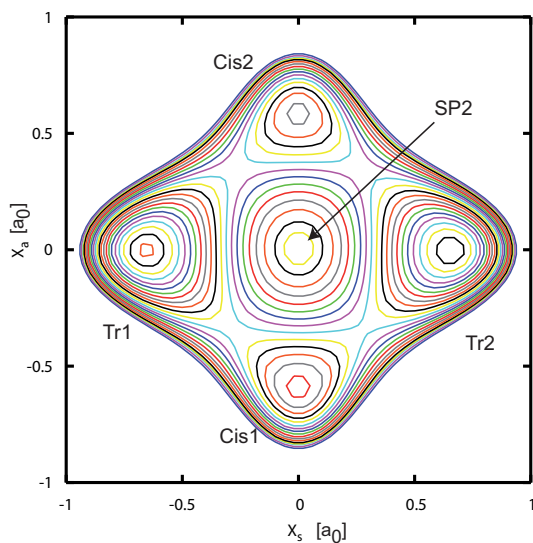
Fig. 3.24 *Two-dimensional model potential according to Eq. (3.5) for the DPT in 4. The parameters are $U_0 = 876\ cm^{-1}$, $x_0 = 0.624\ a_0$, $g = 0.435$, $\alpha_{\mathrm{trans}} = 0.0095$, and $\alpha_{\mathrm{cis}} = 0.034$. The barrier height for concerted transfer is $2169\ cm^{-1}$. The energetic difference between the two trans minima is $38\ cm^{-1}$ and the energies of the cis minima are $725\ cm^{-1}$ and $838\ cm^{-1}$ (contour lines are in steps of $400\ cm^{-1}$ from $400\ cm^{-1}$ to $8800\ cm^{-1}$).*
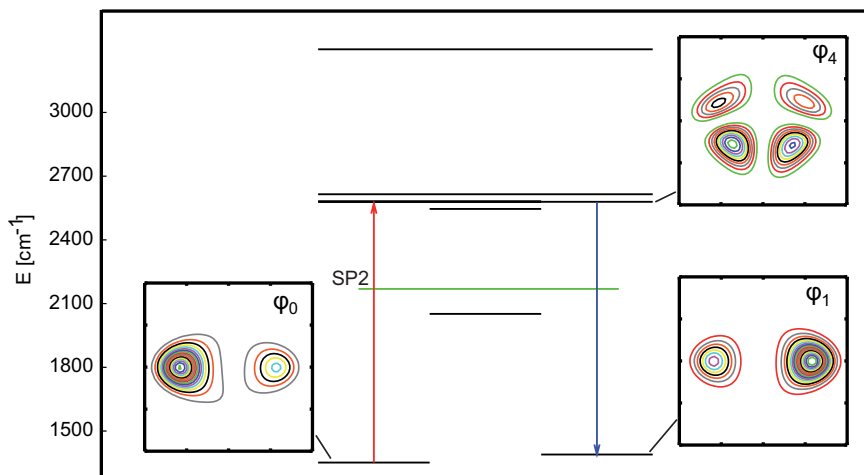
Fig. 3.25 *Energy level scheme of the model Hamiltonian for 4 including the probability densities of those states which dominate the dynamics. The lengths of the horizontal lines indicate the area of delocalization of the wave function along the x_s coordinate. The green line corresponds to the energy of the SP2 barrier. The vibrational eigenstates have been obtained using the improved relaxation scheme within MCTDH [164]. The pathway of laser-driven pump-dump control is marked by vertical arrows. The density plots cover the range $[-1 : 1]\, a_0$ along the vertical x_a and the horizontal x_s axes.*

tions. Going from **2** to **3** some electron density appears at those alkyl chains which are opposite to the position of the hydrogen bonded H atom. Overall, however, the MOs are

rather similar, i.e. in the HOMO there is a *p*-orbital at those nitrogens, which are bonded to the central hydrogens whereas there is no electron density at the "free" nitrogen atoms. In the HOMO-1 this situation is reversed. Asymmetric substitution causes a disturbance of the porphycene π-system by the acetoxy group with the effect being different for the two tautomers. Tr2 of **4** resembles the HOMO in **2** and **3** with some electron density at the acetoxy group. In Tr1 of **4** the presence of the latter electron density renders the Tr2-HOMO-1 to become more stable than the Tr2-HOMO.

3.7.4   Transition Dipole Orientation

The directions of the transition dipole moments for the $S_0 \rightarrow S_1$ transitions of the different molecules are compiled in Fig. 3.23. Comparing **2** and **3** we notice that symmetric substitution has almost no effect on the direction of the transition dipole moments. Furthermore, both cases show the well-known 90 degree change of the transition dipole moment upon tautomerization [79]. The presence of the acetoxy group in **4**, however, changes this picture due to the polarity introduced by the oxygen atoms. Most notably is the fact that the tautomerization causes a tilt of the transition dipole moment by about 50 degrees only. So it has been shown that, the direction of the transition dipole moment depends mainly on the position of the hydrogen atoms in the internal cavity of in the porphyrin like structures. The Förster energy transfer mechanism [108] between different chromophores relies on the coupling between these chromophores which is given by the transition dipole moment orientation. So, one could use DPT (*switching between the ground state tautomers*) triggered by ultrafast laser pulse in IR regime to control this energy transfer or at least modify the strength of the Förster transfer coupling. Let us assume that **4** is built into a molecular photonic wire (compare Fig. 1.6). The Förster energy transfer coupling between different molecular subunits of the wire called donor (D) and acceptor (A) is given by [108]

$$J_{DA} = \kappa_{DA} d_{10}^{(D)} d_{10}^{(A)} \frac{1}{R_{DA}^3} \,. \tag{3.8}$$

Here, $d_{10}^{(A/D)}$ is the magnitude of the transition dipole moment for the $S_0 \rightarrow S_1$ transition and R_{DA} is the distance between donor and acceptor. Most important for the present discussion is the orientational factor given by

$$\kappa_{DA} = \mathbf{n}_A \cdot \mathbf{n}_B - 3(\mathbf{e}_{DA} \cdot \mathbf{n}_D)(\mathbf{e}_{DA} \cdot \mathbf{n}_A)\,, \tag{3.9}$$

where $\mathbf{n}_{D/A}$ and $\mathbf{e}_{DA}$ are the unit vectors pointing in the directions of the transition dipole moment of D/A and the center to center DA distance, respectively.

In order to estimate the effect of DPT on the Förster transfer coupling and in particular on the orientational factor we suppose that **4** is built into the wire such that the neighboring unit has a transition dipole moment like structure **2**. This could be the case, for instance, for the widely used porphyrins. Let us further assume that $\mathbf{e}_{DA}$ points along the x-direction. In this case we obtain $\kappa_{DA}(\text{Tr1}) = 1.43$ and $\kappa_{DA}(\text{Tr2}) = 0.60$. In other words the transfer coupling changes by about 60% as a consequence of the tautomerization.

3.8   Quantum Dynamics

3.8.1   Ground State Model Hamiltonian

The potential energy surface for DPT in the electronic ground state for this asymmetric substituted porphycene will be modeled using the same Hamiltonian in Eq. 3.5 which was introduced by Smedarchina and coworkers [36, 39] and which has been supplemented by asymmetric terms to mimic systems like **4** in Ref. [37].

Hamiltonian Eq 3.5 with parameters obtained by fitting to the quantum chemical results of Table 3.1. The resulting potential energy surface is plotted in Fig. 3.24 and the fitting parameters are given in the figure caption. Note that while the minima and the SP2 maximum are in good agreement with the quantum chemistry results, the simple form of the potential does not provide enough flexibility for obtaining all first order transition states (SP1) at the same time with comparable accuracy. The deviations range from 51 cm^{-1} to 169 cm^{-1}, comparing to the quantum chemistry calculations for these SP1 which is, however, still acceptable given the overall approximate nature of the treatment. x_0 is introduced in Sec. 3.2 in Eq. 3.2 as half of the transfer distance of the hydrogen atom. Again, $2x_0 = a - 2r\cos\theta$, where a is N-N distance, r is the $N - H$ bond length and θ is the $\angle$ H-N-N which express the non-linearity of the hydrogen bond. Here, the two hydrogen bonds are not symmetric due the substitution of acetoxy group as introduced before. So, x_0 is taken as the average of the half of transfer distance in both hydrogen bonds in Tr1 conformer. For parameters, (see Table 3.2) and for θ ($\angle$ H-N-N), they are 18.1° and 16.7 ° for both hydrogen bonds. Using these parameters, x_0 for this molecule is 0.624 a_0.

For the interaction with the laser field we assume that the permanent dipole moment depends only linearly on the coordinates, as introduced in Eq. 3.6. Where $\mu_{a/s}$ is the derivative of the dipole moment with respect to $x_{a/s}$. The permanent dipole moment changes mostly along one polarization direction (x, cf. Fig. 3.23). Assuming the laser being linearly polarized along that direction and making a linear interpolation between the minimum configurations we obtain $d_s = -0.028$ e and $d_a = 0.150$ e.

For the laser field we will use the following form

$$E(t) = \sum_{i=1,2} E_{0,i} \cos(\omega_i t) \exp(-(t - t_{0,i})^2/2\tau_i^2) \qquad (3.10)$$

which facilitates the consideration of the so-called pump-dump control mechanism [74, 186]. In Eq. (4.7) $E_{0,i}$ is the laser amplitude, ω_i the carrier frequency, and τ_i the temporal width of the pulse centered at $t_{0,i}$.

3.8.2   Laser Control of DPT in the Electronic Ground State

The two-dimensional time-dependent Schrödinger equation has been solved using the MCTDH approach [161, 156] as implemented in the Heidelberg program package [160] with the same numerical implementation as in Sec. 3.3. The only diffrence from there is the border of the coordinates, here they are (64 points within [-1.5:1.5] a$_0$).

In the following we will investigate the possibility to control the DPT in **4** using a simple two pulse pump-dump scheme involving an intermediate state which is energetically above the reaction barrier for concerted DPT (cf. Fig. 3.25). The initial state is localized mostly in the Tr1 well, while the final state lies mostly in the Tr2 well. Due to the low barrier and the small asymmetry both states have finite probabilities in the respective other wells. The goal is to find an electric field of the form given by Eq. (3.10), for which the first (pump) pulse populates the intermediate state and the second (dump) pulse
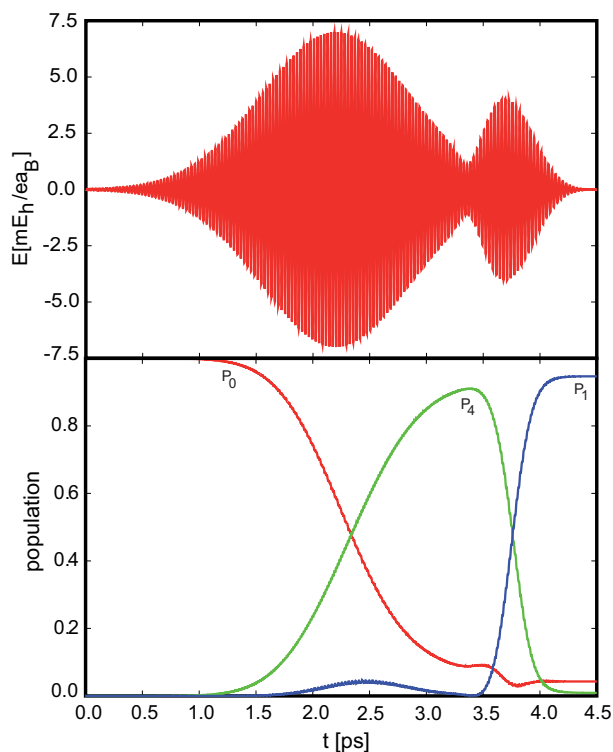
Fig. 3.26 *Upper panel: Electric field for the pump-dump control scheme (pulse parameters: $E_{0,1} = 7$ mE$_h$/ea$_0$, $\omega_1 = 1111$ cm^{-1}, $t_{0,1} = 2200$ fs, and $\tau_1 = 650$ fs); ($E_{0,2} = 4$ mE$_h$/ea$_0$, $\omega_2 = 1055$ cm^{-1}, $t_{0,2} = 3750$ fs, and $\tau_2 = 200$ fs). Lower panel: Population dynamics of the states φ_0, φ_1, and φ_4*
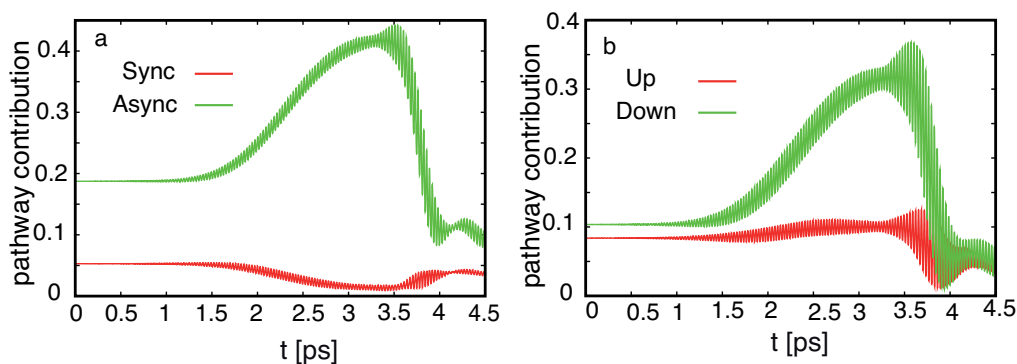
Fig. 3.27 *Concerted pathway versus step-wise pathway for asymmetric porphycene (a), which is measured by the probability of being in the C and S regions of the PES according to the defined step functions, the probability of being in the down (more stable cis) S region and upper (less stable cis) S region of the PES.*

triggers a transition from this intermediate to the product state. This scheme operates in complete analogy to other isomerization reactions studied previously, such as the single H-atom transfer in malonaldehyde [186] or the cope rearrangement in semibullvalenes

[74]. The parameters for the present case of DPT were chosen as follows: First, the field strength is fixed at a certain value and the pulse length is increased starting from 800 fs until the intermediate state population reaches a maximum. For this pulse length the field amplitude is changed around its starting value to check whether the intermediate state population can be increased. The carrier frequency is chosen to correspond to the respective transition frequency. The same procedure is followed independently for the dump pulse by letting it start immediately after the pump pulse. This gave a total pulse duration of 5 ps during which the population of the intermediate state showed a plateau, which allowed us to shift the dump pulse such that pump and dump pulse partly overlap (cf. Fig. 3.26) then the final propagation time becomes 4.5 ps.

The progress of the laser-driven reaction can be followed by calculating the populations of vibrational eigenstates of the model Hamiltonian. A representation of the energy level scheme is given in Fig. 3.25 which also shows the probability density of those states which dominate the dynamics. The chosen above-barrier transition state involves an excitation of the asymmetric stretching coordinate x_a which triggers the reaction to occur mostly along the stepwise pathway (see also Sec. 3.4 and Sec. 3.5). Furthermore, it is seen that the probability density has a higher weight in that part of the potential where $x_a < 0$, implying that there is a preference for the Cis1 minimum to be visited during the dynamics. According to our previous study (see Sec. 3.4.2 and Sec. 3.5.1) this is due to the higher stability of Cis1 as compared with Cis2. In fact, this is the case as the discussion below concerning the pathways of DPT. Finally, we note that there are several states in the region of the chosen intermediate state φ_4, thus state selective population will be more easily achieved using long pulses as compared, e.g., with the NH-vibrational stretching frequency.

The optimized field and selected state populations are shown in Fig. 3.26. The pump pulse excites the system from the ground state ground state, φ_0, to the intermediate state φ_4, while the dump pulse de-excites this population to the target state φ_1. The maximum intermediate state population is 91 %, reached around 3.4 ps. At this time, however, the dump pulse is already transferring population from φ_4 to the target state φ_1. The overall duration of the laser-induced DPT process is 4.5 ps and the final population of the target state is 95 %. Two minor features seen in Fig. 3.26 deserve a comment. Around 2.4 ps there is some transient population of the target state already due to the pump pulse. Later on around 3.6 ps the dump pulse also is seen to further depopulate the initial ground state. Both effects can be traced to the fact that the energetic separation between the two transitions is only 56 cm^{-1}, i.e. they can be simultaneously addressed by the laser pulse spectra.

For the investigation of the DPT mechanisms for this molecule , three step functions have been used to define each area in the PES, the concerted area, Cis1 (down area) and Cis2 (upper area). For the concerted area, $(\theta(x_s - (-0.35)) \, \theta(0.35 - x_s) \, \theta(x_a - (-0.0963) \, \theta(0.0963 - x_a))$, Cis1 (more stable cis in down area) $(\theta(x_s - (-0.35)) \, \theta(0.35 - x_s) \, \theta(-0.0963 - x_a))$ and Cis2 (less stable cis in upper area) $(\theta(x_s - (-0.35)) \, \theta(0.35 - x_s) \, \theta(x_a - 0.096))$ have been used. With respect to the concerted area, the width of the vibrational ground state is used. The different pathway contributions, concerted versus stepwise as well as the stepwise via Cis1 and the stepwise via Cis2 are presented in Fig. 3.27 (a) and (b), respectively. It has been shown that, the dominant pathway for DPT in this molecule is the stepwise mechanism and very low contributions of the concerted mechanism is pronounced Fig. 3.27 (a). Further, the stepwise of DPT prefers the more favorable energy way as noticed from the pathway contribution of the more stable cis (down area) as clearly shown in Fig. 3.27 (b).

3.9 Summary

In summary, a two-dimensional model has been used to describe DPT reactions. Specifically, optimal control theory has been used to get the optimal electric field that triggers ultrafast double proton transfer. It has been shown that the optimized field, mechanism of DPT and the involved states in the isomerisation reaction depend on the time duration of the field and on the Hamiltonian parameters, U_0, excitation directions x_a and x_s and asymmetry parameter α_{cis}.

It has been seen that the field for the longer propagation time looks very complicated compared with the shorter propagation time. The stepwise transfer was found to be the major way for the DPT mechanism since the initial excitation of wavepacket is along the asymmetric coordinate. The concerted pathway has a minor contribution in the total mechanism since the dipole moment in this direction is very small. Actually the concerted pathway is relevant when a state of mixed character is involved in the transfer. For the high barrier case, different states are involved in the reaction through a multiple pump-dump mechanism. But for lower barrier case, the number of involved states is small, i.e. the ground, target and intermediate state and the mechanism is according to a pump-dump scheme. The asymmetry parameter α_{cis}, has affected the involved states as well as the amount of concerted pathway to the total transfer. As an application, the DPT in 9-acetoxy-2,7,12,17-tetra-n-propylporphycene (**4**) (see Fig. 1.1) has been studied. It has been shown the transition dipole moment depends mainly on the position of the protons in porphycene-like structures so, laser control of DPT provides a means for switching the dipole orientation. This could provide an ultrafast switch of the energy transfer through the molecular photonic wires instead of classical switch.

Future extensions of this study could include the account for more degrees of freedom such as heavy atom motions and the integration into a simulation of energy flow in molecular photonic wires.

CHAPTER 4

Laser Driven Vibrational Dynamics of $Mn_2(CO)_{10}$

4.1 Overview

In this chapter, the results concerning the computational chemistry calculations as well quantum dynamics calculations for $Mn_2(CO)_{10}$ are discussed. In the next section, the quantum chemistry characterization (computational details, optimized geometries, harmonic frequencies and normal modes analysis) is given. In the next section, Quantum dynamics are discussed. For instance, 10D PES of all CO modes is obtained and then the anharmonic frequencies of CO modes are calculated by Fourier transformation of dipole-dipole autocorrelation function. Next, CPL in IR domain is used to excite degenerate active CO modes to provide pseudorotation of the molecule (wavepacket circulation). At the end, two-dimensional PES for the CO dissociation (axial and equatorial) is obtained and discussed.

4.2 Quantum Chemistry Calculations

4.2.1 Computational Details

The calculations reported in this part of the thesis are based on density functional theory (DFT) using BP86 functional as implemented in Gaussian 03 package [180]. This functional is chosen because it has been noted [187, 188] that it gives reliable results for transition metal carbonyl complexes.

The fully optimized contracted Gaussian basis sets with triple zeta valence polarization (TZVP) [140, 141] for all atoms are used for geometry optimization, frequency calculation and PES calculations. The calculations of $Mn_2(CO)_{10}$ were performed for D_{4d} (staggered structure) and D_{4h} (eclipsed structure) point group symmetries, Fig. 4.1. C_{4v} and C_s point group symmetries are retained along the reaction paths corresponding to the dissociation of axial and equatorial CO, respectively.
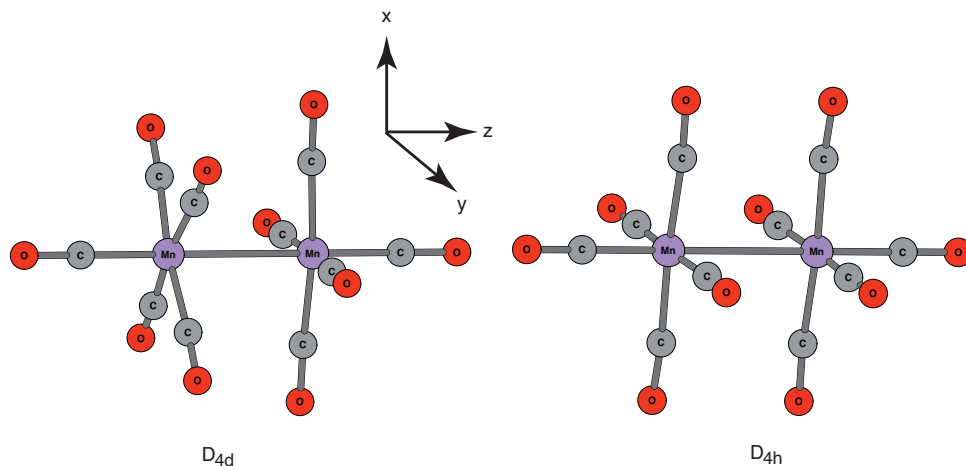
Fig. 4.1 *Optimized geometries of Mn$_2$(CO)$_{10}$ in D$_{4d}$ and D$_{4h}$ point group symmetries using the BP86/TZVP level of theory.*

Table 4.1 *Calculated properties for the optimized D$_{4d}$ and D$_{4h}$ geometries (bond lengths are in Ångstrom and bond angles are in degrees), ^{a}Reference [189], ^{b}Reference [190].*

Property	D$_{4d}$	Expt^a	Expt^b	D$_{4h}$
Mn–Mn	2.97	2.98	2.90	3.11
Mn–C$_{ax}$	1.81	1.80	1.82	1.80
Mn–C$_{eq}$	1.85	1.87	1.86	1.90
C$_{ax}$ –O$_{ax}$	1.16	1.15	1.15	1.16
C$_{eq}$ –O$_{eq}$	1.15	1.15	1.14	1.08
∠C$_{ax}$–Mn–C$_{eq}$	93.40	93.40	93.94	92.30
∠O$_{eq}$–C$_{eq}$–Mn	177.00	177.77	178.61	175.00
∠Mn–Mn–C$_{eq}$	86.60	86.60	86.10	87.60

4.2.2 Optimized Geometry and Normal Modes

For geometry optimization two structures of the Mn$_2$(CO)$_{10}$, namely D$_{4d}$ (staggered structure) and D$_{4h}$ (eclipsed structure,) have been studied. Since the experimental (electron diffraction in the gas phase [189] and X-ray diffraction at room temperature [191]) and at 74 K [190] results for Mn$_2$(CO)$_{10}$ confirmed the staggered structure, the frequency calculations as well as the PES for the dissociation channels of CO have been done for that structure. The optimized parameters for both structures, the staggered D$_{4d}$ along with the structural data from Refs. [190, 189] which are averaged over the bond lengths and bond angles, and the eclipsed D$_{4h}$ are introduced in Table 4.1. Computational chemistry confirmed that D$_{4d}$ is in agreement with the experiment, the most stable isomer i.e. a global minimum with all real vibrational frequencies. The Mn-Mn bond distance is 2.97 Å which is in a good agreement with the experimental results as shown in Table 4.1. The Mn-Mn bond should be a single bond in order to obey the 18-electron rule. The other parameters, e.g. the distances Mn-C$_{ax}$, Mn-C$_{eq}$, C$_{ax}$ -O$_{ax}$, C$_{eq}$ -O$_{eq}$ and the bond angles are also in a good agreement with the experiment. The eclipsed structure of Mn$_2$(CO)$_{10}$ has an energy 4.6 kcal/mol higher than the D$_{4d}$ global minimum structure and a 3.11 Å Mn-Mn bond distance, i.e. slightly longer than the corresponding one in the

stable D_{4d} structure. The higher energy and longer Mn-Mn bond distance of this structure is attributed to the repulsion between of equatorial CO groups. The corresponding normal modes for this D_{4h} structure show an imaginary vibrational frequency of (22i cm^{-1}) which is related to A_{1u} point group symmetry. Actually this vibrational mode involves the rotation of each of Mn atoms around z-axes with small angle against each other in order to end up with the global minimum D_{4d} structure. So, D_{4h} is a transition state with very a small imaginary frequency for the most stable D_{4d} structure. The computed IR vibrational spectra for the D_{4d} structure for $Mn_2(CO)_{10}$ are introduced in Table 4.2. It is shown that our theoretical predictions using BP86/TZVP level of theory are in rather good agreement with the experimental IR spectra. It is seen that, there are four CO active normal modes, 1988 cm^{-1} (B_2), 2014 cm^{-1}(E_1, doubly degenerate) and 2045 cm^{-1} (B_2)

The active normal modes are presented in Fig. 4.2. It is shown that, these four CO active modes are delocalized modes all over the whole molecule. And, this makes the dissociation of CO harder because before the dissociation, a way should be found to covert these delocalized vibrations into local one. Investigating the polarization of these CO active normal modes showed that, the degenerate E_1 modes are polarized in x- and y-directions (the axes are shown in the figure), but the other two less intensity B_2 modes are polarized in z-direction. Also the harmonic IR-line spectra came out from the calculation are introduced in Fig. 4.2. In Fig. 4.3, the remaining CO vibrational modes and some of low frequency modes are introduced. It is seen that, these modes are also delocalized modes.

Actually three tasks will be discussed in the following. The first one is obtaining the anharmonic CO vibrational frequencies, the second one is CO wavepacket circulation and the last one creating an anharmonic PES and then discussing the quantum dynamics of non-statistical Mn-CO bond breaking in the ground state. For the first task, three active modes (degenerate E_1 active modes 2014 cm^{-1} and higher intensity B2 mode 2045 cm^{-1}) are chosen for creation of the anharmonic PES and subsequent calculation of the anharmonic IR-spectrum. For the second task, only the degenerate E_1 active modes 2014 cm^{-1} are chosen in order to achieve wavepacket circulation around the principal axis. For the last task, it depends on which Mn-CO bond will be broken. Two-dimensional (R_{MCO} and r_{CO}) PES for the axial and equatorial CO groups is calculated assuming that, the delocalized CO vibrations are superimposed to have this local vibrations. Then, non-stastical Mn-CO bond breaking is discussed without direct laser excitation but using displaced ground state wavepacket instead.

4.3 Quantum Dynamics

4.4 Model Hamiltonian for Anharmonic Vibrational Frequencies

For the anharmonic frequency calculation of the CO modes, there are only three active modes are chosen, i.e. the degenerate E_1 modes (2014 cm^{-1}) and higher intensity B_2 mode (2045 cm^{-1}) to be treated explicitly. The PES calculations have been performed using DFT/BP86 with TZVP basis set as implemented in Gaussian 03 [180]. The PES is that expressed in terms of normal mode coordinates, i.e $V(\mathbf{Q}, \mathbf{q})$. Thereby, the two E_1 degenerate modes as well as B_2 mode are treated beyond harmonic approximation. These three modes ($\mathbf{Q} = (Q_1, Q_2, Q_3)$) have been separated from the remaining $3N - 9$ harmonic bath modes $\mathbf{q}$. The coupling $V_c(\mathbf{Q}, \mathbf{q})$ is modeled in linear order with respect to $\mathbf{q}$. There is no contribution from global rotation of the molecule so the molecular

Table 4.2 *Calculated harmonic vibrational frequencies (cm^{-1}), their infrared intensities (km/mol) and the experimental values for active CO modes, [a]Reference [124], [b]Reference [125] and [b]Reference [192]. All E modes are doubly degenerate.*

Symmetry	Frequency	Intensity	Expt
A$_1$	149	0	
A$_1$	1999	0	
A$_1$	2106	0	
A$_1$	425	0	
A$_1$	499	0	
A$_1$	695	0	
A$_1$	97	0	
A$_2$	380	0	
B$_1$	381	0	
B$_1$	47	0	
B$_2$	118	3	
B$_2$	1988	788	(1983)[a] (1992)[b] (1983)[c]
B$_2$	2045	1348	(2045)[a] (2053)[b] (2044)[c]
B$_2$	420	15	
B$_2$	491	1	
B$_2$	673	590	
E$_1$	107	1	
E$_1$	2014	2224	(2014)[a] (2025)[b] (2014)[c]
E$_1$	420	0	
E$_1$	484	18	
E$_1$	55	0	
E$_1$	563	0	
E$_1$	669	189	
E$_1$	99	0	
E$_2$	2016	0	
E$_2$	428	0	
E$_2$	469	0	
E$_2$	555	0	
E$_2$	68	0	
E$_2$	99	0	
E$_3$	108	0	
E$_3$	1981	0	
E$_3$	402	0	
E$_3$	482	0	
E$_3$	551	0	
E$_3$	57	0	
E$_3$	666	0	
E$_3$	84	0	
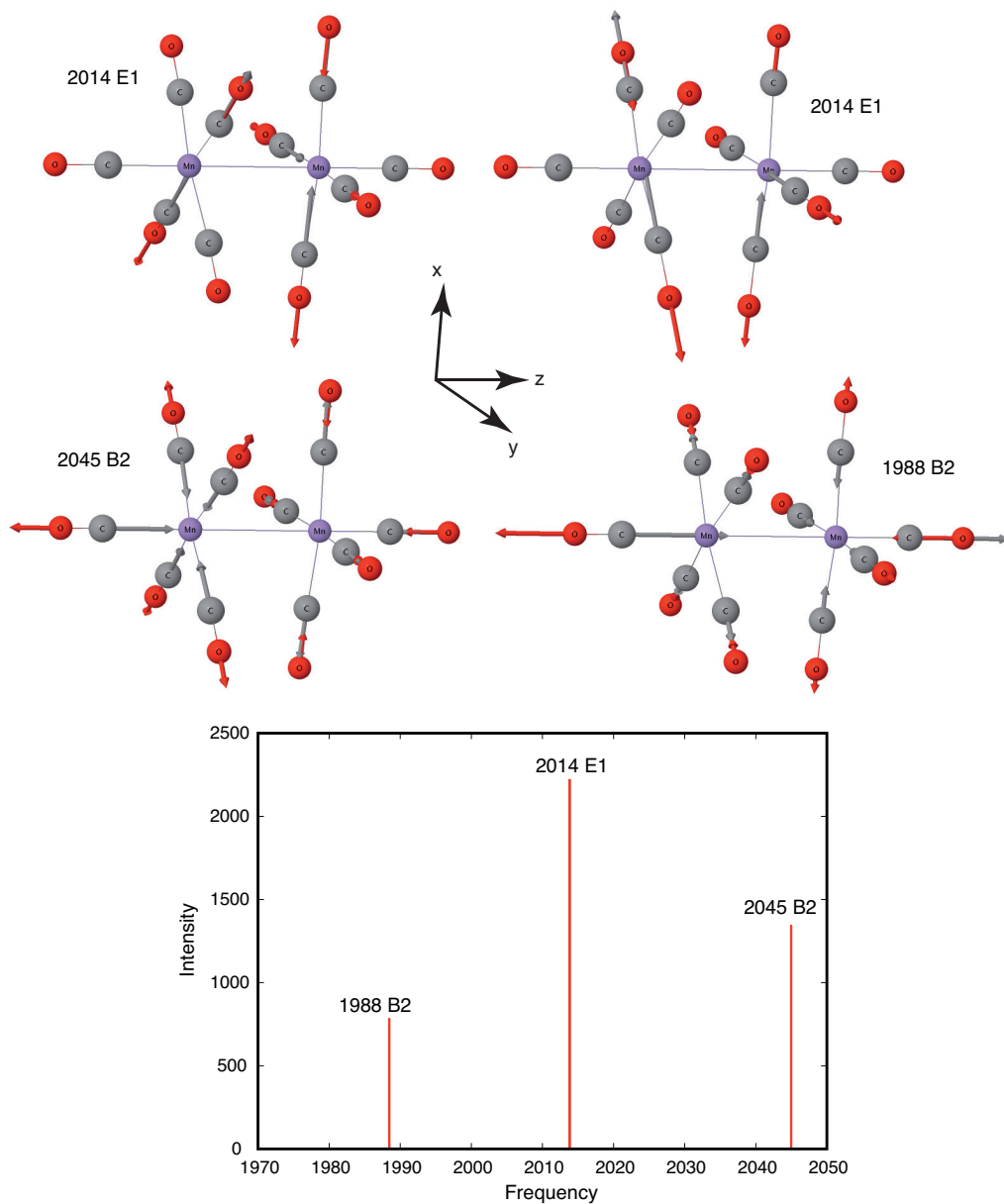
Fig. 4.2 *Active CO normal mode displacement vectors of $Mn_2(CO)_{10}$ of D_{4d} point group symmetry and the calculated IR-line spectrum using the BP86/TZVP level of theory.*

Hamiltonian is,

$$H_{mol} = H_{\mathbf{Q}} + H_{\mathbf{q}} + V_c(\mathbf{Q}, \mathbf{q}) \tag{4.1}$$

with the part describing the anharmonic coordinates (explicitly treated modes)

$$H_{\mathbf{Q}} = T_{\mathbf{Q}} + V(\mathbf{Q}, \mathbf{q} = 0) \tag{4.2}$$
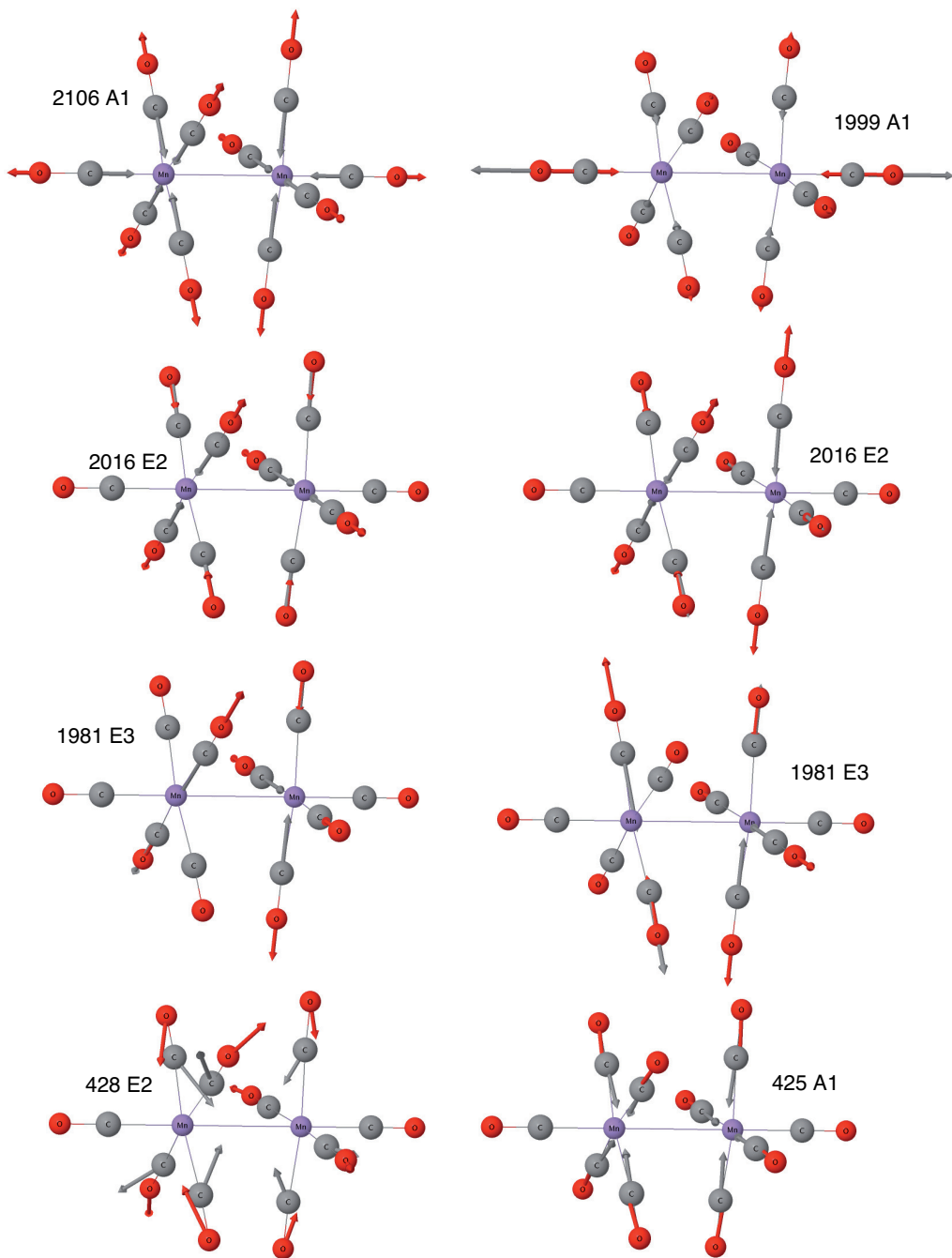
Fig. 4.3 *Displacement vectors of some selected modes, remaining CO modes and two of low frequency modes of $Mn_2(CO)_{10}$ in D_{4d} point group symmetry obtained using the BP86/TZVP level of theory.*

the harmonic part (bath modes)

$$H_{\mathbf{q}} = \frac{1}{2} \sum_i \left(p_1^2 + \omega_i^2 q_i^2 \right) \tag{4.3}$$

and the interaction (coupling) part

$$V_c(\mathbf{Q}, \mathbf{q}) = \left. \frac{\partial V(\mathbf{Q}, \mathbf{q})}{\partial \mathbf{q}} \right|_{\mathbf{q}=0} \mathbf{q} = -\mathbf{F}(\mathbf{Q})\mathbf{q} \tag{4.4}$$

The total Hamiltonian is given by Eq. 2.39. The forces $\mathbf{F}(\mathbf{Q})$ have been used to select the subset of harmonic (bath) modes for the model. Actually in this case the 3D PES is extended to a 10D PES by including the rest of all CO modes, as bath modes (see Fig. 4.3). Since we are in the vicinity of minimum, these bath modes are treated in harmonic approximation as mentioned in the theoretical part. A proper way for choosing the bath modes is the calculation of the reorganization energy. Here and in the next section, the reorganization energy of bath modes has been measured using Eq. 2.47 assuming the frequency does not change.

Furthermore, the dipole moment surface, $\boldsymbol{\mu}(Q_1, Q_2, Q_3)$, has been computed at the DFT level of theory as the PES for the three vectors components, $\boldsymbol{\mu} = (\mu_x, \mu_y, \mu_z)$. In addition, the linear dipole approximation for the bath modes was assumed.

The IR-spectrum is obtained by Fourier-transform of the dipole-dipole autocorrelation function given by Eq. 2.72 [108]. Neglecting the prefactors, this equation becomes

$$\alpha(\omega) = \omega \sum_{a=x,y,z} \int_0^\infty \mathrm{d}t\, e^{i\omega t - \gamma t} \left\langle \Psi(0) | \boldsymbol{\mu}_a(t) \boldsymbol{\mu}_a | \Psi(0) \right\rangle. \tag{4.5}$$

Where, $\langle \Psi_0 |$ is the ground state which was determined by imaginary time propagation as described in Ref. [162] and γ is a parameter that is introduced to cut-off the integral.
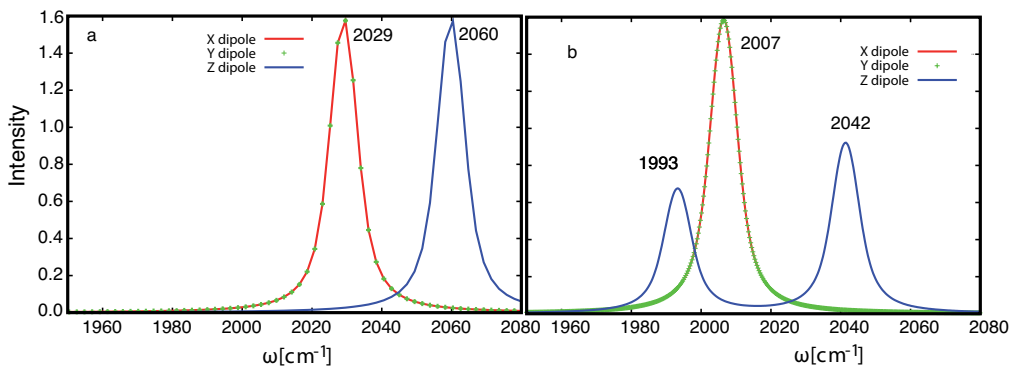
Fig. 4.4 *Anharmonic spectra for CO vibrations for 3D (a) and for 10D (b). These spectra are obtained using Eq. 4.5 using a propagation time for 3 ps and the damping factor $\gamma = 1.5$ ps .*

Numerical Implementation

The 10D wave function $\Psi(\mathbf{Q}, \mathbf{q}; t)$ is represented on a grid in terms of a harmonic oscillator discrete variable representation. With (11 points within $[-1.4 : 1.4]\, a_0$ (a.m.u.)$^{1/2}$) for the explicitly treated modes $\mathbf{Q}$ as well as the bath modes (remaining CO modes) $\mathbf{q}$. The actual propagation is performed using the constant mean field CMF scheme with an initial step size of 1 fs and an error tolerance of 10^{-8} in combination with BS/SPFs with integration order of 10 and error tolerance of 10^{-8} and SIL with integration order of 40 and error tolerance of 10^{-8}. Five single particle functions (SPF) are used per explicitly

Table 4.3 *Most important bath modes according the averaged reorganization energy $\langle E^{(\text{reorg})} \rangle$ (average over the full $\mathbf{Q}$ grid. The parameters of the MCTDH implementation (N_{DVR}: number of DVR points, N_{SPF}: number of single particle functions) are given as well. Notice that modes q_2 and q_5 as well as q_3 and q_4 have been combined. Dipole gradient for the bath modes are given in Debye*

mode	ω_i (cm^{-1})	$\langle E^{(\text{reorg})} \rangle$ (cm^{-1})	grid $(a_0(\text{a.m.u.})^{1/2})$	N_{DVR}	N_{SPF}	Dipole Gradient
q_1 (E$_3$)	1981	2045.25	-1.4:1.4	11	4	-0.0076 in x
q_2 (E$_3$)	1981	2045.25	-1.4:1.4	11	4	-0.0076 in y
q_3 (B$_2$)	1988	98.2852	-1.4:1.4	11	4	-1.1415 in z
q_4 (A$_1$)	1999	361.823	-1.4:1.4	11	4	-0.0058 in z
q_5 (E$_2$)	2016	1036.89	-1.4:1.4	11	4	0.0000
q_6 (E$_2$)	2016	1177.16	-1.4:1.4	11	4	0.0000
q_7 (A$_1$)	2106	5675.46	-1.4:1.4	11	5	0.0034 in z

treated coordinates Q_1 and Q_2 (combined together) for E$_1$ degenerate modes. And, 5 SPFs for the other active mode (B$_2$). The parameters for the bath modes are combined in Table 4.3. The largest natural orbital populations have been typically on the order of 10^{-4}. The wave function propagation has been performed using the MCTDH method [163] as implemented in the Heidelberg program package [160]. The reorganization energy for the bath modes over the whole grid points is calculated using Eq. 2.47 for the bath modes and is presented in Table 4.3.

The anharmonic CO vibrational spectra for 3D and 10D are introduced in Fig. 4.4 (a) and (b), respectively. For the parameters see the Figure caption. The anharmonic CO vibration spectra are calculated by Fourier-transform of the dipole-dipole autocorrelation function of the propagated wavepacket. As shown from 3D spectrum in panel (a), the position of peaks are blue shifted ~ 20 cm^{-1} from the experimental spectra. Moreover, the missing of the peak which is at 1988 cm^{-1} and the intensity ratio between these vibrations are not in agreement with the experimental spectra. Extending this 3D PES to 10D PES including the other CO vibrations gave the spectrum which is presented in panel (b). This spectra shows a good agreement with the experimental results with respect to the position and intensity of the peaks. At the end, there is a coupling between the active CO modes and the other CO modes which can not be neglected.

4.5   Model Hamiltonian for Wavepacket Circulation

Which is interesting for the vibrational spectra of Mn$_2$(CO)$_{10}$ molecule is the degenerate E$_1$ active modes which could be excited with polarized laser pulses. Here, CPL will be used to excite these E$_1$ degenerate CO modes in order achieve pseudorotation of the molecule around its principal axis. So in this section we will deal with different potential model from the previous section. The potential energy surface for this task has also been expressed in terms of normal mode coordinates as the previous section i.e. $V(\mathbf{Q}, \mathbf{q})$. But, $\mathbf{Q}$ here are the two E$_1$ degenerate modes i.e $(\mathbf{Q} = (Q_1, Q_2))$ which are treated explicitly i.e. beyond the harmonic approximation. The bath modes $\mathbf{q}$, are the rest of the modes that could couple with the active displaced modes. The Hamiltonian parameters are as in the previous case and can be described by Eq. 4.1 to Eq. 4.4.

The molecular Hamiltonian is supplemented by the interaction field Hamiltonian

which is described in dipole approximation, (see Eq. 2.54)

$$H_{field}(t) = -\boldsymbol{\mu}\left(\mathbf{Q}\right)\mathbf{E}(t) \tag{4.6}$$

Here, $\boldsymbol{\mu}\left(Q_1, Q_2\right)$ is the dipole moment surface for different polarization direction $\boldsymbol{\mu} = (\mu_x, \mu_y)$ since these E_1 degenerate modes are polarized only in x- and y-direction and there is no polarization in z-direction. It has been obtained along with the PES for the explicitly treaded modes $\mathbf{Q}$ using DFT (BP86/TZVP) level of theory. In this case there is no coupling to the other two active B_2 modes because they are polarized in z-direction. For the dynamics simulation it will be assumed that the molecule has been pre-oriented with the coordinate system as presented in Fig. 4.1 (for an overview on field-driven pre-orientation, see Ref. [193]). Circularly polarized laser field as introduced in Eq. 2.83 is used to excite the ground state wavepacket. The laser field will be taken to be of the form

$$
\begin{aligned}
\mathbf{E}(t) &= \left(\begin{array}{c} E_x(t) \\ E_y(t) \\ 0 \end{array} \right) \\
&= E_0 \Theta(t)\Theta(t_{\mathrm{p}} - t)\sin^2(t\pi/t_{\mathrm{p}}) \left(\begin{array}{c} \cos(\omega t) \\ \sin(\omega t) \\ 0 \end{array} \right).
\end{aligned} \tag{4.7}
$$

i.e. the field is right-polarized and assumed to propagate along the z-direction.

Here t_{p} is the total pulse duration, ω is the carrier frequency, and E_0 is the field strength. These parameters will be chosen such as to achieve the excitation of a vibrational superposition state with respect to the two E_1 modes, which corresponds to a wave packet performing a clockwise circulation on the potential energy surface $V(\mathbf{Q}, \mathbf{q} = 0)$, if viewed along the propagation direction of the field. The respective normal mode displacements are shown in Fig. 4.5. Close inspection of this figure shows that during this circulation, the antisymmetric combination of stretching motions of equatorial CO groups which are opposite to each other "moves" around the symmetry (z) axis. Of course, this classical picture applies only as long as the wave packet stays compact and an important question to be addressed will be the regime of validity of this classical analogue.

In this case the PES is extended to be a 7D PES. Two explicitly treated modes $\mathbf{Q}$ and five bath modes $\mathbf{q}$. The bath modes have been selected according the value of the force in Eq. 4.4 $\mathbf{F}(\mathbf{Q})$ exerted on the coupled modes $\mathbf{q}$. In other words, the bath modes have been selected according to their coupling to the explicitly treated displaced modes. The reorganization energy of the bath modes is a convenient measure for the $\mathbf{F}(\mathbf{Q})$. Reorganization energy is the energy which is required to return the oscillators back to their equilibrium position and it is a function of the active mode displacements. So, the average of the reorganization energy over the PES has been considered to select the most important bath modes, taking into account that this average is compared to the original frequency of the oscillator. All the selected bath modes with the reorganization energies as well as the original frequency value of the vibrational modes are combined in Table 4.4. The displacement vectors for the low frequency mode A_1 is presented in Fig. 4.3.

Numerical Implementation

The 7D time-dependent Schrödinger equation,

$$i\hbar\frac{\partial}{\partial t}\Psi(\mathbf{Q}, \mathbf{q}; t) = (H_{mol} + H_{field}(t))\Psi(\mathbf{Q}, \mathbf{q}; t) \tag{4.8}$$

Table 4.4 *Most important bath modes according the averaged reorganization energy $\langle E^{(\mathrm{reorg})}\rangle$ (average over the full **Q** grid and - in parentheses - over a reduced grid from -1 to 1 $a_0\,(\mathrm{a.m.u.})^{1/2}$). The parameters of the MCTDH implementation (N_{DVR}: number of DVR points, N_{SPF}: number of single particle functions) are given as well. Notice that modes q_2 and q_5 as well as q_3 and q_4 have been combined. Dipole gradient of the low frequency mode is 0.01 Debye in z-direction.*

mode	ω_i (cm^{-1})	$\langle E^{(\mathrm{reorg})}\rangle$ (cm^{-1})	grid ($a_0(\mathrm{a.m.u.})^{1/2}$)	N_{DVR}	N_{SPF}
q_1 (A$_1$)	425	468 (72)	-7.5:7.5	45	10
q_2 (A$_1$)	1999	822 (122)	-1.7:1.7	25	10
q_3 (E$_2$)	2016	1426 (204)	-1.7:1.7	25	10
q_4 (E$_2$)	2016	1649 (239)	-1.7:1.7	25	10
q_5 (A$_1$)	2106	4646 (692)	-1.7:1.7	25	10

has been solved using the MCTDH method [163] as implemented in the Heidelberg program package [160]. The seven-dimensional wave function $\Psi(\mathbf{Q}, \mathbf{q}; t)$ is represented on a grid in terms of a harmonic oscillator discrete variable representation (DVR). A total of 25 DVR points on the grid $[-1.7 : 1.7]\,a_0$ (a.m.u.)$^{1/2}$ together with 12 single particle functions (SPFs) are used for each of the **Q** modes which are treated as a combined MCTDH particle. The parameters for the bath modes are compiled in Table 4.4. Potential energy and dipole moment surfaces have been fitted on this grid using the POTFIT algorithm. [156] Using this set of SPFs the natural orbital populations have been below 10^{-5}. The actual propagation is performed using the variable mean field scheme with a 6th order Adams-Bashforth-Moulton integrator. The vibrational ground state, $|\Psi_0\rangle$, has been calculated using the improved relaxation scheme [164]; some uncoupled (one-dimensional zero-order) states in the **Q**-subspace will be used for the discussion of the dynamics.

In the following we will present results for the time-dependent wave packet dynamics which have been obtained for a carrier frequency ω, fixed to the fundamental harmonic transition of the E_1 modes, which is at 2014 cm^{-1}. The total propagation time has been set to 5 ps. First, we will discuss the effect of changing the field strength E_0, before the variation of the pulse length is addressed. A global analysis of the dynamics will be given in terms of the following quantities: (i) the energy absorbed by the molecule at the end of the pulse: $\Delta E_{\mathrm{mol}} = \langle\Psi(t_\mathrm{p})|H_{\mathrm{mol}}|\Psi(t_\mathrm{p})\rangle - \langle\Psi_0|H_{\mathrm{mol}}|\Psi_0\rangle$, (ii) the maximum energy change of the bath modes reached during the considered time interval of 5 ps: $\Delta E_{\mathrm{bath}}^{(\mathrm{max})} = \max(\langle\Psi(t)|H_{\mathbf{q}}|\Psi(t)\rangle - \langle\Psi_0|H_{\mathbf{q}}|\Psi_0\rangle)$, (iii) the maximum expectation value of the E_1 modes' coordinate operators during the 5 ps time interval: $Q^{(\mathrm{max})} = \max(\langle\Psi(t)|\mathbf{Q}|\Psi(t)\rangle)$, (iv) the population of the ground state at the end of the pulse: $P_0 = |\langle\Psi(t_\mathrm{p})|\Psi_0\rangle|^2$ and (v) the mean radius of the circulating wave packet in the space of the E_1 modes: $Q_\mathrm{r}(t) = (\langle\Psi(t)|(Q_1^2 + Q_2^2)|\Psi(t)\rangle)^{1/2}$.

4.5.1   Dependence on the Field Strength

A global analysis of the dynamics in dependence on the field strength and for a pulse duration of $t_\mathrm{p} = 500$ fs is given in Table 4.5. Overall, we observe a monotonous decrease of the ground state population P_0 with increasing field amplitude. For the highest amplitude used, the ground state is completely depopulated. At the same time the absorbed energy ΔE_{mol} increases, indicating vibrational ladder climbing. In fact for $E_0 = 1.5$ mE$_\mathrm{h}/ea_0$ the absorbed energy is compatible with an appreciable simultaneous population of the third vibrationally excited state in each of the two **Q** modes. Analysis of the population
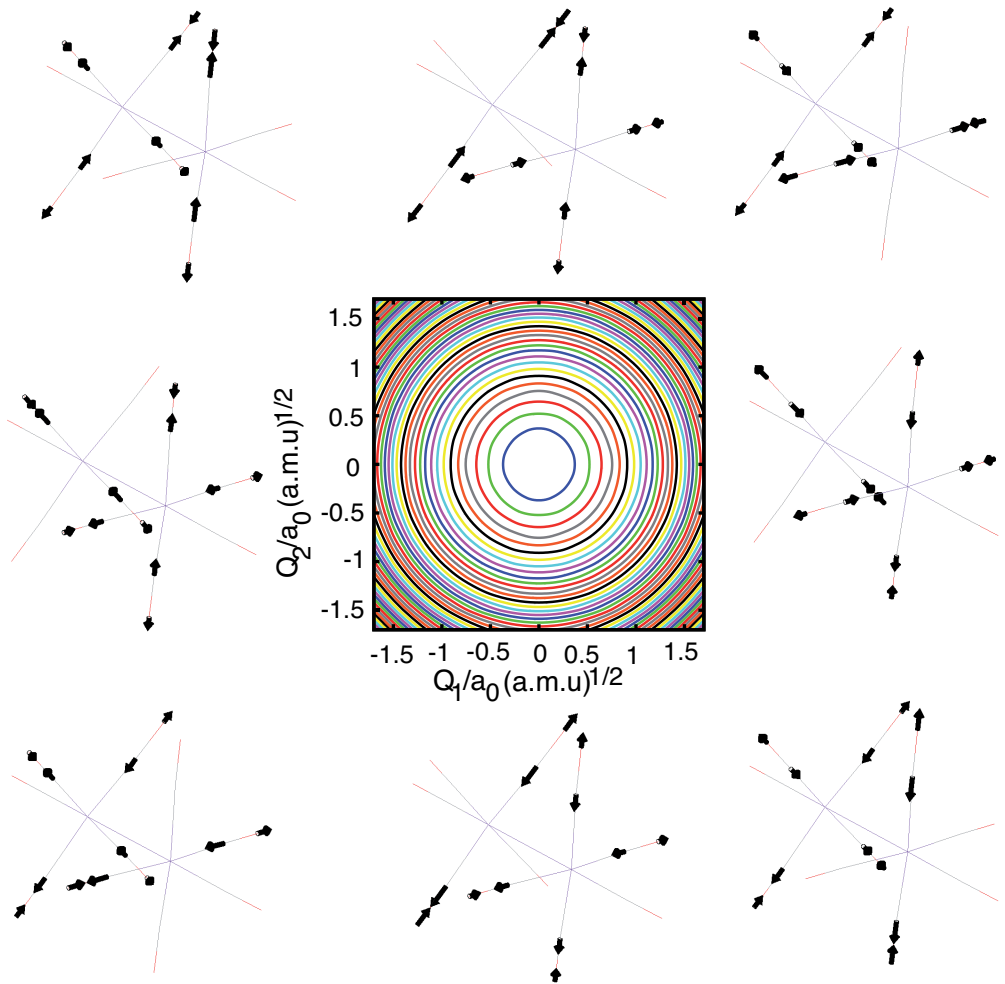
Fig. 4.5 *Classical picture of vibrational wave packet circulation triggered by excitation of the two degenerate E_1 modes by means of a circularly polarized laser field. Shown are the displacement vectors for the superposition of the modes along a unit circle in steps of 45°. In the central panel the two-dimensional potential $V(\mathbf{Q}, \mathbf{q} = 0)$ is shown (contour lines in steps of 2000 cm^{-1} starting at 2000 cm^{-1}).*

shows that in fact many overtone and combination transitions are excited with the ($\nu_1 = 2, \nu_2 = 2$) state having the largest population.

The anharmonic coupling to the bath modes will increase along with the absorbed energy, i.e. if the wave packet explores configurations away from equilibrium. For moderate excitation conditions the extent of anharmonic coupling is rather small, e.g. if the amount of absorbed energy corresponds to about one quantum of excitation in a CO mode ($E_0 = 0.5$ mE$_h$/ea_0) we find $\Delta E_{\mathrm{mol}}/\Delta E_{\mathrm{bath}}^{(\mathrm{max})} \approx 5$. The effect of the bath becomes appreciable only under high excitation conditions, e.g., for $E_0 = 1.5$ mE$_h$/ea_0 we find $\Delta E_{\mathrm{mol}}/\Delta E_{\mathrm{bath}}^{(\mathrm{max})} \approx 2.8$.

In Fig. 4.6 we show the expectation values of the Hamiltonian operators for the system modes, $H_{\mathbf{Q}}$, the uncoupled bath modes, $H_{\mathbf{q}}$ and the sum over uncoupled bath modes, $H_{\mathbf{q}}$, for two field strengths. As expected the energy of the $\mathbf{Q}$ modes rises during laser
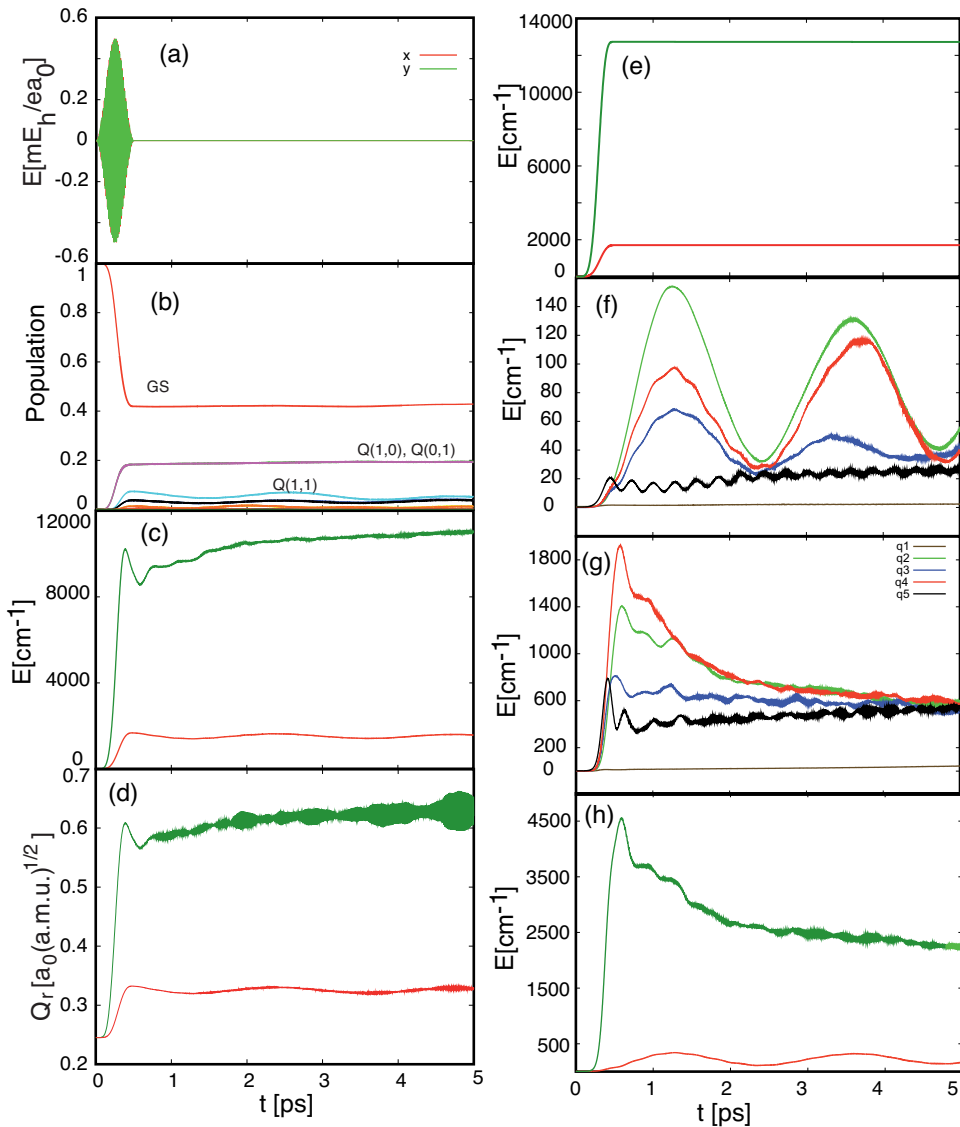
Fig. 4.6 *CPL in x- and y- directions (a) and Populations of the ground states and some other uncoupled (one-dimensional zero-order) states (b) for t_p=500 fs and $E_0 = 0.5$ mE$_h$/ea$_0$. (c) Expectation values of $H_\mathbf{Q}$ for a 500 fs excitation with field strength $E_0 = 0.5$ mE$_h$/ea$_0$ (lower curve) and 1.5 mE$_h$/ea$_0$ (upper curve). Time-dependence of the expectation value of the radius of circulation $Q_r(t)$ for the two cases considered in panel (c) (upper curve: $E_0 = 1.5$ mE$_h$/ea$_0$, lower curve: $E_0 = 0.5$ mE$_h$/ea$_0$) is presented in panel (d). The free field Hamiltonian (H_0) for a 500 fs excitation with field strength $E_0 = 0.5$ mE$_h$/ea$_0$ (lower curve) and 1.5 mE$_h$/ea$_0$ (upper curve) (e). The respective expectation values of $H_\mathbf{q}$ for the five bath modes are shown in panels (f) ($E_0 = 0.5$ mE$_h$/ea$_0$) and (g) ($E_0 = 1.5$ mE$_h$/ea$_0$). With increasing energy at about 1000 fs the curves correspond to q_1, q_5, q_3, q_2, and q_4 in panel (g), whereas in panel (f) q_2 and q_4 are interchanged (see also key in panel (g)). The sum of the expectation values of $H_\mathbf{q}$ for the five bath modes are shown in panels (h) for the same time durations t_p=500 fs, $E_0 = 0.5$ mE$_h$/ea$_0$ (lower curve) and 1.5 mE$_h$/ea$_0$ (upper curve).*

pulse excitation ($t_{\mathrm{p}} = 500$ fs) as seen in panel (c). For the lower field strength the expectation value subsequently oscillates around the attained value signaling reversible energy exchange with the bath modes. Indeed the corresponding oscillations in the bath mode energies are seen in panel (f). Increasing the field strength, the energy exchange with the bath is more pronounced and instead of regular oscillations the onset of equilibration among the bath modes is observed in panel (g). The sum over the bath modes is presented in panel (h). It is shown that the energy exchange between the system modes, $H_{\mathbf{Q}}$ and the bath modes, $H_{\mathbf{q}}$ is more pronounced for the high field strength (upper curve). For medium field strength (lower curve), the energy exchange is oscillating, starting to increase in the beginning of the field, at 2.5 ps and around 5 ps.

The populations of the ground state and some uncoupled states are introduced in Fig. 4.6 (b) for the medium field strength, The ground state population reaches ≈ 40 %. The other uncoupled states have been populated in such away that confirms the ladder climbing where the $(0, 1)$ and $(0, 1)$ are populated first 20%, $(1, 1)$ is populated 8% and then $(2, 0)$ and $(0, 2)$ are populated 4 %. Still there is no appreciable coupling to lower frequency modes that could lead to an energy flow out of the selected $\mathbf{Q}$ modes. We notice from panels (f) and (g) that the low-frequency mode q_1, which was selected because it had the largest reorganization energy in the lower-frequency part of the spectrum is not appreciably excited. Of course, this could be partly due to the simplified treatment of anharmonic coupling in the present model. Nonlinear terms in the bath mode coordinate as well as mixed contributions from several low-frequency bath modes could lead to a resonant relaxation channel for the high-frequency modes. Finally, we comment on the initial partitioning of energy among the bath modes. Inspecting Table 4.4 one might have anticipated that mode q_5 will dominate the bath dynamics. However, the fundamental frequency of the laser-excited $\mathbf{Q}$ modes is 2014 cm^{-1}, which is resonant to $q_2 - q_4$, but rather off-resonant with respect to q_5. Hence, energy exchange between the $\mathbf{Q}$ and the q_5 modes is not very efficient.

Table 4.5 *Analysis of the laser-driven wave packet dynamics for a 500 fs pulse which is resonant to the fundamental transition of the E_1 modes (cf. Eq. (4.7)).*

E_0 (mE$_{\mathrm{h}}$/ea_0)	ΔE_{mol} (cm^{-1})	$\Delta E_{\mathrm{bath}}^{(\mathrm{max})}$ (cm^{-1})	$Q^{(\mathrm{max})}$ ($a_0\sqrt{\text{a.m.u}}$)	P_0
0.1	71	6	0.05	0.97
0.2	277	18	0.09	0.87
0.3	621	62	0.13	0.73
0.4	1099	164	0.18	0.57
0.5	1708	341	0.22	0.42
1.5	12733	4553	0.50	0.00

The focus of the present investigation is on the wave packet circulation with respect to the E_1 modes. Inspecting Table 4.5 we notice that the maximum bond elongation increases with the amount of absorbed energy. The value that is reached can be compared, e.g., with the variance of the ground state coordinate distribution which is 0.17 $a_0\sqrt{\text{a.m.u}}$ for the $\mathbf{Q}$ modes. Thus for the largest field strength we observe that the bond elongation is about three times this ground state variance. A more detailed picture is provided by inspecting the coordinate operator expectation values, $Q_i(t) = \langle \Psi(t)|Q_i|\Psi(t)\rangle$, which are shown in Fig. 4.7. In the parametric plot the expectation values trace a clockwise (if viewed along the propagation direction of the field) circulating trajectory on the potential $V(\mathbf{Q}, \mathbf{q} = \mathbf{0})$. For small field strengths the amplitude of this circulation increases during the excitation period of 500 fs (a) and (b) panels of Fig. 4.7. For the strongest field used

(c) panel of Fig. 4.7, the amplitude of the circulation starts to decrease already during the interaction with the pulse. Furthermore, after the excitation pulse is over the behavior shows a strong dependence on the field amplitude (right column of (a), (b) and (c) panels of Fig. 4.7). IJudging from the amount of energy redistribution given in Table 4.5 the decrease of $Q_i(t)$ can only in part be an effect of the anharmonic coupling to the bath. Instead it is the wave packet dispersion that is mostly responsible for this decrease of $Q_i(t)$. This is shown in Fig. 4.7 (g) where snapshots of the reduced density are plotted for the case of $E_0 = 0.5$ mE$_\mathrm{h}/ea_0$. One notices that the wave packet stays compact in the excitation period only, but then starts to disperse. Eventually, the wave packet is rather delocalized even though it is still circulating. However, due to the delocalization negative and positive coordinate values contribute to the expectation values along the **Q** axes and therefore the expectation values become smaller and cannot reflect the wave packet circulation anymore. With increasing excitation more eigenstates contribute to the wave packet such that the dispersion effect becomes more pronounced and sets in already during the pulse.

A quantity which will reflect the wave packet circulation even in situations where the latter becomes delocalized is the mean radius $Q_\mathrm{r}(t)$, which is shown in Fig. 4.6 (d) for the two cases of Fig. 4.6 (c). Clearly, after the excitation pulse is over $Q_\mathrm{r}(t)$ stays approximately constant in the considered time interval. The non-vanishing $Q_\mathrm{r}(t)$ implies that there will a nuclear ring current inducing a magnetic field. [194]

4.5.2   Dependence on the Pulse Duration

In the following the dependence of the laser-driven wave packet dynamics on the duration of the excitation pulse has been investigated. As a reference case we have used $t_\mathrm{p} = 500$ fs and $E_0 = 0.5$ mE$_\mathrm{h}/ea_0$. For a given duration t_p the field amplitudes have been chosen such as to keep the integrated field envelope at the same value as in the reference case. Note that we are not dealing with a two level system and that the pulses are no π-pulses. The pulse parameters are summarized in Table 4.6.

Table 4.6   *Analysis of the laser-driven wave packet dynamics for pulses of different duration and amplitude. The integrated field envelope is identical in all cases.*

| t_p | E_0 | ΔE_mol | $\Delta E_\mathrm{bath}^{(\mathrm{max})}$ | $Q^{(\mathrm{max})}$ | P_0 |
(fs)	(mE$_\mathrm{h}/ea_0$)	(cm^{-1})	(cm^{-1})	($a_0\sqrt{\mathrm{a.m.u}}$)	
100	2.5	1812	374	0.23	0.40
500	0.5	1708	341	0.22	0.42
1000	0.25	1441	273	0.20	0.47
1500	0.17	1146	205	0.18	0.54

Table 4.6 also contains the various expectation values, which give a global characterization of the dynamics. First, we notice that the different pulse durations give comparable depopulations of the vibrational ground state between 40 and 54%. The amount of energy absorbed by the molecule decreases with the pulse duration and is largest for the shortest pulse ($t_\mathrm{p} = 100$ fs), although the difference to the reference pulse is only 6%. At the same time the excitation of bath modes decreases from a contribution to the total energy of 21% for $t_\mathrm{p} = 100$ fs down to 18% for $t_\mathrm{p} = 1500$. Moreover, the maximum radius of circulation of the expectation value of the **Q** coordinates is reduced slightly. Inspecting the time dependence of the $Q_i(t)$ in Fig. 4.7 (d), (e) and (f), it is noticed that again there is an initial period, where the wave packet stays rather compact such that the coordinate expectation values give a reasonable picture of the moving wave packet. This
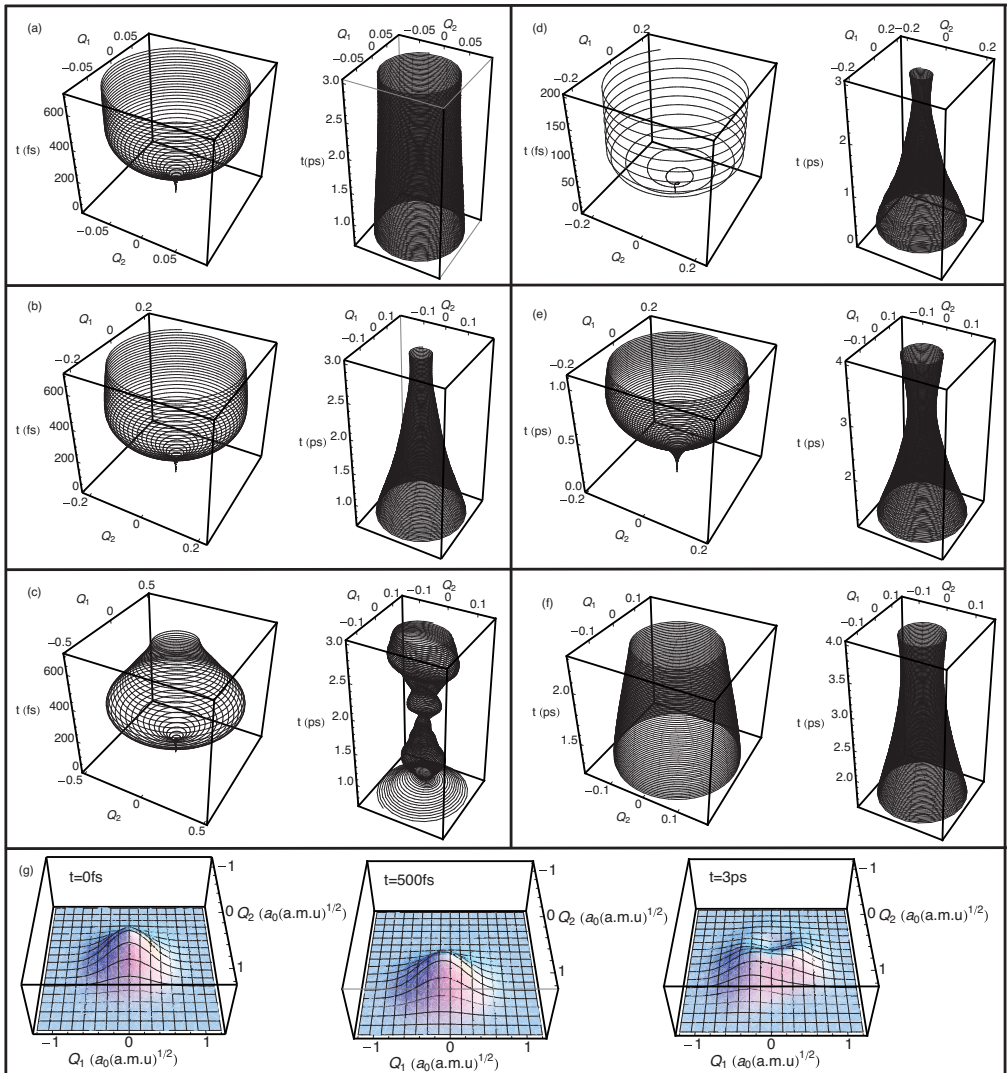
Fig. 4.7 *Parametric plots of (Q_1, Q_2) (in $a_0\sqrt{\text{a.m.u}}$) for a 500 fs laser pulse excitation and a field strength E_0 (in mE_h/ea_0) of 0.2 (a), 0.5 (b) and 1.5 (c). (Notice the different axes scales). Parametric plots of (Q_1, Q_2) (in $a_0\sqrt{\text{a.m.u}}$) for different pulse durations. Panel (d): $t_p = 100$ fs, $E_0 = 2.5$ mE_h/ea_0, Panel (e): $t_p = 1000$ fs, $E_0 = 0.25$ mE_h/ea_0, Panel (e): $t_p = 1500$ fs, $E_0 = 0.17$ mE_h/ea_0. (Notice the different axes scales). Panel (g) are snapshots of the time evolution of the reduced density with respect to the $\mathbf{Q}$ modes for laser-driving with a pulse having the parameters $t_p = 500$ fs, $E_0 = 0.5$ mE_h/ea_0, and $\omega/2\pi c = 2014$ cm^{-1}.*

is followed by a period where the wave packet disperses such that the dynamics cannot be understood from the expectation values. As far as the pulse duration dependence is concerned the most striking observation from Fig. 4.7 (d), (e) and (f), is that the time span of compact wave packet propagation can be prolongated by increasing the parameter t_p. In passing it is noted that this does also imply that the time span of circulation at about the full radius is longer, but of course not identical to t_p. For $t_p = 500$ fs and 1500 fs the expectation values $Q_i(t)$ are within 90% of their maximum value during the interval $[450 : 800]$ fs and $[950 : 1650]$ fs, respectively. Since the anharmonic coupling is still small in the considered range of the potential energy surface corresponding to about one to two quanta of excitation of the E_1 modes, intramolecular energy redistribution doesn't destroy wave packet circulation even for the longest pulse duration of 1.5 ps and subsequent 3.5 ps free evolution.

4.6   Two-Dimensional Dissociative PES

In this molecule there are two channels for Mn-CO bond breaking, namely of the equatorial or axial CO. For describing Mn-CO bond breaking, one needs to introduce large amplitude coordinates instead of normal modes. Here, we assumed that, the delocalized CO vibrations have been superimposed to give a local vibration that could be used to describe these large amplitude coordinates (see Sec. 4.4 and Sec. 4.5). In the first step we start with a two-dimensional PES to study the quantum dynamics of bond breaking. We have done a 1D potential energy scan for moving of the CO center of mass with respect to the Mn atom using the DFT (BP86/TZVP) level of theory for both axial and equatorial CO groups. The result of this potential energy scan is introduced in Fig. 4.8. It is seen that from the energetic point of view, the equatorial CO is simpler than the axial CO to be removed since the electronic binding energy barrier for equatorial and axial CO is 46 kcal/mol and 55 kcal/mol, respectively.

Since only the CO vibration can be easily excited by a laser pulse one needs to introduce this coordinate into a 2D PES. Introducing R_{MCO} as the distance between the CO center of mass and Mn atom and r_{CO} as one CO bond distance (all other coordinates are frozen), then the model Hamiltonian reads

$$H = \frac{p_{MCO}^2}{2M_{CO}} + \frac{p_{CO}^2}{2\mu_{CO}} + V(R_{MCO}, r_{CO}). \qquad (4.9)$$

The quantum dynamics of this 2D model Hamiltonian will be investigated using the MCDTH method. For the numerical implementation, a harmonic oscillator discrete variable representation is used for the r_{CO} coordinate with 21 grid points and a fast Fourier transform grid is utilized for the R_{MCO} coordinate with 64 grid points. 15 SPFs are used for each coordinate. For this setup the population of the lowest natural orbitals were below 10^{-6}.

The IR line absorption spectrum has been obtained for the 2D model Hamiltonian for both axial and equatorial CO displacement. For this purpose, the dipole moment surface has been calculated in line with the PES as a function of the two coordinates. The PES and the dipole moment surface have been obtained using DFT (BP86/TZVP) level of theory. The spectrum is then obtained by Fourier transformation of dipole-dipole autocorrelation function Eq. 4.5. The obtained spectrum for both cases is shown in Fig. 4.10. It is seen from the spectra the fundamental CO stretching for both axial and equatorial are red shifted as compared with the previous calculations (see Sec.4.4). The axial CO which is polarized in z-direction is shifted to 1993 cm^{-1} as compared to the harmonic value of 2045 cm^{-1}. The equatorial CO vibration that polarized in xy-
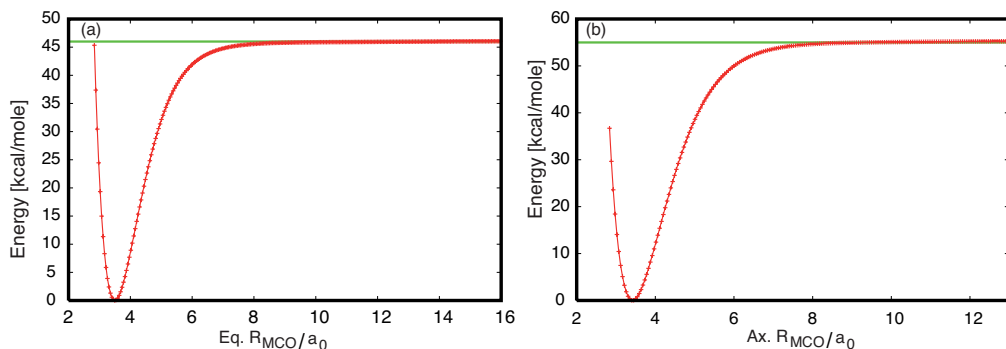
Fig. 4.8 *One dimensional PES for equatorial (a) and axial (b) CO using the DFT, BP86/TZVP level of theory. Energy is in kcal/mol and distance is in a.u. .*
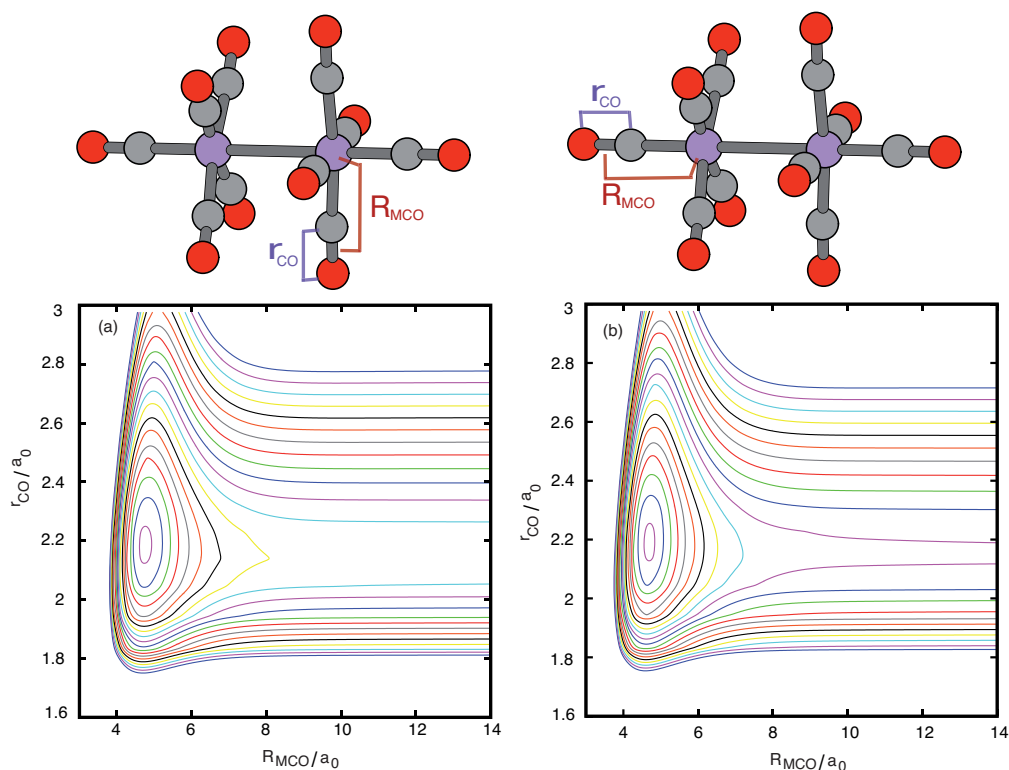
Fig. 4.9 *Two dimensional PES for equatorial (a) and axial (b) CO using the DFT, BP86/TZVP level of theory. Contours are in kcal/mol and from 2 to 120 with 6 intervals distance is in a.u..*

directions is also shifted to 1983 cm^{-1} as compared to the harmonic value of 2014 cm^{-1}. This shift is attributed to the different type of coordinates which are used in the 2D model.

In order to quantify the bond dissociation probability a step function has been defined at the exit channel of the dissociation which is at $R_{MCO} = 6.0$ a_0. The expectation value

of this step function operator is the measure of the probability in the exit channel. In the following, we are not going to use laser excitation explicitly. Instead, the ground state wavepacket has been displaced along the r_{CO} coordinate at different positions. Such displacements are corresponding to different amounts of energy that would be given to the wavepacket. We want to explore how many quanta of the fundamental CO vibration are needed to induce the bond breaking. This is a kind of approximation since this frequency has been red shifted due to the anharmonicity of the PES. The dissociation yield versus the number of quanta (fundamental CO vibration) is shown in Fig. 4.11 for both cases. It is found that the dissociation yield is very small even when the corresponding energy of the displaced ground state wavepacket is more than 15 quanta for both cases although this energy is rather high with respect to the dissociation barriers which are at about 9 quanta and 7.5 quanta for axial CO and equatorial CO, respectively.
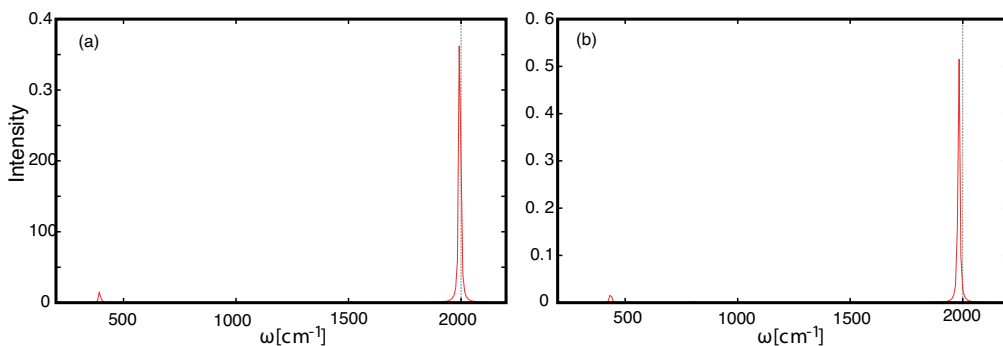

Fig. 4.10 *Linear infrared absorption spectrum for 2D model system for axial (a) and equatorial (b) CO stretching vibration. These spectra are obtained using Eq. 4.5 and propagation time of 3 ps and the damping factor $\gamma = 1.5$ ps.*

Fig. 4.11 *Reaction probability for Mn-CO bond breaking defined as the expectation value of the step function operator $\theta(R_{MCO} - 6.0a_0)$ at the end of the propagation time (2 ps) versus number of quanta. The quanta here, is the fundamental CO vibrational transition. The green vertical line is at the energy of the dissociation barrier.*

In the following we are going to discuss the quantum dynamics of the axial CO dissociation for the displacement of the wavepacket along r_{CO} coordinate that corresponds to an energy of 6.2 quanta, labeled point in Fig. 4.11 (a).

In Fig. 4.12 snapshots of the 2D wavepacket dynamics at different time durations.

Fig. 4.12 (a) is the initially displaced ground state wavepacket which is driven back to the equilibrium position (in few fs) that triggers the CO bond oscillation. The most important point here is that, the wavepacket remains localized in the region around the equilibrium distance of the center of mass coordinate (4.6442 a_0) till the end of the propagation time.

Fig. 4.12 *Wave packet dynamics of the axial 2D model potential at different time durations, $t = 0$ fs (a) (after initial displacement of the ground state wavepacket along r_{CO} coordinate to $r_{CO} = 2.6$ a_0 that corresponds to energy of 6.2 quanta of fundamental CO vibration), $t = 500$ fs (b), $t = 1000$ fs (c), $t = 1500$ fs (d), $t = 1735$ fs (e) and $t = 2000$ fs (f).*

Fig. 4.13 *Time-dependence expectation value of zero-order metal-center of mass Hamiltonian (a), expectation value for R_{MCO} coordinate (b) an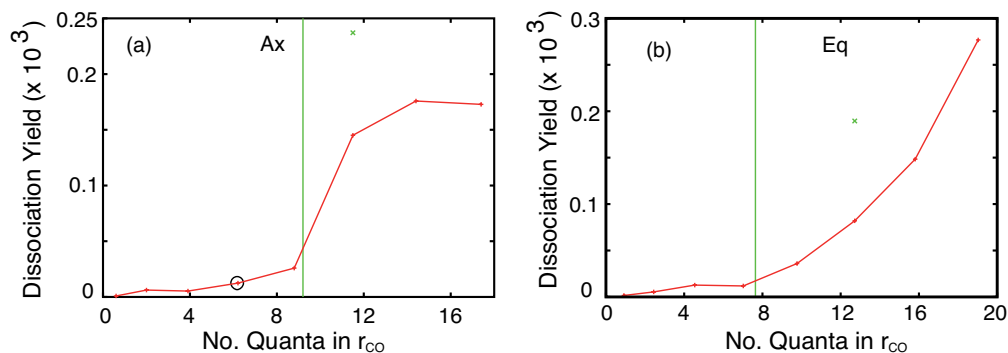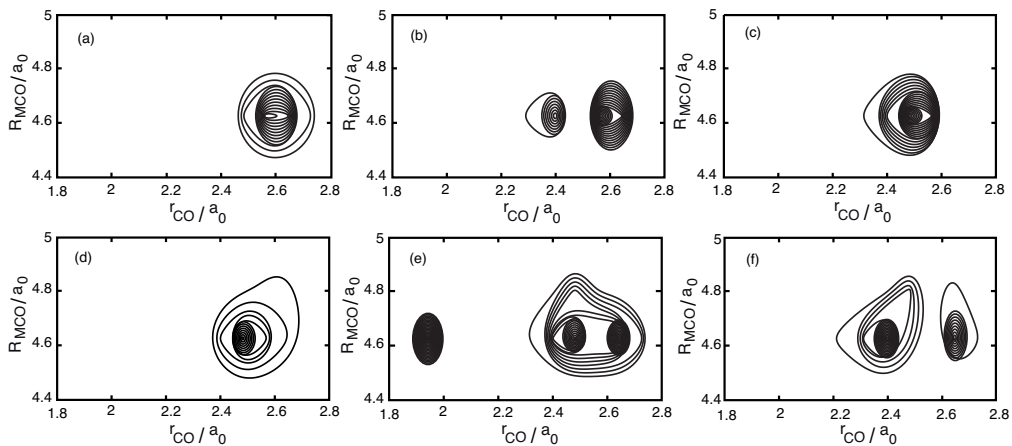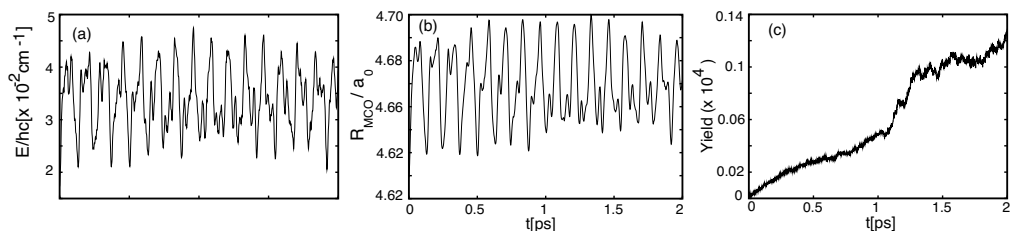d reaction probability for Mn-CO bond breaking defined as the expectation value of the step function operator $\theta(R_{MCO} - 6.0a_0)$ (c). This is for the axial CO and the displacement of the wavepacket along r_{CO} coordinate that corresponding to the energy of 6.2 quanta.*

The expectation values of the zero-order metal-center of mass $V(R_{MCO}, r_{CO} = r_{eq})$ and the R_{MCO} Hamiltonian coordinate as well as the reaction probability for Mn-CO bond breaking defined as the expectation value of the step function operator $\theta(R_{MCO} - 6.0a_0)$ are given in Fig. 4.13 (a), (b) and (c), respectively. The increase of the averaged energy of the center-of-mass motion after the first energy gain due the displacement is about 70 -100 cm^{-1} during the propagation time. So, we could expect that the bond breaking process will be of very low probability even though the amount of energy is increased beyond the energy barrier of the dissociation. This is clearly shown in Fig. 4.11 for both cases since the increase of the reaction probability is rather small. The expectation value of the R$_{MCO}$ coordinate did not show a big elongation since it

stayed around its equilibrium configuration. And, this is in line with the low dissociation yield.

One could assume that, pre-excitation of the R_{MCO} coordinate might be has some effects on the dissociation yield. Actually this is the case for the axial and equatorial CO bond breaking. That is why a small displacement along this coordinate (R_{MCO}) has been done in addition to the displacement along the r_{CO} coordinate. The results of such displacements with respect to both coordinates is introduced in the Fig. 4.11 by the green points where at that green points, both coordinates are displaced and the corresponding point in the red line is without any Mn center of mass coordinate displacement. The amount of energy gained corresponds to such R_{MCO} displacement is a bout 2.5 quanta. It has been seen an increase of the dissociation yield is noticed as a result of R_{MCO} displacement for both CO groups.

On the basis of this 2D dissociative potential for Mn-CO bond breaking, we can conclude that the reaction probability is very small. This simulation indicates that this molecule is not suited for the dissociation in the ground state!

4.7   Summary

In this chapter, the electronic structure for $Mn_2(CO)_{10}$ (optimal geometry and the harmonic frequencies) using BP86/TZVB level of theory has been studied. The results were in a good agreement with the experiments. The quantum chemistry calculations have been carried out using the symmetry restriction D_{4d} point group for the global structure. Multidimensionality of the PES is necessary to obtain the anharmonic IR spectrum. Three active modes are combined in a ten-dimensional PES (involving all carbonyl vibrations). In this case three active modes, degenerate E_1 modes and highest intensity B_2 mode are treated beyond harmonic approximations and the other seven modes (bath modes) are treated using the harmonic approximation. Fourier transformation of dipole-dipole autocorrelation function of the propagated wavepacket gives the anharmonic IR spectra.

Circularly polarized laser is used to excite the degenerate E_1 modes and to drive the wavepacket circulation of CO groups around the the principal axis. CPL have been used before by J. Manz and co-worker to obtain wavepacket circulation for small molecule like triatomic molecule (CdH$_2$)[168]. Here, a seven-dimensional PES has been used for the wavepacket circulation i.e. the two E_1 degenerate modes and five bath modes. The average reorganization energy over the whole grid points was the indicator for choosing these bath modes. The important point here is that this kind of circulation can be achieved for a polyatomic molecule for a long time (couple of picoseconds).

Two dissociative PES for axial and equatorial CO group are determined. It has been shown that reaction probability for non-statistical bond breaking is extremely small even when the gained energy via the ground state displacement is beyond the dissociation barrier.

CHAPTER 5

Summary and Outlook

In this work, laser driven DPT reactions in porphycenes and collective carbonyl vibrations in a transition metal complex ($Mn_2(CO)_{10}$) have been studied. In fact, laser control of DPT reactions has not yet received much attention. Here, a two-dimensional model which was introduced by Smedarchina and coworkers [36, 39] has been used to mimic the DPT systems. A generalization of this potential has been introduced which accounts for the asymmetry of trans and cis tautomers. Two scenarios have been studied, a high and a low barrier case which correspond to porphyrin and porphycene compounds, respectively. The Hamiltonian parameters have been obtained by fitting quantum chemistry calculations which have been carried out using DFT at the B3LYP/6-31+G(d,p) level of theory for the electronic ground state. For excited state calculation TDDFT has been used with the same level of theory. The 2D time-dependent Schrödinger equation has been solved using the MCTDH approach. Optimal control theory has been used to devise laser fields which trigger ultrafast double proton transfer. This 2D potential supports stepwise and concerted mechanisms. The optimized pulses are of (multiple) pump-dump character. Emphasizing the DPT pathways, it was found that, stepwise transfer is dominant for all cases considered. Concerted transfer has been shown to become relevant if almost degenerate pairs of states exist which are mostly localized in the reactant or product well, but can be excited simultaneously. In order to excite such a superposition state for the situation where the dipole moment changes along the asymmetric coordinate only, the states have to be of mixed character with respect to symmetric and asymmetric excitations. This situation is likely to be met for high barrier cases which support many locally excited states, that attain mixed character with increasing energy due to the anharmonicity of the potential energy surface. In such a situation a dipole change along the symmetric coordinate does not provide an additional means for concerted DPT. For low reaction barriers already fundamental excitations of the asymmetric coordinate can be delocalized such as to provide a direct pump-dump pathway involving a mostly single intermediate state. The present use of a rather simple model Hamiltonian facilitates application to specific molecular systems by virtue of its straightforward parameterization. In this respect the used OCT-MCTDH approach is ideally suited for studying driven quantum dynamics of such systems. In order to avoid the backward reaction of DPT through tunneling, an energetic difference between the two tautomers (global minima) should be present. In fact, the asymmetrically substituted porphycene (9-actetoxy-2,7,12,17-tetra-n-propylporphycene) (**4**) (see Fig. 1.1) fits this requirement. DPT reactions triggered

by the pump-dump scheme have been studied for this molecule in the electronic ground state. In this thesis, the possibility to use IR laser-controlled double proton transfer as a way of influencing the direction of the $S_0 \rightarrow S_1$ transition dipole moment has been investigated. This is possible because in porphycenes, it depends completely on the positions of the protons. This gives a means for changing the dipole-dipole interaction between neighboring chromophores in a molecular photonic wire. The estimated effect amounts to a 60% change of the transfer coupling, which could be used to design a molecular switch operating on a time scale of a few picoseconds and being, in principle, reversible. It has been demonstrated that, ultrafast laser control in the IR regime could be used as an alternative way for controlling the energy transfer through molecular photonic wires. This provides an alternative to established (slow) methods such as changing pH value of the medium or electrochemical oxidation.

Actually this proof-of-principle study calls for many extensions. First, the two dimensional model of DPT needs to be extended to involve the effect of heavy atom motions since it could affect the double proton transfer reactions and its mechanisms. Indeed Waluk and coworkers showed that the coupling to this type of motions may have a strong influence on the dynamics [79, 195, 196]. Second, a suitable design for a molecular photonic wire containing a DPT switching unit has to be found. This implies not only a favorable orientation of the transition dipoles of neighboring units but also the dominance of through space Förster transfer over through bond energy transfer.

In the second part of thesis, laser driven dynamics of collective carbonyl vibrations of $Mn_2(CO)_{10}$ have been studied. Computational chemistry for this system has been done using BP86/TZVB level of theory. Optimized parameters have been obtained for both D_{4d} and D_{4h} structures. Our quantum chemistry calculations using this level of theory agreed with the literature data. It has been found that, D_{4d} is the most stable isomer i.e. a global minimum and D_{4h} is 4.6 kcal/mol higher energetics than the D_{4d} isomer and it is a transition state of D_{4d} with very low imaginary frequency. Calculated parameters for the D_{4d} structure are in pretty good agreement with the crystal structure. IR spectra obtained within harmonic approximation have in good agreement with experimental one.

In order to see how much coupling between normal modes exists, the anharmonic PES should be created. A ten-dimensional PES for all carbonyl modes has been obtained. The two degenerate E_1 carbonyl and highest intensity B_2 stretching vibrations are treated beyond harmonic approximations and the rest are treated harmonically. Anharmonic frequencies for such a 10D model has been calculated.

It has been demonstrated that laser-driven wave packet circulation with respect to the two degenerate E_1 carbonyl stretching vibrations in a pre-oriented $Mn_2(CO)_{10}$ model is possible. The wave packet circulation corresponds to a vibrational excitation moving around the symmetry axis of the system. It has been shown that a classical picture holds approximately during the interaction with the excitation laser pulse. Later on, appreciable wave packet dispersion sets in such that the classical picture becomes meaningless, although the wave packet still circulates around the minimum of the potential energy surface.

The possibility of wave packet circulation upon excitation of degenerate vibrational modes with circularly polarized laser light could have been anticipated from the work of J. Manz et al. on triatomic molecules. [168, 197] Therefore, the important point here is the robustness of wave packet circulation with respect to intramolecular vibrational

energy redistribution in a polyatomic molecule. To proof this we have considered the coupling of the two E_1 mode to other intramolecular degrees of freedom, which have been described in harmonic approximation. This resulted in a seven-dimensional model for which the time-dependent Schrödinger equation has been solved using the MCTDH approach. It has been shown that the localization of the wavepacket during the circulation depends strongly on the laser amplitude. For weak laser field the localization of the wavepacket persists for a long propagation time. For the stronger laser field the radius of circulation is bigger but the wavepacket is dispersed faster. For moderate excitation conditions of one or two quanta in the E_1 modes, at most about 20 % of the absorbed energy is disposed into the bath modes within a time span of 5 picoseconds. In this respect it is important to note that the circularly polarized laser field generates a nuclear ring current which induces a magnetic field in propagation direction of the laser field [194]. This assigns a directionality making it possible, at least in principle, to differentiate between left and right circulation. Angular moment is also a property of interest to be measured.

One-dimensional PES scan for the moving CO center of mass away from the manganese atom using DFT is done for the axial and the equatorial CO group. It is found that the dissociation energy for the equatorial CO group is an energy lower of about 9 kcal/mole than the axial CO group. Since the Mn-CO center of mass can not be excited directly or might be it is not IR active, one could excite CO vibrations. Then in order to initiate CO bond breaking, the two-dimensional (R_{MCO} and r_{CO}) dissociative PES for the axial and the equatorial CO group should be introduced. For investigation of the quantum dynamics for CO bond breaking the 2D dissociative PES is created using DFT. Then, displaced ground state wavepacket along the r_{CO} coordinate is used instead of using direct laser excitation. It is found the dissociation yield is very small even though the gained energy corresponds to the displacement is higher than the dissociation barrier of carbonyl groups. On the basis of these 2D PES for axial and equatorial CO groups it has been concluded that laser-induced of non-statistical CO bond breaking by excitation of CO vibrations is very hard for this molecule. As an extension of this work, these 2D PES should be extended to involve the other bath modes using CRS model Hamiltonian. These bath modes could couple to these coordinates and could promote the CO bond breaking.

BIBLIOGRAPHY

[1] A. Battersby, C. Fookes, G. Matcham, and E. Mcdonald. Nature **285**(5759), 17 (1980).

[2] H. Fischer and H. Orth. Die Chemie des Pyrrols, vol. II, Part 1. Akademic Verag, Leipzig (1937).

[3] D. Dolphin. (ed) The porphyrins, Academic Press, New York (1978).

[4] R. Lammi, A. Ambroise, T. Balasubramanian, R. Wagner, D. Bocian, D. Holten, and J. Lindsey. J. Am. Chem. Soc. **122**(31), 7579 (Aug. 2000).

[5] D. Kuciauskas, P. Liddell, S. Lin, T. Johnson, S. Weghorn, J. Lindsey, A. Moore, T. Moore, and D. Gust. J. Am. Chem. Soc. **121**(37), 8604 (Sep. 1999).

[6] H. Levanon, T. Galili, A. Regev, G. Wiederrecht, W. Svec, and M. Wasielewski. J. Am. Chem. Soc. **120**(25), 6366 (Jul. 1998).

[7] A. Renn, U. Wild, and A. Rebane. J. Phys. Chem. A **106**(13), 3045 (Apr. 2002).

[8] C. Carcel, J. Laha, R. Loewe, P. Thamyongkit, K. Schweikart, V. Misra, D. Bocian, and J. Lindsey. J. Org. Chem. **69**(20), 6739 (Oct. 2004).

[9] T. Hasobe, P. Kamat, M. Absalom, Y. Kashiwagi, J. Sly, M. Crossley, K. Hosomizu, H. Imahori, and S. Fukuzumi. J. Phys. Chem. B **108**(34), 12865 (Aug. 2004).

[10] R. Bonnett. Chem. Soc. Rev. **24**(1), 19 (Feb. 1995).

[11] T. Maisch, R. Szeimies, G. Jori, and C. Abels. Photochem. Photobiol. Sciences **3**(10), 907 (2004).

[12] Y. Kobuke and K. Ogawa. Bull. Chem. Soc. Jpn. **76**(4), 689 (Apr. 2003).

[13] J. Collman, J. Mcdevitt, G. Yee, C. Leidner, L. Mccullough, W. Little, and J. Torrance. Pro. of the National Academy of Sciences of the United States of America **83**(13), 4581 (Jul. 1986).

[14] J. L. Sessler and S. J. Weghorn. *Expanded, Contracted and Isomeric Porphyrins*. Elsevier Science., Oxford. (1997).

[15] K. M. Kadish, K. M. Smith, and R. Guilard. *The Porphyrin Handbook Vol. 2* (Academic Press, New York., 2000).

[16] E. Vogel, M. Köcher, H. Schmickler, and J. Lex. Angew. Chem. Int. Ed. **25**, 257 (1986).

[17] L. Webb and Fleische.EB. J. Chem. Phys. **43**(9), 3100 (1965).

[18] U. Langer, C. Hoelger, B. Wehrle, L. Latanowicz, E. Vogel, and H.-H. Limbach. J. Phys. Org. Chem. **13**, 23 (2000).

[19] J. Radziszewski, J. Waluk, and J. Michl. Chem. Phys. **136**(2), 165 (Sep. 1989).

[20] J. Waluk. In *Hydrogen transfer reactions* (edited by J. Hynes, J. Klinman, H.-H. Limbach, and R. Schowen) (VCH-Wiley, Weinheim, 2007), vol. 1, chap. 8, p. 245.

[21] W. M. Latimer and W. H. Rodebush. J. Am. Chem. Soc. **42**, 1419 (1920).

[22] M. L. Huggins. Angew. Chem. Int. Ed. **10**, 147 (1971).

[23] L. Pauling. *The nature of the chemical bond* (Cornell University Press, Ithaka, 1939).

[24] L. Pauling. J. Am. Chem. Soc. **53**, 1367 (1931).

[25] V. G. R. Desiraju and homas Steiner. *The weak hydrogen bond: in structural chemistry and biology* (Oxford University Press, New York., 1999).

[26] M. L. Huggins. J. Phys. Chem. **40**, 723 (1936).

[27] P. Schuster, G. Zundel, and C. Sandorfi (eds.). *The hydrogen bond theory* (North-Holland, Amsterdam, 1976).

[28] H.-H. Limbach and J. Manz. Ber. Bunsenges. Phys. Chem. **102**, 289 (1998).

[29] A. Kohen and H.-H. Limbach (eds.). *Isotope Effects in Chemistry and Biology* (Taylor and Francis, Boca Raton, 2005).

[30] J. T. Hynes, J. P. Klinman, H. H. Limbach, and R. Schowen (eds.). *Hydrogen transfer Reactions* (Wiley-VCH, Weinheim, 2007).

[31] G. A. Jeffrey and W. Saenger. *Hydrogen Bonding in Biological Structures* (Springer-Verlag, Berlin, 1991).

[32] I. Thanopulos and M. Shapiro. J. Am. Chem. Soc. **127**(41), 14434 (2005).

[33] S. Hammes-Schiffer. J. Chem. Phys. **105**(6), 2236 (1996).

[34] M. Shibl. *Mechanisms of Double Proton Transfer Tautoerization and Quantum Control of Tautomerism in Enantiomers by Light* (PhD thesis Freie Universtät Berlin, 2006).

[35] R. Rousseau, V. Kleinschmidt, U. W. Schmitt, and D. Marx. Phys. Chem. Chem. Phys. **6**, 1848 (2004).

[36] Z. Smedarchina, W. Siebrand, and A. Fernandez-Ramos. J. Chem. Phys. **127**, 174513 (2007).

[37] M. K. Abdel-Latif and O. Kuehn. Chem. Phys. **368**(1-2), 76 (Feb. 2010).

[38] L. Meschede and H. H. Limbach. J. Phys. Chem. **95**, 19267 (1991).

[39] Z. Smedarchina, W. Siebrand, A. Fernández-Ramos, and R. Meana-Pañeda. Z. Phys. Chem. **222**, 1291 (2008).

[40] G. L. Barnes and W. L. Hase. Nat. Chem. **1**(2), 103 (May 2009).

[41] M. Rini, B.-Z. Magnes, E. Pines, and E. T. J. Nibbering. Science **301**, 349 (2003).

[42] V. Zoete and M. Meuwly. J. Chem. Phys. **121**(9), 4377 (2004).

[43] Z. Smedarchina, M. Zgierski, W. Siebrand, and P. M. K. J. Rodriguez-Otero. J. Chem. Phys. **109**, 1014 (1998).

[44] S. van Gisbergen, A. Rosa, G. Ricciardi, and E. Baerends. J. Chem. Phys. **111**(6), 2499 (Aug. 1999).

[45] Z. Smedarchina, M. F. Shibl, O. Kühn, and A. Fernández-Ramos. Chem. Phys. Lett. **436**, 314 (2007).

[46] M. Dewar, S. Olivella, and J. Stewart. J. Am. Chem. Soc. **108**(19), 5771 (Sep. 1986).

[47] L. Xu, C. E. Doubleday, and K. N. Houk. Angew. Chem. Int. Ed. **48**(15), 2746 (2009).

[48] S. Schweiger, B. Hartke, and G. Rauhut. Phys. Chem. Chem. Phys. **6**, 3341 (2004).

[49] S. Schweiger, B. Hartke, and G. Rauhut. Phys. Chem. Chem. Phys. **7**(3), 493 (2005).

[50] M. Shapiro and P. Brumer. *Principles of the Quantum Control of Molecular Processes* (Wiley, Hoboken, 2003).

[51] O. Kühn and L. Wöste (eds.). *Analysis and control of ultrafast photoinduced reactions*, vol. 87 of *Springer Series in Chemical Physics* (Springer, Heidelberg, 2007).

[52] M. Dantus and V. Lozovoy. Chem. Rev.s **104**(4), 1813 (Apr. 2004).

[53] V. V. Lozovoy and M. Dantus. ChemPhysChem **6**, 1970 (2005).

[54] A. Stolow, A. Bragg, and D. Neumark. Chem. Rev.s **104**(4), 1719 (Apr. 2004).

[55] R. de Vivie-Riedle and U. Troppmann. Chem. Rev. **107**, 5082 (NOV 2007).

[56] D. Tannor and S. Rice. J. Chem. Phys. **83**(10), 5013 (1985).

[57] S. Shi, A. Woody, and H. Rabitz. J. Chem. Phys. **88**(11), 6870 (Jun. 1988).

[58] W. Zhu and H. Rabitz. J. Chem. Phys. **109**, 385 (1998).

[59] R. Kosloff, S. A. Rice, P. Gaspard, S. Tersigni, and D. J. Tannor. Chem. Phys **139**, 201 (1989).

[60] J. Werschnik and E. K. U. Gross. J. Phys. B-Atomic Mol. Opt. Phys. **40**, R175 (2007).

[61] N. Došlić, O. Kühn, J. Manz, and K. Sundermann. J. Phys. Chem. A **102**, 9645 (1998).

[62] N. Došlić, K. Sundermann, L. González, O. Mo, J. Giraud-Girard, and O. Kühn. Phys. Chem. Chem. Phys. **1**, 1249 (1999).

[63] H. Naundorf, K. Sundermann, and O. Kühn. Chem. Phys. **240**, 163 (1999).

[64] E. Geva. J. Chem. Phys. **116**, 1629 (2002).

[65] V. Malinovsky and D. Tannor. Phys. Rev. a **56**(6), 4929 (Dec. 1997).

[66] I. Sola, V. Malinovsky, and D. Tannor. Phys. Rev. a **60**(4), 3081 (Oct. 1999).

[67] G. K. Paramonov. In *Femtosecond Chemistry* (edited by J. Manz and L. Wöste) (Verlag Chemie, Weinheim, 1995), vol. 2, p. 671.

[68] M. Korolkov and G. Paramonov. Phys. Rev. a **57**(6), 4998 (Jun. 1998).

[69] U. Gaubatz, P. Rudecki, S. Schiemann, and K. Bergmann. J. Chem. Phys. **92**(9), 5363 (May 1990).

[70] G. Paramonov and V. Savva. Phys. Lett. a **97**(8), 340 (1983).

[71] M. V. Korolkov, J. Manz, and G. K. Paramonov. Chem. Phys. **217**, 341 (1997).

[72] J. Lawall and M. Prentiss. Phys. Rev. Lett. **72**(7), 993 (Feb. 1994).

[73] J. E. Combariza, B. Just, J. Manz, and G. K. Paramonov. J. Phys. Chem. **95**, 10351 (1991).

[74] M. V. Korolkov, J. Manz, and G. K. Paramonov. J. Chem. Phys. **105**, 10874 (1996).

[75] K. Nishikawa, T. Ito, K. Sugimori, Y. Ohta, and H. Nagao. Int. J. Quant. Chem. **102**, 665 (2005).

[76] I. Thanopulos and M. Shapiro. J. Am. Chem. Soc. **127**, 14434 (2005).

[77] I. Thanopulos, E. Paspalakis, and V. Yannopapas. Nanotechnology **19**, 445202 (2008).

[78] M. K. Abdel-Latif and O. Kuehn. Theo. Chem. Acc. **128**(3), 307 (Feb. 2011).

[79] J. Waluk. Acc. of Chem. Res. **39**(12), 945 (Dec. 2006).

[80] D. Mauzerall. Photosyn. Res. **10**(3), 163 (1986).

[81] S. Karrasch, P. Bullough, and R. Ghosh. Embo J. **14**(4), 631 (Feb. 1995).

[82] R. Wagner and J. Lindsey. J. Am. Chem. Soc. **116**(21), 9759 (Oct. 1994).

[83] R. W. Wagner, T. E. Johnson, and J. S. Lindsey. J. Am. Chem. Soc. **118**, 11166 (1996).

[84] F. Li, S. Gentemann, W. Kalsbeck, J. Seth, J. Lindsey, D. Holten, and D. Bocian. J. of Mat. Chem. **7**(7), 1245 (Jul. 1997).

[85] A. Ambroise, J. Li, L. Yu, and J. Lindsey. Org. Lett. **2**(17), 2563 (Aug. 2000).

[86] D. Holten, D. Bocian, and J. Lindsey. Acc. of Chem. Res. **35**(1), 57 (Jan. 2002).

[87] E. Hindin, R. Forties, R. Loewe, A. Ambroise, C. Kirmaier, D. Bocian, J. Lindsey, D. Holten, and R. Knox. J. Phys. Chem. B **108**(34), 12821 (Aug. 2004).

[88] H.-e. Song, M. Taniguchi, M. Speckbacher, L. Yu, D. F. Bocian, J. S. Lindsey, and D. Holten. J. Phys. Chem. B **113**(23), 8011 (Jun. 2009).

[89] R. Wagner and J. Lindsey. Pure and Applied Chem. **68**(7), 1373 (Jul. 1996).

[90] M. Heilemann, P. Tinnefeld, G. Mosteiro, M. Garcia-Parajo, N. Van Hulst, and M. Sauer. J. Am. Chem. Soc. **126**(21), 6514 (Jun. 2004).

[91] M. Heilemann, R. Kasper, P. Tinnefeld, and M. Sauer. J. Am. Chem. Soc. **128**(51), 16864 (Dec. 2006).

[92] S. Vyawahare, S. Eyal, K. Mathews, and S. Quake. Nano Lett. **4**(6), 1035 (Jun. 2004).

[93] J. K. M. Sanders, N. Bampos, Z. Clyde-Watson, S. L. Darling, J. C. Hawley, H. J. Kim, C. C. Mak, and S. J. Webb. *Axial Coordination Chemistry of Metalloporphyrins, in The Porphyrin Handbook, ed. K. M. Kadish and K. M. Smith and R. Guilard* (Academic Press, San Diego, 2000).

[94] J. K. M. Sanders. *Coordination Chemistry of Oligoporphyrins, in The Porphyrin Handbook, ed. K. M. Kadish and K. M. Smith and R. Guilard* (Academic Press, San Diego, 2000).

[95] I. Danks, I. Sutherland, and C. Yap. J. of the Chem. Soc.-Per. Trans. **1**(2), 421 (Feb. 1990).

[96] F. Felluga, P. Tecilla, L. Hillier, C. Hunter, G. Licini, and P. Scrimin. Chem. Comm. **12**, 1087 (2000).

[97] U. Michelsen and C. Hunter. Angew. Chem. Int. Ed. **39**(4), 764 (2000).

[98] R. Haycock, A. Yartsev, U. Michelsen, V. Sundstrom, and C. Hunter. Angew. Chem. Int. Ed. **39**(20), 3616 (2000).

[99] Y. Kuroda, K. Sugou, and K. Sasaki. J. Am. Chem. Soc. **122**(32), 7833 (Aug. 2000).

[100] C. Hunter, J. Sanders, G. Beddard, and S. Evans. J. of the Chem. Soc.-Chem. Comm. **22**, 1765 (Nov. 1989).

[101] D. Guldi, C. Luo, A. Swartz, M. Scheloske, and A. Hirsch. Chem. Comm. **12**, 1066 (Jun. 2001).

[102] J. Bahr, G. Kodis, L. de la Garza, S. Lin, A. Moore, T. Moore, and D. Gust. J. Am. Chem. Soc. **123**(29), 7124 (Jul. 2001).

[103] R. Wagner, J. Lindsey, J. Seth, V. Palaniappan, and D. Bocian. In *Abstracts of Papers of the American Chemical Society* (AMER CHEMICAL SOC, 1155 16TH ST, NW, WASHINGTON, DC 20036, 1996), vol. 212, pp. 411–ORGN.

[104] R. Lammi, R. Wagner, A. Ambroise, J. Diers, D. Bocian, D. Holten, and J. Lindsey. J. Phys. Chem. B **105**(22), 5341 (Jun. 2001).

[105] M. Albelda, P. Diaz, E. Garcia-Espana, J. Lima, C. Lodeiro, J. de Melo, A. Parola, F. Pina, and C. Soriano. Chem. Phys. Lett. **353**(1-2), 63 (Feb. 2002).

[106] P. Wang and S. Wu. J. of PhotoChem. and Photobiology A-Chem. **118**(1), 7 (Oct. 1998).

[107] J. Otsuki, T. Akasaka, and K. Araki. Coor. Chem. Rev. **252**(1-2), 32 (Jan. 2008).

[108] V. May and O. Kühn. *Charge and energy transfer dynamics in molecular systems, 3nd revised and enlarged edition* (Wiley–VCH, Weinheim, 2011).

[109] W. Herrmann and B. Cornils. Angew. Chem. Int. Ed. **36**(10), 1049 (Jun. 1997).

[110] C. Daniel, M. Heitz, L. Lehr, J. Manz, and T. Schroder. J. of Phys. Chem. **97**(48), 12485 (Dec. 1993).

[111] O. Rubner, V. Engel, M. Hachey, and C. Daniel. Chem. Phys. Lett. **302**(5-6), 489 (Mar. 1999).

[112] M. Paterson, P. Hunt, M. Robb, and O. Takahashi. J. Phys. Chem. A **106**(44), 10494 (Nov. 2002).

[113] Y. Zhao and O. Kühn. Chem. Phys. Lett. **302**, 7 (1999).

[114] O. Kühn, J. Manz, and Y. Zhao. Phys. Chem. Chem. Phys. **1**, 3103 (1999).

[115] Y. Zhao and O. Kühn. J. Phys. Chem. A **104**, 4882 (2000).

[116] E. Brimm, M. Lynch, and W. Sesny. J. Am. Chem. Soc. **76**(14), 3831 (1954).

[117] L. Dahl, E. Ishishi, and R. Rundle. J. Chem. Phys. **26**(6), 1750 (1957).

[118] T. Seder, S. Church, and E. Weitz. J. Am. Chem. Soc. **108**(24), 7518 (Nov. 1986).

[119] T. Seder, S. Church, and E. Weitz. J. Am. Chem. Soc. **108**(5), 1084 (Mar. 1986).

[120] L. Rothberg, N. Cooper, K. Peters, and V. Vaida. J. Am. Chem. Soc. **104**(12), 3536 (1982).

[121] S. Church, H. Hermann, F. Grevels, and K. Schaffner. J. Chem. Soc.-Chem. Comm. **12**, 785 (1984).

[122] K. Schaffner and F. Grevels. J. Mol. Str. **173**, 51 (May 1988).

[123] T. Meyer and J. Caspar. Chem. Rev.s **85**(3), 187 (1985).

[124] H. Haas and R. Sheline. J. Chem. Phys. **47**(8), 2996 (1967).

[125] D. Parker. Spectrochimica Acta Part A-Mol. and BioMol. Spec. **39**(5), 463 (1983).

[126] Y. Xie, J. Jang, R. King, and H. Schaefer. Inorg. Chem. **42**(17), 5219 (Aug. 2003).

[127] T. Ticich, M. Likar, H. Dubal, L. Butler, and F. Crim. J. Chem. Phys. **87**(10), 5820 (Nov. 1987).

[128] T. ArusiParpar, R. Schmid, R. Li, I. Bar, and S. Rosenwaks. Chem. Phys. Lett. **268**(1-2), 163 (Apr. 1997).

[129] T. Witte, T. Hornung, L. Windhorn, D. Proch, R. de Vivie-Riedle, M. Motzkus, and K. L. Kompa. J. Chem. Phys. **118**, 2021 (2003).

[130] C. Ventalon, J. M. Fraser, M. H. Vos, A. Alexandrou, J.-L. Martin, and M. Joffre. Proc. Natl. Acad. Sci. USA **101**, 13216 (2004).

[131] T. Klamroth. J. Chem. Phys. **124**(14), 144310 (Apr. 2006).

[132] K. Pronin and A. Bandrauk. Phys. Rev. B **69**(19) (May 2004).

[133] F. Remacle and R. Levine. Pro. of the National Academy of Sciences of the United States of America **103**(18), 6793 (May 2006).

[134] A. S. Moskalenko, A. Matos-Abiague, and J. Berakdar. Phys. Rev. B **74**(16) (Oct. 2006).

[135] D. J. Maas, D. I. Duncan, R. B. Vrijen, W. J. van der Zande, and L. D. Noordam. Chem. Phys. Lett. **290**, 75 (1998).

[136] O. Kühn. Chem. Phys Lett. **402**(1-3), 48 (2005).

[137] M. Born and R. Oppenhheimer. Ann. Phys. **84**, 457 (1927).

[138] D. Hartree. Pro. Cam. Philos. Soc. **24**, 89 (Jul. 1928).

[139] D. Hartree. Pro. Cam. Philos. Soc. **24**, 111 (Jul. 1928).

[140] A. Schafer, H. Horn, and R. Ahlrichs. J. Chem. Phys. **97**(4), 2571 (Aug. 1992).

[141] A. Schafer, C. Huber, and R. Ahlrichs. J. Chem. Phys. **100**(8), 5829 (Apr. 1994).

[142] P. Lowdin. J. Chem. Phys. **18**(3), 365 (1950).

[143] E. Baerends and O. Gritsenko. J. Phys. Chem. A **101**(30), 5383 (Jul. 1997).

[144] P. Hohenberg and W. Kohn. Phys. Rev. **136**(3B), B864 (Nov 1964).

[145] A. Becke. J. Chem. Phys. **98**(7), 5648 (Apr. 1993).

[146] C. Lee, W. Yang, and R. Parr. Phys. Rev. B **37**(2), 785 (Jan. 1988).

[147] A. Becke. Phys. Rev. a **38**(6), 3098 (Sep. 1988).

[148] J. Perdew. Phys. Rev. B **33**(12), 8822 (Jun. 1986).

[149] W. Koch and M. C. Holthausen. *A Chemist's Guide to Density Functional Theory* (Wiley, Weinheim, 2000).

[150] B. A. Ruf and W. H. Miller. J. Chem. Soc. Faraday Trans. 2 **84**, 1523 (1988).

[151] R. Kosloff. J. of Phys. Chem. **92**(8), 2087 (Apr. 1988).

[152] M. D. Feit, J. A. Fleck, and A. Steiger. J. Comp. Phys. **47**, 412 (1982).

[153] M. Feit and J. Fleck. J. Chem. Phys. **78**(1), 301 (1983).

[154] H. Tal-Ezer and R. Kosloff. J. Chem. Phys. **81**(9), 3967 (1984).

[155] T. Park and J. Light. J. Chem. Phys. **85**(10), 5870 (Nov. 1986).

[156] M. H. Beck, A. Jäckle, G. A. Worth, and H.-D. Meyer. Phys. Rep. **324**, 1 (2000).

[157] P. A. M. Dirac. Proc. Cam. Philos. Soc. **26**, 376 (1930).

[158] J. Frenkel. *Wave Mechanics* (Clarendon Press, Oxford, 1934).

[159] M. Beck and H. Meyer. Zeitschrift Fur Physik D-Atoms Molecules and Clusters **42**(2), 113 (Nov. 1997).

[160] G. Worth, M. Beck, A. Jäckle, and H.-D. Meyer. The mctdh package, version 8.4. University of Heidelberg, Heidelberg (2007).

[161] H.-D. Meyer, U. Manthe, and L. S. Cederbaum. Chem. Phys. Lett. **165**, 73 (1990).

[162] R. Kosloff and H. Tal-Ezer. Chem. Phys. Lett. **127**(3), 223 (Jun. 1986).

[163] H. Meyer and G. A. Worth. Theor. Chem. Acc. **109**, 251 (2003).

[164] H.-D. Meyer, F. L. Quere, C. Leonard, and F. Gatti. Chem. Phys. **329**, 179 (2006).

[165] F. A. Carey and R. J. Sundberg. *Advanced Organic Chemistry* (VCH, Weinheim, 1993).

[166] G. Gilbert, A. Aspect, and C. Fabre. *Introduction to Quantum Optics From the Semi-classical Approach to Quantized Light* (Cambrigde University Press, New York, 2010).

[167] I. Barth, J. Manz, Y. Shigeta, and K. Yagi. J. Am. Chem. Soc. **128**(21), 7043 (May 2006).

[168] I. Barth, J. Manz, and P. Sebald. Chem. Phys. **346**(1-3), 89 (May 2008).

[169] A. Peirce, M. Dahleh, and H. Rabitz. Phys. Rev. A **37**, 4950 (1988).

[170] W. Zhu, J. Botina, and H. Rabitz. J. Chem. Phys. **108**, 1953 (1998).

[171] R. S. Judson and H. Rabitz. Phys. Rev. Lett. **68**, 1500 (1992).

[172] H. Rabitz. Theor. Chem. Acc. **109**, 64 (2003).

[173] K. Sundermann and R. de Vivie-Riedle. J. Chem. Phys. **110**, 1896 (2000).

[174] L. Wang, H.-D. Meyer, and V. May. J. Chem. Phys. **125**(1), 014102 (2006).

[175] S. Linden, H. Giessen, and J. Kuhl. Physica Status Solidi B-Basic Res. **206**(1), 119 (Mar. 1998).

[176] M. Schröder, J.-L. Carreon-Macedo, and A. Brown. Phys. Chem. Chem. Phys. **10**, 850 (2008).

[177] P. M. Kozlowski, M. Z. Zgierski, and J. Baker. J. Chem. Phys. **109**, 5905 (1998).

[178] G. Worth, M. Beck, A. Jäckle, and H.-D. Meyer. The mctdh package, version 8.3. University of Heidelberg, Heidelberg (2002).

[179] M. Gil, J. Jasny, E. Vogel, and J. Waluk. Chem. Phys. Lett. **323**(5-6), 534 (Jun. 2000).

[180] M. J. Frisch, G. W. Trucks, H. B. Schlegel, G. E. Scuseria, M. A. Robb, J. R. Cheeseman, J. A. Montgomery, Jr., T. Vreven, K. N. Kudin, J. C. Burant, J. M. Millam, S. S. Iyengar, J. Tomasi, V. Barone, B. Mennucci, M. Cossi, G. Scalmani, N. Rega, G. A. Petersson, H. Nakatsuji, M. Hada, M. Ehara, K. Toyota, R. Fukuda, J. Hasegawa, M. Ishida, T. Nakajima, Y. Honda, O. Kitao, H. Nakai, M. Klene, X. Li, J. E. Knox, H. P. Hratchian, J. B. Cross, V. Bakken, C. Adamo, J. Jaramillo, R. Gomperts, R. E. Stratmann, O. Yazyev, A. J. Austin, R. Cammi, C. Pomelli, J. W. Ochterski, P. Y. Ayala, K. Morokuma, G. A. Voth, P. Salvador, J. J. Dannenberg, V. G. Zakrzewski, S. Dapprich, A. D. Daniels, M. C. Strain,

O. Farkas, D. K. Malick, A. D. Rabuck, K. Raghavachari, J. B. Foresman, J. V. Ortiz, Q. Cui, A. G. Baboul, S. Clifford, J. Cioslowski, B. B. Stefanov, G. Liu, A. Liashenko, P. Piskorz, I. Komaromi, R. L. Martin, D. J. Fox, T. Keith, M. A. Al-Laham, C. Y. Peng, A. Nanayakkara, M. Challacombe, P. M. W. Gill, B. Johnson, W. Chen, M. W. Wong, C. Gonzalez, and J. A. Pople. Gaussian 03, Revision B.04. Gaussian, Inc., Wallingford, CT, 2004.

[181] M. W. Schmidt, K. K. Baldridge, J. A. Boatz, S. T. Elbert, M. S. Gordon, J. H. Jensen, S. Koseki, N. Matsunaga, K. A. Nguyen, T. L. W. S. Su, M. Dupuis, , and J. A. M. Jr. General atomic and molecular electronic structure system (1993).

[182] M. F. Shibl, M. Pietrzak, H.-H. Limbach, and O. Kühn. ChemPhysChem **8**, 315 (2007).

[183] J. Waluk, M. Muller, P. Swiderek, M. Kocher, E. Vogel, G. Hohlneicher, and J. Michl. J. Am. Chem. Soc. **113**(15), 5511 (Jul. 1991).

[184] M. Parac and S. Grimme. J. Phys. Chem. A **106**(29), 6844 (Jul. 2002).

[185] A. L. Sobolewski, M. Gil, J. Dobkowski, and J. Waluk. J. Phys. Chem. A **113**(27), 7714 (Jul. 2009).

[186] N. Došlić, O. Kühn, and J. Manz. Ber. Bunsenges. Phys. Chem. **102**, 292 (1998).

[187] Q. Li and Y. Liu. Inorg. Chem. **40**(23), 5842 (Nov. 2001).

[188] Y. Xie, H. Schaefer, and R. King. J. Am. Chem. Soc. **122**(36), 8746 (Sep. 2000).

[189] Almennin.A, G. Jacobsen, and H. Seip. Acta Chemica Scand. **23**(2), 685 (1969).

[190] M. Martin, B. Rees, and A. Mitschler. Acta Crys. Sec. B-Str. Science **38**(JAN), 6 (1982).

[191] L. Dahl and R. Rundle. Acta Crys. **16**(5), 419 (1963).

[192] C. R. Baiz, P. L. Mcrobbie, J. M. Anna, E. Geva, and K. J. Kubarych. Acc. of Chem. Res. **42**(9), 1395 (Sep. 2009).

[193] H. Stapelfeldt and T. Seideman. Rev. Mod. Phys. **75**, 543 (2003).

[194] I. Barth and J. Manz. In *Progress in Ultrafast Intense Laser Science VI* (edited by K. Yamanouchi, G. Gerber, and A. Bandrauk) (Springer, Berlin, 2010), Springer Series in Chemical Physics.

[195] A. Vdovin, J. Waluk, B. Dick, and A. Slenczka. Chemphyschem **10**(5), 761 (Mar. 2009).

[196] L. Walewski, J. Waluk, and B. Lesyng. J. Phys. Chem. A **114**(6), 2313 (Feb. 2010).

[197] I. Barth, J. Manz, G. Perez-Hernandez, and P. Sebald. Zeitschrift Fur Physikalische Chemie-Int. J. of Res. In Phys. Chem. & Chem. Phys. **222**(8-9), 1311 (2008).

Acknowledgements

It is so difficult for me to remember all persons I have to thank them — but I try to remember as can as I do.

I would first of all like to thank my GOD (*Al-Hamd Lellah* is the arabic version of thanks God) for every thing he gave me, for choosing to me every thing e.g. Germany to come to and my supervisors, etc. . . .

The second people I have to thank are my parents, mom and dad. In fact, whatever I thank or do anything for them, I can not return back to them their favors to me. I can not forget that, they were the main reason for me to come to the life. It was impossible to me to continue without their support for me, praying (asking God) to me all the time to be a successful person and motivating me to work well to be a productive person over my life. I am indebted to them forever.

It was small part of my prophet Mohammed talk which says, ''Who does not thank people, does not thank God'' so considering this talk, I have to . . .

Over the years in my daily life it was and still is my hope to help others whoever they are and to make them happy. Also, it has been my good fortune to meet and encounter many people who have given me more of their time, companionship, professional and personal help, and in the first place above all: patience than leaving me alone at least without guiding me to the right direction.

One of these people is my supervisor, Prof. Dr. Oliver Kühn, I would like to thank him so much. He not only gave me the scientific support and supervision that a graduate student can expect from his supervisor, but he also helped me beyond the scientific research e.g. in personal level. Thanks to him again, he allowed and encouraged me to be one of his group in FU-Berlin and then in Uni-Rostock, for suggesting me the point of research, for his open door to me all the time for any of my questions and helping me to overcome the obstacles I encountered in Germany. I hope in the future I can return back to any of his family some of his favors.

Thanks go to Prof. Dr. Ralf Ludwig for his supervision, helping and allowing me to be accepted in the Institute of Chemistry to make my defense there.

The gratitude should go to Dr. Yun-an Yan. He is one of my room mates and he was the person who is responsible for the computer stuff. He helped me a lot with his scripts, without them I would spend more time to extract data from the output files.

There is a Professor to whom I would specifically like to introduce my thanks for his support he introduced to me over the time I was in Berlin. He is Prof. Dr. Jörn Manz. I am grateful to him for the kind hospitality with me and my wife.

A special word of thank and gratitude, to my previous supervisors. Prof. Dr. A. Abdel-Khaleq, he helped me a lot to finish the official stuff in my home university in Beni-Suef in Egypt for example, getting any extension to complete my work here. Prof. Dr. Rafie Abu-Eittah for his advice and letting me complete my work here in Germany.

I have to acknowledge with the gratitude to Dr. Mohamed Shibl since he was the ring link between me and my supervisor, Prof. Dr. Oliver Kühn. I think without his help it would be very difficult to me to be accepted by my supervisor. Also to Prof. Dr. Refaat. Helal for asking Mohamed to talk to my supervisor to accept me as a member in his group.

A list that, alas, has far too many names on it to mention separately is that of all the group members and room mates in Rostock that I have worked and talked over the years, Yun-an Yan, Ashour Ahmed, David Ambrosek, Mahdi Taghikhani, Sergey Polyutov, Sergey Bokarev, Olga Bokareva, Guennaddi Paramonov and Mateusz Lisaj for

their kindness. My gratitude goes out to all these colleagues and former room mates at the Chemistry Institute in FU-Berlin, Gireesh Krishnan and Yonggang Yang.

Moving towards more personal acknowledgements, I would like to express a big block of aggregates of thanks towards all my family, Mrs. Marwa Hamza (my wife) for her support and patience, Abdel-Rahman, Basmala and Goweyreyah (my children), Mr. Salah Abdel-Latif (my brother) for every thing, Sohair, Asmaa, Amal, Shymaa, Gehad and Mysoon (my sisters) for praying to me all the time and then comes my friends.

For financial support, I would like to thank the Egyptian higher eduction ministry for its two year scholarship (March-10-2007 to March-09-2009). In the same time I would like to thank my supervisor, Prof. Dr. Oliver Kühn for supporting me financially for the rest period (April-10-2009 to now) to complete my thesis.

Last but not least, I would like to introduce my deep thanks to any person I have ever met in Germany and he/she has smiled in my face without having any deal between us.

Rostock,   *M. K. Abdel-Latif*

October, 11, 2011

Published Papers

(4) ***Carbonyl Vibrational Wave Packet Circulation in $Mn_2(CO)_{10}$ Driven by Ultrashort Polarized Laser Pulses.***

M. K. Abdel-Latif and O. Kuehn.

*J. Chem. Phys. **135**, (2011) 084314.*

(3) ***Laser Control of Single and Double Proton Transfer Reactions*** .

N. Doslic, **M. K. Abdel-Latif** and O. Kuehn.

*Acta. Chim. Slov. **58** (2011), 411; D. Hadzi Festschrift.*

(2) ***Laser Control of Double Proton Transfer in Porphycenes: Towards an Ultrafast Switch for Photonic Molecular Wires.***
M. K. Abdel-Latif and O. Kuehn.

*Theo. Chem. Acc. **128**, (2011), 307.*

(1) ***Infrared Laser Driven Double Proton Transfer. An Optimal Control Theory Study***.

M. K. Abdel-Latif and O. Kuehn.

*Chem. Phys. **368**, (2010), 76.*

Talks

(1) *Laser Driven Dynamics and Control of Double Proton Transfer.*

Mahmoud K. Abdel-Latif

Institute of physics, Rostock university, June - 23 - 2009.

(2) *Multidimensional vibrational Hamiltonian and wave packet dynamics of $Mn_2(CO)_{10}$.*

Mahmoud K. Abdel-Latif

Institute of physics, Rostock university, December - 21 - 2010.

Graduate school, Institute of physics, Rostock university, January - 06 - 2011.

(3) *Laser Driven Dynamics of Double Proton Transfer and Wavepacket Circulation of $Mn_2(CO)_{10}$.*

Mahmoud K. Abdel-Latif

Department of Physical Chemistry, Rudjer Boskovic Institute, Zagreb, April - 07 - 2011.

Posters

(1) *Infrared Laser Driven Double Proton Transfer. An Optimal Control Theory Study.*

Mahmoud K. Abdel-Latif and Oliver Kühn

Symposium on Theoretical Chemistry, Sept. 8-12, 2009, Neuss, (Germany).

Organized by Prof. Dr. Christel M. Marian.

(2) *Multidimensional vibrational Hamiltonian and wave packet dynamics of $Mn_2(CO)_{10}$.*

Mahmoud K. Abdel-Latif and Oliver Kühn

Conference for Young Academics and PhD Students in Natural Science, June 15-17, 2011, Rostock, (Germany).

Organized by Prof. Dr. Heimo Reinitzer and Prof. Dr. Udo Kragl.

(3) *Carbonyl Vibrational Wave Packet Circulation in $Mn_2(CO)_{10}$ Driven by Ultrashort Polarized Laser Pulses.*

Mahmoud K. Abdel-Latif and Oliver Kühn

Symposium on Theoretical Chemistry, August. 21-25, 2011, Campus Sursee, Sursee - (Switzerland).

Organized by Prof. Dr. Markus Reiher.

(4) *Infrared Laser Driven Quantum Dynamics of Collective Carbonyl Vibrations of Dimanganese Decacarbonyl.*

Mahmoud K. Abdel-Latif and Oliver Kühn

International Conference on Correlation Effects in Radiation Fields 2011, Sept. 12-16, 2011, Rostock, (Germany).

Organized by Prof. Dr. Karl-Heinz Meiwes-Broer.

Curriculum Vitae

Name:	Mahmoud K. Abdel-Latif
Date of birth:	Nov. 15, 1975
Nationality:	Egyptian
Home address:	Towa, Beba, Beni-Suef, Egypt
Current address:	WokrenterStr. 37, 18055, Rostock, Germany
Marital status:	Married + three children
Email:	mahmoud.abdel-latif@uni-rostock.de

Education

1994	High school, Beni-Suef, Egypt
1998	B.Sc, Chemistry, Grade 82.8 % Faculty of Science, Beni-Suef branch, Cairo University, Egypt
2003	M.Sc., Physical Chemistry, Thesis entitled "An Experimental and Theoretical Studies on The Electronic Spectra And Structures of Some Pyridine Azides." Faculty of Science, Beni-Suef branch, Cairo University, Egypt
2008	Ph.D. Candidate, Institute of Physics, Rostock University, Supervisor : Prof. Dr. Oliver Kühn

Employment

1999-2003	Instructor, Faculty of Science, Beni-Suef branch, Cairo University, Egypt
Current	Lecturer assistance, Faculty of Science, Beni-Suef University, Beni-Suef, Egypt
04/09 - 09/11	Lecturer assistance, Institute of Physics, Rostock University,

Erklärung

Ich versichere hiermit, die vorliegende Arbeit selbstständig angefertigt und ohne fremde Hilfe verfasst zu haben. Keine außer den von mir angegebenen Hilfsmitteln und Quellen wurden bei der Erstellung dieser Dissertation verwendet und die den benutzten Werken inhaltlich und wörtlich entnommenen Stellen wurden als solche kenntlich gemacht.

Rostock   *Mahmoud Abdel-Latif*

October, 11, 2011   . . . .